NACA RM L57H05

NACA

RESEARCH MEMORANDUM

TWO-DIMENSIONAL CASCADE TESTS OF NACA 65-$(C_{l_o}A_{10})_{10}$ BLADE SECTIONS AT TYPICAL COMPRESSOR HUB CONDITIONS FOR SPEEDS UP TO CHOKING

By James C. Emery and James C. Dunavant

Langley Aeronautical Laboratory
Langley Field, Va.

NATIONAL ADVISORY COMMITTEE FOR AERONAUTICS

WASHINGTON

October 23, 1957
Declassified December 1, 1959

NATIONAL ADVISORY COMMITTEE FOR AERONAUTICS

RESEARCH MEMORANDUM

TWO-DIMENSIONAL CASCADE TESTS OF NACA 65-$(C_{l_o}A_{10})_{10}$ BLADE SECTIONS AT TYPICAL COMPRESSOR HUB CONDITIONS FOR SPEEDS UP TO CHOKING

By James C. Emery and James C. Dunavant

SUMMARY

Two-dimensional porous-wall cascade tests of NACA 65-$(C_{l_o}A_{10})_{10}$ blade sections at typical compressor hub conditions were run at speeds up to choking. A blade section of circular arcs designed to have a specific blade-passage area distribution was also tested. Results of these tests indicate that, for typical compressor blade hub sections, the angle of attack for best operation at high Mach numbers is about 6° higher than the design angle of attack selected to have pressure distributions at low speeds that are free of peaks. The decrease in the angle-of-attack range for low losses at high Mach numbers is due largely to choking of the blade passages, which are smaller at low angles of attack. The circular-arc blade section performed best at angles of attack for which the throat area was located rearward in the passage rather than at the leading edge.

INTRODUCTION

The present-day high-weight-flow compressors with low ratios of hub radius to tip radius have rotor blade sections at the root characterized by high solidity, low inlet flow angles, high cambers, and high turning angles. The combination of high camber, high solidity, and large maximum blade thickness used to meet the aerodynamic and strength requirements of root sections results in small blade-passage throat area. Although the axial or through velocity is often higher at the blade root than at the tip, the relative Mach number at which root sections are required to operate is low compared with tip Mach numbers. Choking, with the resulting high losses, may occur at a low relative entering Mach number and is frequently a real problem to the designer.

Blade sections of the 65 series have been used successfully as root sections on many rotors, including high-flow designs. The low-speed cascade turning-angle data of references 1 and 2 have been adequate for the design of most root sections, since reference 3 has indicated that measured low-speed turning angles are satisfactory for design purposes for speeds up to critical. Reference 3 also showed that higher speeds would decrease the low-drag angle-of-attack range and change the low-speed design angle of attack. Although the throat area determines the maximum entering Mach number, the blade profile losses may increase at an appreciably lower Mach number. Therefore, high-speed cascade tests of typical hub sections were made to establish design information for 65-series hub sections.

In order to determine whether a more efficient blade passage might be designed by having a passage area distribution different from that of the 65 series, a blade section was devised of circular arcs and tested. In these tests, the throat was varied from a position near the leading edge to a position near midchord. At one angle of attack, the passage was of constant area for the first half of its length.

SYMBOLS

A	flow area
c	blade chord
C_{l_o}	camber, expressed as design lift coefficient of isolated airfoil
C_w	momentum-loss coefficient
F_c	ratio of wake momentum loss to integrated total-pressure loss in wake
M	Mach number
p	static pressure
P	total pressure
q	dynamic pressure, $\frac{1}{2}\rho V^2$
s	tangential spacing between blades

S pressure coefficient, $\frac{p_1 - p_l}{q_1}$

V velocity

w wake width

α angle of attack (angle between entering flow direction and chord)

β air angle measured from perpendicular to blade row

δ wake blockage

θ turning angle

ρ density

σ solidity (chord-spacing ratio), c/s

Subscripts:

1 upstream of blade row (in undisturbed stream)

2 downstream of blade row

cr critical (condition of first attainment of sonic velocity on blade surface)

l local (as on blade surface)

T throat of blade passage

APPARATUS AND METHODS

Apparatus

The blades were tested in a 7-inch high-speed cascade tunnel at the Langley Laboratory, shown schematically in figure 1. The tunnel is designed to produce two-dimensional flow through the cascade, that is, no spanwise convergence or divergence of the stream tubes. For this purpose, protruding boundary-layer-removal slots are contained in the four tunnel walls upstream of the blade row, and the blade-passage end walls are of a porous material that permits flow removal to maintain the two-dimensionality. The tunnel is capable of producing Mach numbers from low speed to choking. The apparatus is described more completely

in reference 3. The blade models had a 7-inch span and $3\frac{1}{2}$-inch chord. Seven blades were used in all tests, and flexible fairings were used on both top and bottom walls to simulate an infinite series of blades.

Test Procedure

The same test procedure and instrumentation were used as that described more completely in reference 3. Briefly, two-dimensional flow was established by controlling the amount of flow removed through the porous side walls. Thus, velocity and pressure changes across the cascade were made to conform to values calculated from turning angle, Mach number, and wake measurements. With the two-dimensional flow conditions established, the blade-surface static pressures, upstream and downstream flow angles and pressures, and total-pressure loss in the wake were recorded.

The tests were run at the two-dimensional flow condition wherever possible. Usually, as the blade passages choked, two-dimensional flow could not be achieved. Blade turning angles change as the pressure rise across the cascade is varied from two-dimensional, usually increasing as the pressure rise decreases. To indicate the magnitude of this change, two test points approximately at critical speed, one having pressure rise greater and one less than two-dimensional, were recorded. All test points not having a minimum of 90 percent of the two-dimensional pressure rise are not considered to be two-dimensional and the data are marked accordingly.

Reduction of Data

A momentum-loss coefficient was calculated from the measured total-pressure loss by the method of reference 4 for calculating drag. Momentum loss was calculated from the downstream conditions and is expressed in coefficient form based on the dynamic pressure upstream of the cascade. Hence,

$$C_{w_1} = F_c \int_0^w \frac{P_1 - P_2}{q_1 c} \, dw$$

where F_c (determined from ref. 4) is the ratio of the momentum-loss coefficient to the total-pressure-loss coefficient for an assumed wake shape as a function of the maximum total-pressure loss and Mach number.

A calculated check of the two-dimensionality of the flow was made for all tests. Tests are considered two-dimensional if the test pressure rise $\frac{p_2 - p_1}{q_1}$ is greater than 90 percent of the ideal pressure rise calculated from the entering Mach number, inlet-air angle, turning angle, and wake blockage of the particular test. The values of wake blockage for a number of tests were calculated and plotted against the integrated total-pressure loss and the following relationship for the wake blockage δ was indicated:

$$\frac{\delta}{c} = 0.51 \int_0^w \frac{P_1 - P_2}{q_2 c} dw$$

The ideal pressure rise was obtained from this displacement thickness and isentropic relationships. This ideal pressure rise was compared with the measured pressure rise to determine whether the tests were to be considered two-dimensional.

BLADE DESIGN, TESTS, AND PRESENTATION OF RESULTS

Blade Design

Minimum, or throat, passage areas for the 65-series blade configurations typical of compressor hub sections are near the leading edge. In order to determine whether a more efficient passage might be obtained by using a different passage area distribution or by having the maximum thickness and throat farther rearward, a special blade section of circular arcs was designed. This blade section, referred to in this report as the circular-arc blade section and shown in figure 2(a), consists of three circular arcs, one on the upper surface and two on the lower. The blade was so designed that at a solidity of 1.5 and $(\beta_1 - \alpha) = 10.3^\circ$ the arc forming the leading edge of the lower surface of the upper blade was concentric with the arc forming the upper surface of the lower blade. Thus, at this condition, the passage area was constant from the leading edge to the 37-percent-chord point on the lower surface and the 50-percent-chord point on the upper surface. (See fig. 2(b).) For $(\beta_1 - \alpha) > 10.3^\circ$, the throat was at the leading edge and the passage opened to the rear; for $(\beta_1 - \alpha) < 10.3^\circ$, the passage converged from the leading edge rearward to beyond the middle of the passage and then diverged. The blades for these conditions are

referred to as configuration I. By reversing the blade sections (trailing edge to leading edge) another configuration, referred to as configuration II, was obtained. The throat at $(\beta_1 - \alpha) = 11^\circ$ was between the 41-percent-chord point on the upper surface of the lower blade and the 27-percent-chord point on the lower surface of the upper blade, and hence the throat was not so far rearward as for configuration I. From tests of these configurations, it was hoped to determine the better passage area distribution.

Blade Tests

Blade sections of the 65 series, 10 percent thick for structural reasons, were selected for these tests. Cambers from $C_{l_o} = 1.2$ to $C_{l_o} = 2.1$, solidity values of 1.5 and 1.25, and inlet-flow angles from 25° to 45° were investigated. Each configuration was tested over a range of angle of attack determined by the rising losses at high and low angles of attack. The circular-arc blade section was tested both forward and backward (configuration I and configuration II) at a solidity of 1.5 and inlet-flow angles of both 25° and 35°. All configurations tested are listed in table I.

Presentation of Results

Parts (a) to (d) of figures 3 to 78 give, for each angle of attack tested, pressure distributions measured at four Mach numbers. On each pressure distribution, the maximum blade-surface Mach number is given and the downstream static pressure is indicated by the 100-percent-chord point even though this pressure was measured about 1 chord length downstream of this point. Part (e) of these figures presents the variation on turning angle, momentum loss, and pressure rise with Mach number. Figures 79 to 90 are plots of turning angle against angle of attack. Where available, low-speed turning angles from reference 1 or 2 are plotted for comparison. Figures 91 to 102 are plots of momentum loss against angle of attack at various constant Mach numbers. Between angles of attack, anticipated increases in momentum loss due to choking are shown as dashed lines. Figures 103 and 104 show the throat-area variation with maximum entering Mach number, and figure 105 indicates the difference between the low-speed design angle of attack and the high-speed angle of attack for minimum losses. Figure 106 shows schlieren photographs of one blade configuration.

DISCUSSION OF RESULTS

65-Series Blade Tests

Turning angle.- The variation of the measured turning angle with Mach number is shown for each blade configuration tested in figures 3 to 48. In figures 79 to 86, these turning angles are plotted against angle of attack for two Mach numbers, $M_1 = 0.3$ and critical Mach number. It may be seen that the difference between the turning angle measured at a low Mach number ($M_1 = 0.3$) and that measured at a typical blade operating speed (critical) is seldom greater than 1.0°. These measured turning angles also agree well with the measured or interpolated turning angles of reference 1 or 2 (see fig. 81 and figs. 83 to 86 for this comparison). Hence, the results of reference 3, which indicated that for 65-series blade sections the turning angles measured at low speed are sufficiently accurate for design purposes, are found to be equally applicable to typical hub sections.

Above critical speed, shocks forming on blade surfaces usually alter blade-surface boundary layers unfavorably by causing separation to occur farther forward on the blade and decreasing the turning angle. At high inlet-flow angles, the turning angle decreased abruptly upon formation of a strong blade-surface shock (see ref. 3). However, for typical root sections, the drop in turning angle tended to be small. Some tests showed no change, and in tests of the 65-$(21A_{10})$10 section (see figs. 25 to 27) the turning angle increased.

Blade passage choking.- For root sections, the minimum passage area (throat) is critical and frequently limits the entering Mach number. For typical root configurations of 65-series blade sections, the minimum, or throat, area is just inside the blade passage and extends from about the 5-percent-chord point on the lower surface to about the 25-percent-chord point on the upper surface. At the higher blade-setting angles tested (where $\beta_1 = 45^\circ$), the throat is a little farther rearward. The minimum-pressure point on the upper surface is seldom at the throat. The blade-surface velocity is usually slightly above sonic at the throat and increases behind the throat until a shock occurs. If the minimum pressure is ahead of the throat at low speed, a second peak velocity is sometimes present just behind the throat. On the lower surface, the minimum pressure and the shock (when it occurs) are almost at the leading edge, although increasing the pressure ratio across the cascade sometimes shifts this point downstream.

Passage areas for the 65-$(C_{l_o} A_{10})$10 blade sections are given in reference 3. A maximum entering Mach number may be calculated from the passage area, and although this Mach number represents the maximum obtainable, choking was expected to occur before this Mach number was reached. Such choking may be due to either losses ahead of the throat or high curvature of the blade surfaces at the extremities of the throat. In figure 103, the maximum entering Mach number measured in each test is plotted against the passage area ratio for the particular configuration. It can be seen that the entering Mach numbers for blade configurations with smaller throat areas more closely approach the theoretical maximum than do those for more open configurations. The small-throat configurations usually have small inlet flow angles with the throat located between the lower surface and a point well forward on the upper surface. More open configurations tend to occur when the inlet flow angles are large and the minimum passage is located between the lower-surface leading edge and an upper-surface point located farther rearward. Thickening of the boundary layer or separation along the blade upper surface forward of the minimum passage would produce choking at lower flows than the open area would indicate. Thus, having the throat nearer the trailing edge appears to cause choking at flow rates considerably below the theoretical maximum.

Upstream flow variation.- Compressibility effects at the test Mach numbers produce apparent variations in the upstream flow which alter the pressure distributions and make the angle of attack appear to decrease at higher Mach numbers. The variations are caused by the disproportionate increase in velocity in the throat region near choke and the increased interference of other blade sections with increase in speed. These effects are discussed in more detail in reference 3. Typical examples of this apparent decrease in angle of attack can be seen in figures 3, 16, 29, and 46.

Momentum-loss variation.- At low speed, losses increase at both high and low angles of attack because peak velocities produced by angle of attack require too great a blade-surface pressure rise for the boundary layer. Since high speeds accentuate peaked blade-surface pressures and any tendency of the boundary layer to separate, larger losses were expected and were obtained at high speeds. The increased losses obtained at both high and low angles of attack thus reduced the low-loss angle-of-attack range. (See figs. 91 to 98.) Compressibility and shocks may alter pressure distributions, as in the condition of the choked throat with the shock behind it. The throat limits the entering Mach number, and increasing the pressure ratio across the blade row only increases the strength of the shock behind the throat. The shock not only will have a total-pressure loss but also will separate the boundary layer and thus cause very high losses. Increasing the angle of attack opens the throat and allows higher entering Mach numbers

before the high losses of the choked condition occur. In figures 91 to 98, the low-loss range of angle of attack is decreased more on the low angle-of-attack side as the Mach number increases. Hence, the low-loss range of angle of attack and design angle of attack measured at low speeds may have little significance at high speeds. The selection of higher design angles of attack for high-speed root sections appears feasible and very desirable.

New angles of attack selected from low-drag ranges at critical speed for the 65-series blade tests are plotted in figure 105 as the difference between the low-speed design angle of attack (ref. 2) and the new angle of attack. Results for 65-series blades tested in reference 3 are also plotted. A considerable shift in the optimum angle of attack has occurred at critical speed. For low inlet-flow angles, this shift is approximately 6°. An even greater shift would be evident at a higher Mach number.

Circular-Arc Blade-Section Tests

The circular-arc blade section was designed for the investigation of the effects of passage area distribution on the flow. Configuration I was so constructed that the forward part of the passage between two blades would be formed by two concentric arcs, which would maintain a constant flow-passage area. The two particular conditions that give constant-area passages are $\beta_1 = 35^\circ$ and $\alpha = 24.7^\circ$, and $\beta_1 = 25^\circ$ and $\alpha = 14.7^\circ$. However, at the lower inlet air angle, the constant-area passage did not occur at a useful angle of attack. At higher angles of attack, a throat exists in the passage near the midchord point, and the passage converges ahead of the throat and diverges rearward of the throat. At lower angles of attack, the throat is located at the leading edge and the passage diverges for its entire length. Configuration I operated best at an angle of attack at which the passage throat was near the midchord point of the blade. This angle of attack was sufficiently large to prevent a peaked velocity from occurring on the lower surface at the nose, as happened at lower angles of attack. The better blade performance at the high angles of attack may not be entirely attributable to the shift of the throat position from the leading edge or to the lower-surface peak velocity. Increasing the angle of attack in the cascade tests increased the throat area, and therefore higher measured entering Mach numbers could be expected. Figure 100 indicates the center of the high-speed low-loss region for $\beta_1 = 35^\circ$ to be at $\alpha = 27.2^\circ$, for which the passage area ratio A_T/A_1 is 1.03. For $\beta_1 = 25^\circ$, the center was at $\alpha = 23.2^\circ$ and A_T/A_1 was 0.94.

Configuration II (blade sections reversed, leading edge to trailing edge) was tested at $\beta_1 = 25^\circ$ and 35°. At low angles of attack ($\beta - \alpha$ greater than 14°) the throat was at the leading edge. For higher angles the throat was farther rearward, and it was just ahead of the midchord position at the highest angles of attack tested. Best high-speed performance was obtained at an angle of attack of about 28°. At this angle, the throat was at the quarter-chord position on the lower surface when β_1 was 35° and at the midchord position when β_1 was 25°. For configuration I the better high-speed performance at high angles of attack may be due to the increase in throat area as well as the change in the position of the throat. Nevertheless, for both configurations, the flow over the upper surface at the leading edge did not begin to deteriorate until after the throat had moved from the leading edge.

The maximum test Mach numbers obtained with various throat areas are compared with the maximum theoretical Mach number in figure 104. A trend similar to that plotted for the 65-$\left(C_{l_o} A_{10}\right)$10 blade sections is apparent. The Mach numbers for the circular-arc blade sections are nearer the theoretical maximum.

Pressure distributions for both configurations I and II frequently show a uniform pressure on the upper surface from the 80- or 90-percent-chord point to the trailing edge. (See fig. 75.) The pressures near the trailing edge on both surfaces usually were lower than the static pressure measured approximately 1 chord length downstream. This difference in pressure was particularly great at choke flow (see fig. 57(d), for example). Schlieren photographs were made of configuration I with the typical condition $\beta_1 = 35^\circ$, $\sigma = 1.5$, and $\alpha = 24.2^\circ$. Very wide wakes are seen in the schlieren photographs (fig. 106). At all Mach numbers, the flow appears to separate from the upper surface at about the 75-percent-chord point. Wake width appears to decrease farther downstream and the mixing of the wake produces the static-pressure rise between the blade trailing edge and the downstream orifices. The very large pressure rise at the highest Mach number is caused by the normal shock located downstream of the blade passage (see fig. 106(d)).

On the same blade configuration, an investigation of the blade-surface boundary layer was made by using a total-pressure probe connected to a small soundproof cell containing a microphone. The noise level readily indicated the condition of the boundary layer and the separation point. This test was necessarily made at low speed. Over the lower surface, the boundary layer was laminar to the midchord point and then turbulent to the trailing edge. No separation was detected on the lower surface. A very thin turbulent boundary layer extended from the leading edge to the midchord point on the upper surface. This

turbulent boundary layer thickened between the 40-percent-chord and 65-percent-chord points. Behind the 65-percent-chord point, the flow separated until at the trailing edge a quiet region of very little flow was reached.

A 1/4-inch-mesh screen was placed against the leading edges of the blades to increase the turbulence. The lower-surface boundary layer was then turbulent from the leading edge to the trailing edge and without separation. On the upper surface from the leading edge to about the 20-percent-chord point, the boundary-layer turbulence was the same as that of the free stream; however, rearward of this area the boundary layer became very turbulent and relatively thick. This condition prevailed almost to the trailing edge. The quiet separated region that existed at the trailing edge in the previous test still existed after the screen was put in. However, the extent of this region and the separation was considerably reduced by increasing the turbulence.

SUMMARY OF RESULTS

High-speed cascade tests were made of the NACA 65-$(C_{l_o} A_{10})$10 blade section and a blade section devised from circular arcs at typical compressor-blade hub-section operating conditions. From these tests and previously reported low-speed and high-speed tests, the following results are summarized:

1. Turning angles measured in low-speed tests of the 65-series blade sections are sufficiently accurate for design purposes at speeds up to critical.

2. The angle of attack for best operation at high Mach numbers is higher than the design angle of attack selected to have low-speed pressure distributions that are free of peaks. The amount by which the best operating angle is higher is determined by the throat area ratio and is greatest at low inlet angles.

3. The decrease in the angle-of-attack range for low losses at high Mach numbers is due largely to choking of the blade passages, which are smaller at low angles of attack.

4. In the investigation of the circular-arc blade configuration, the best performance was obtained with the minimum or throat area rearward in the passage rather than at the leading edge.

Langley Aeronautical Laboratory,
National Advisory Committee for Aeronautics,
Langley Field, Va., July 18, 1957.

REFERENCES

1. Herrig, L. Joseph, Emery, James C., and Erwin, John R.: Systematic Two-Dimensional Cascade Tests of NACA 65-Series Compressor Blades at Low Speeds. NACA TN 3916, 1957. (Supersedes NACA RM L51G31.)

2. Felix, A. Richard: Summary of 65-Series Compressor-Blade Low-Speed Cascade Data by Use of the Carpet-Plotting Technique. NACA TN 3913, 1957. (Supersedes NACA RM L54H18a.)

3. Dunavant, James C., Emery, James C., Walch, Howard C., and Westphal, Willard R.: High-Speed Cascade Tests of the NACA 65-$\left(12A_{10}\right)$10 and NACA 65-$\left(12A_2I_{8b}\right)$10 Compressor Blade Sections. NACA RM L55I08, 1955.

4. Heaslet, Max. A.: Theoretical Investigation of Methods for Computing Drag From Wake Surveys at High Subsonic Speeds. NACA WR W-1, 1945. (Formerly NACA ARR 5C21.)

TABLE I.- CASCADE CONFIGURATIONS TESTED

Blade Section	Figure	Angle of attack, α, deg	Inlet air angle, β_1, deg	Solidity, σ
NACA 65-$(12A_{10})$10	3	12.6	25	1.5
	4	15.6		
	5	18.6		
	6	21.6		
	7	24.6		
	8	27.6		
NACA 65-$(15A_{10})$10	9	11.8		
	10	14.8		
	11	17.8		
	12	20.8		
	13	23.8		
	14	26.8		
NACA 65-$(18A_{10})$10	15	15.5	35	
	16	18.5		
	17	21.5		
	18	24.5		
	19	27.5		
	20	30.5		
NACA 65-$(21A_{10})$10	21	20.5		
	22	23.5		
	23	26.5		
	24	29.5		
	25	32.4		
	26	35.4		
	27	38.4		
NACA 65-$(12A_{10})$10	28	11.1	35	1.25
	29	14.1		
	30	17.1		
	31	20.1		
	32	23.1		
NACA 65-$(15A_{10})$10	33	10.3		
	34	13.3		
	35	16.3		
	36	19.3		
	37	22.3		
	38	24.8		

TABLE I.- CASCADE CONFIGURATIONS TESTED - Concluded

Blade Section	Figure	Angle of attack, α, deg	Inlet air angle, β_1, deg	Solidity, σ
NACA 65-$(12A_{10})$10	39	11.1	45	1.25
	40	14.1		
	41	17.1		
	42	20.1		
	43	23.1		
NACA 65-$(15A_{10})$10	44	10.3		
	45	13.3		
	46	16.3		
	47	19.3		
	48	22.3		
Circular-arc configuration I	49	11.2	25	1.5
	50	14.2		
	51	17.2		
	52	20.2		
	53	23.2		
	54	26.2		
	55	29.2		
	56	32.2		
	57	35.2		
	58	12.2	35	
	59	15.2		
	60	18.2		
	61	21.2		
	62	24.2		
	63	27.2		
	64	30.2		
	65	33.2		
	66	36.2		
Circular-arc configuration II	67	14.8	25	
	68	17.8		
	69	20.8		
	70	23.8		
	71	26.8		
	72	29.8		
	73	15.8	35	
	74	18.8		
	75	21.8		
	76	24.8		
	77	27.8		
	78	30.8		

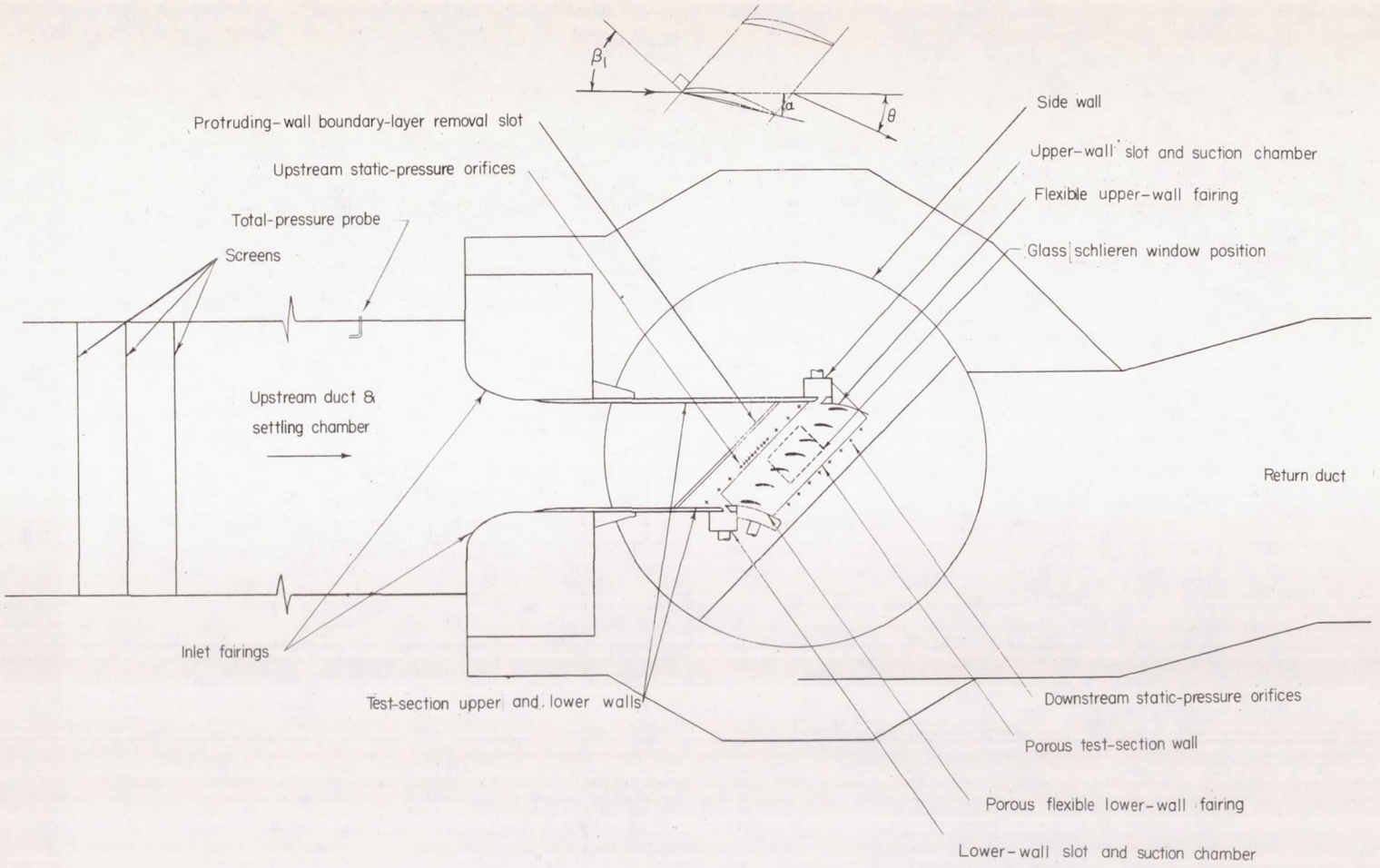
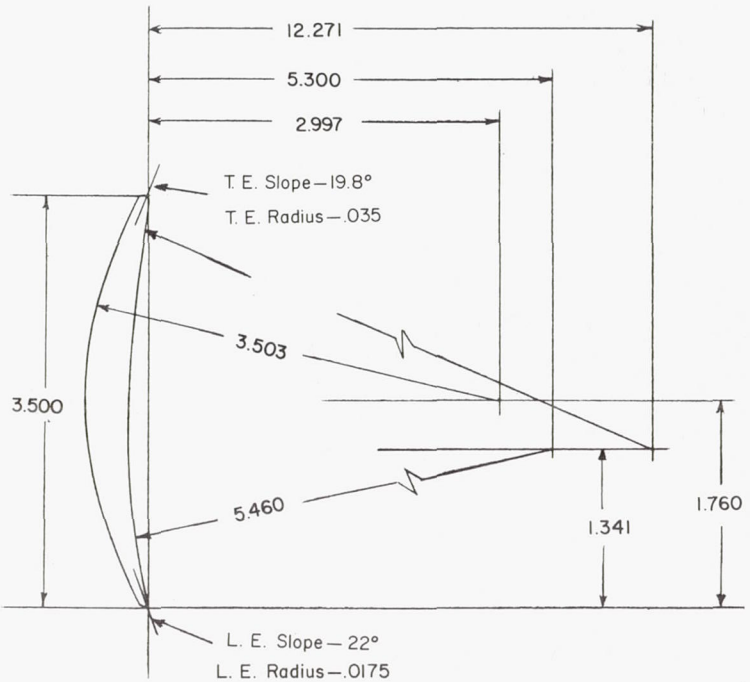
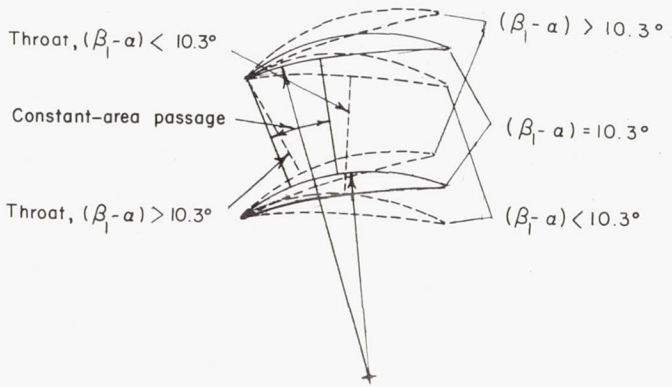


Figure 1.- Cross-sectional view of the 7-inch high-speed cascade tunnel used in tests.



(a) Blade dimensions (inches).



(b) Blade passage, configuration I.

Figure 2.- Circular-arc blade.

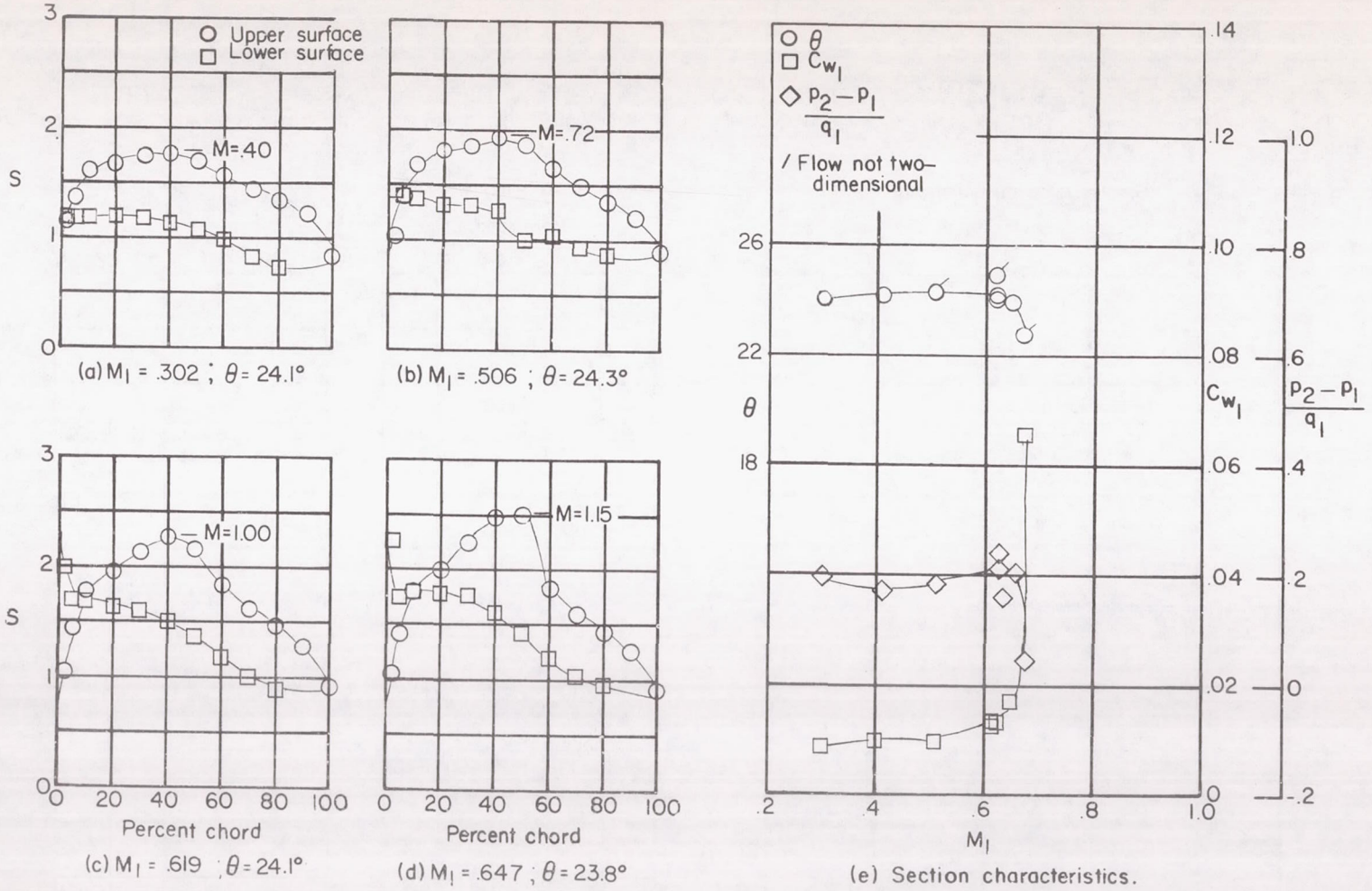


Figure 3.- Blade-surface pressure distributions and section characteristics for the cascade combination $\beta_1 = 25°$, $\sigma = 1.5$, $\alpha = 12.6°$, and NACA 65-$(12A_{10})$10 blade section.

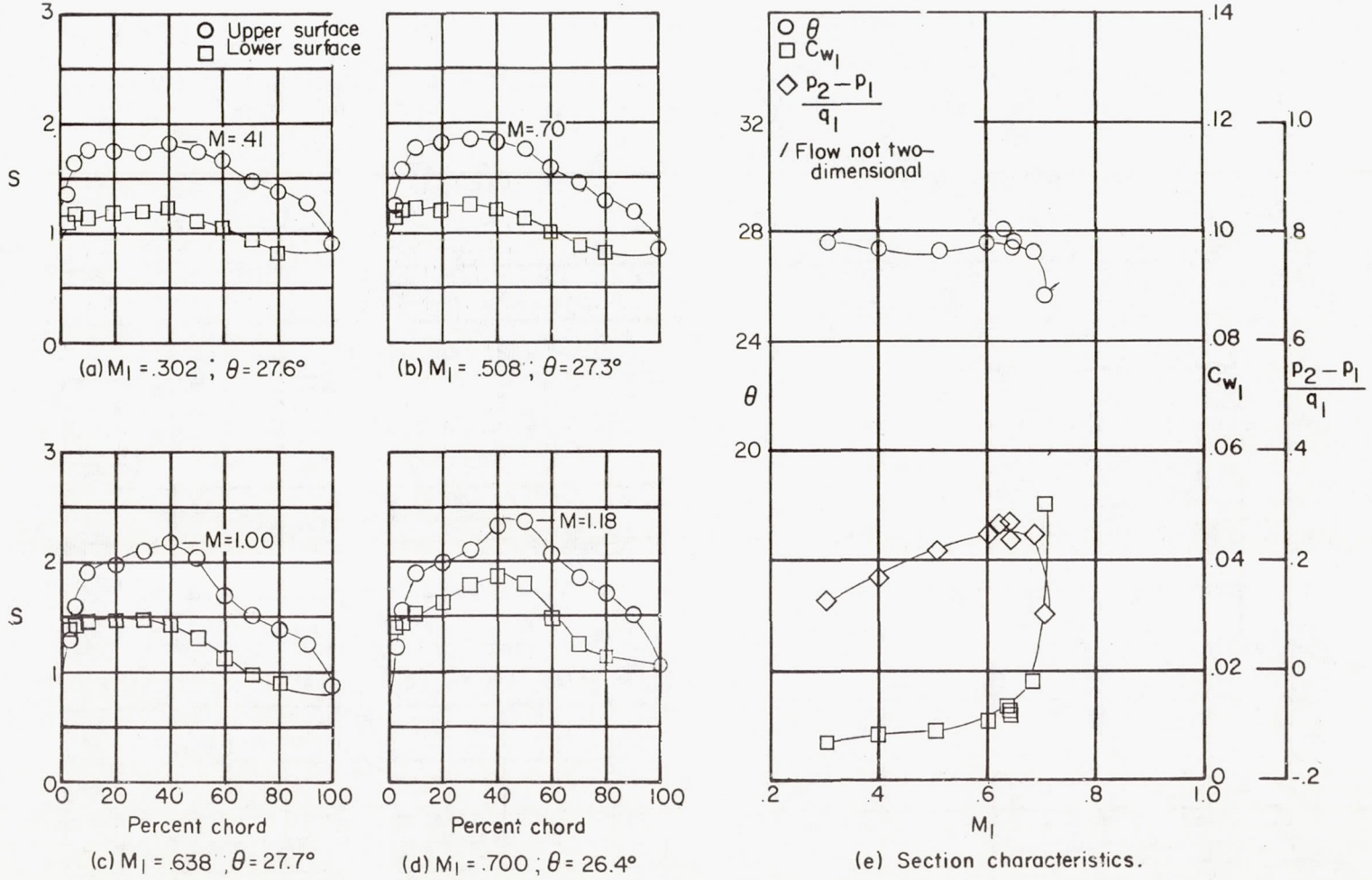


Figure 4.- Blade-surface pressure distributions and section characteristics for the cascade combination $\beta_1 = 25^\circ$, $\sigma = 1.5$, $\alpha = 15.6^\circ$, and NACA 65-($12A_{10}$)10 blade section.

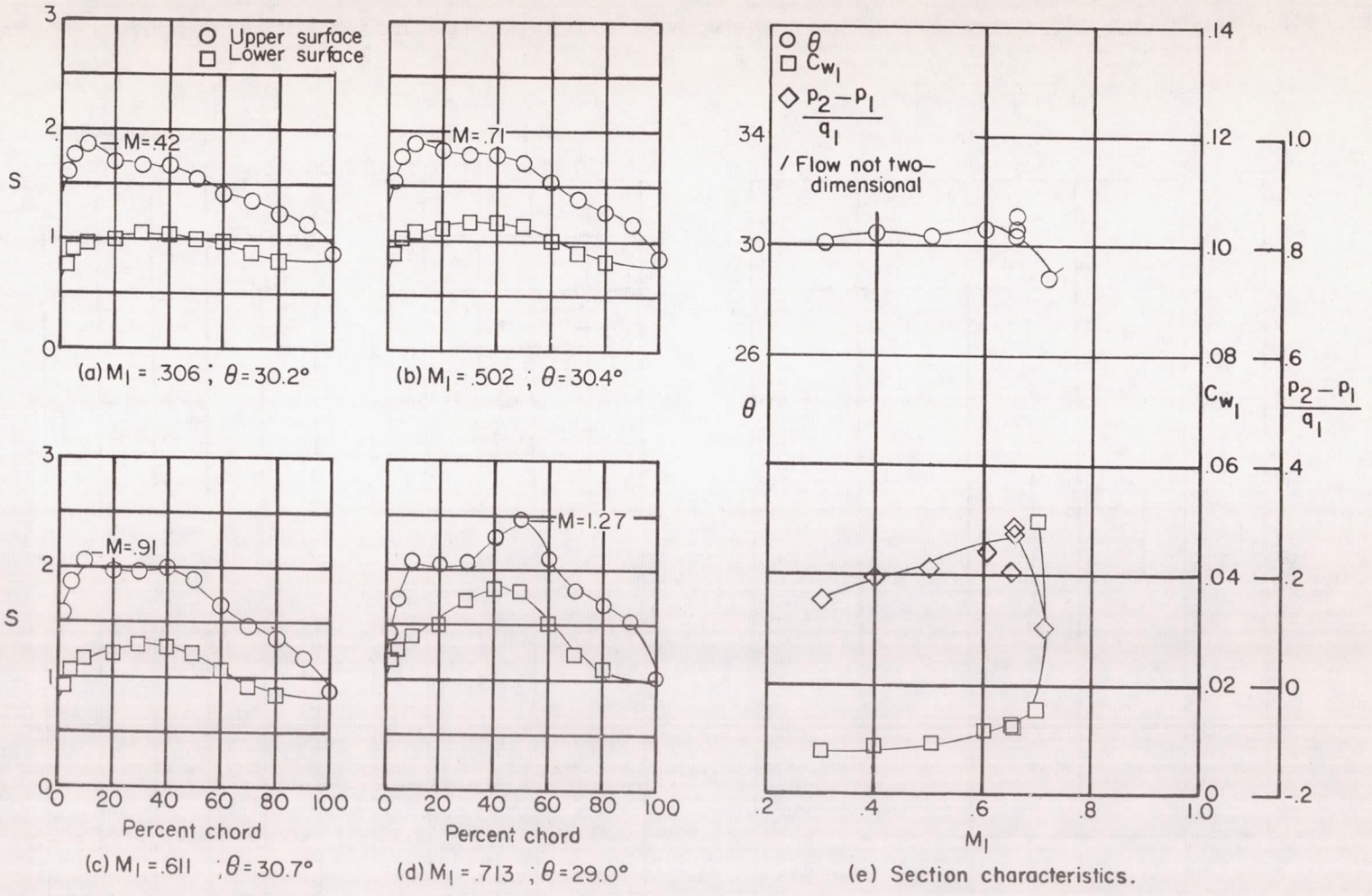


Figure 5.- Blade-surface pressure distributions and section characteristics for the cascade combination $\beta_1 = 25°$, $\sigma = 1.5$, $\alpha = 18.6°$, and NACA 65-($12A_{10}$)10 blade section.

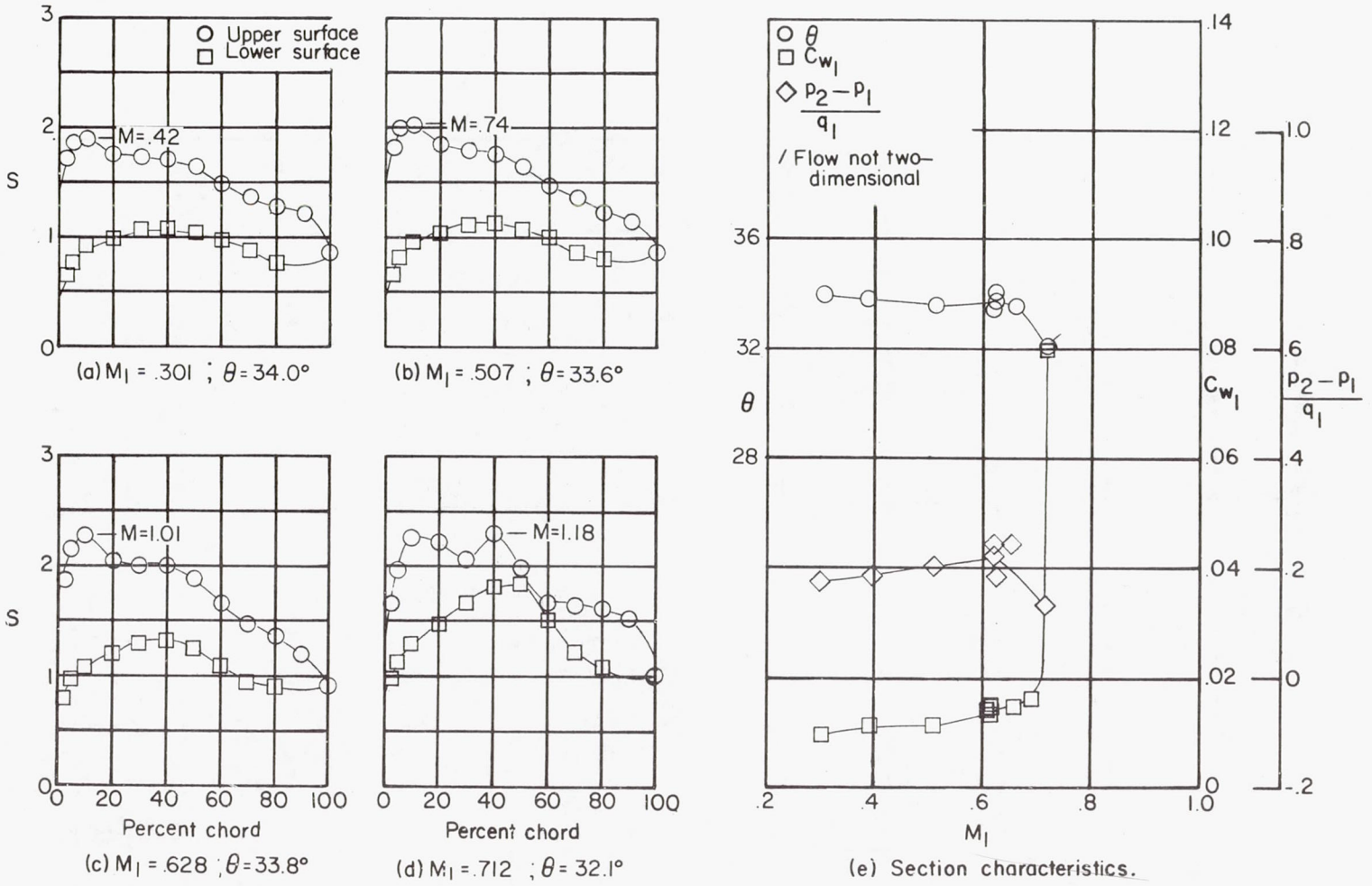


Figure 6.- Blade-surface pressure distributions and section characteristics for the cascade combination $\beta_1 = 25^\circ$, $\sigma = 1.5$, $\alpha = 21.6^\circ$, and NACA 65-$(12A_{10})$10 blade section.

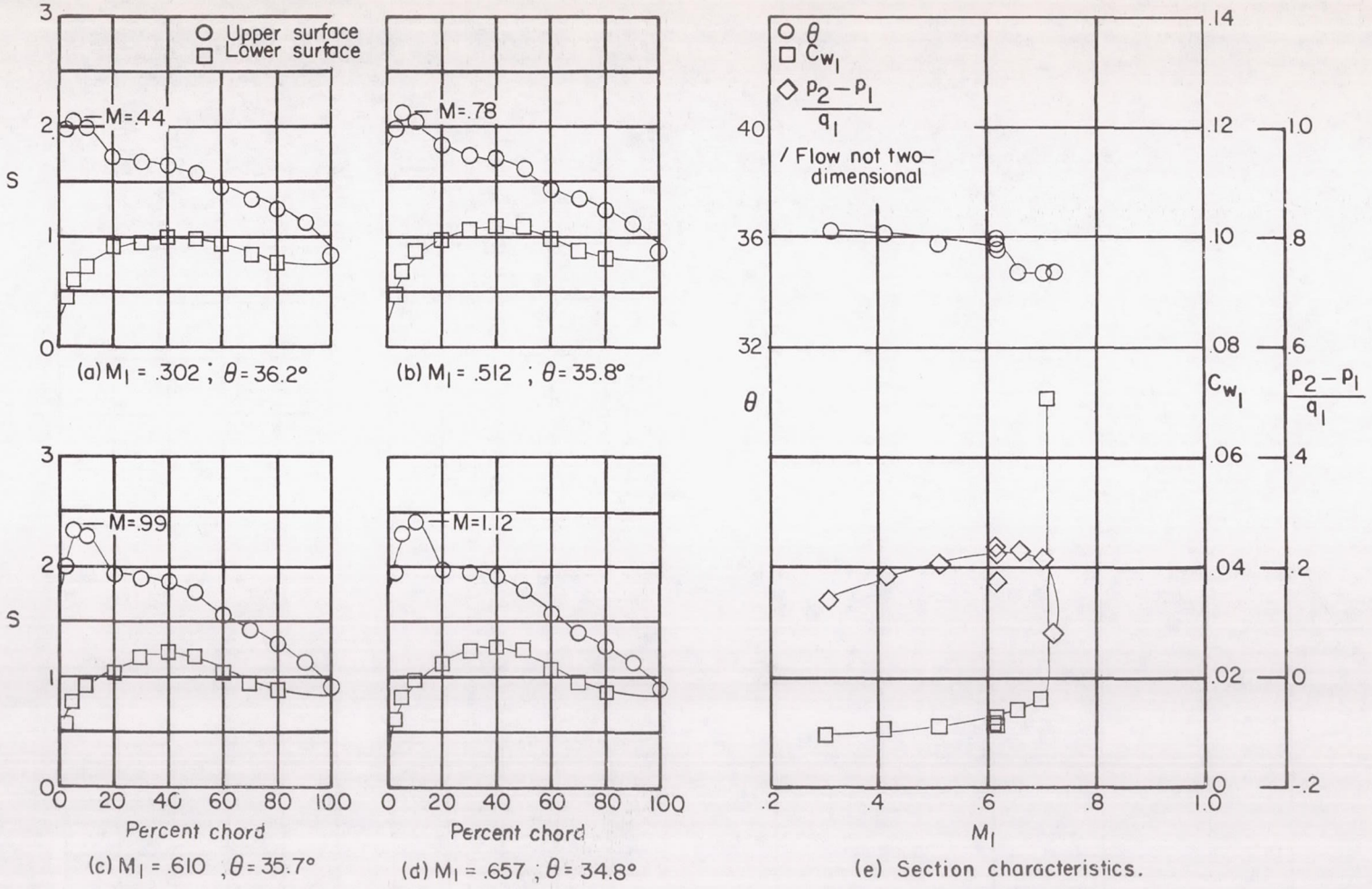


Figure 7.- Blade-surface pressure distributions and section characteristics for the cascade combination $\beta_1 = 25°$, $\sigma = 1.5$, $\alpha = 24.6°$, and NACA 65-($12A_{10}$)10 blade section.

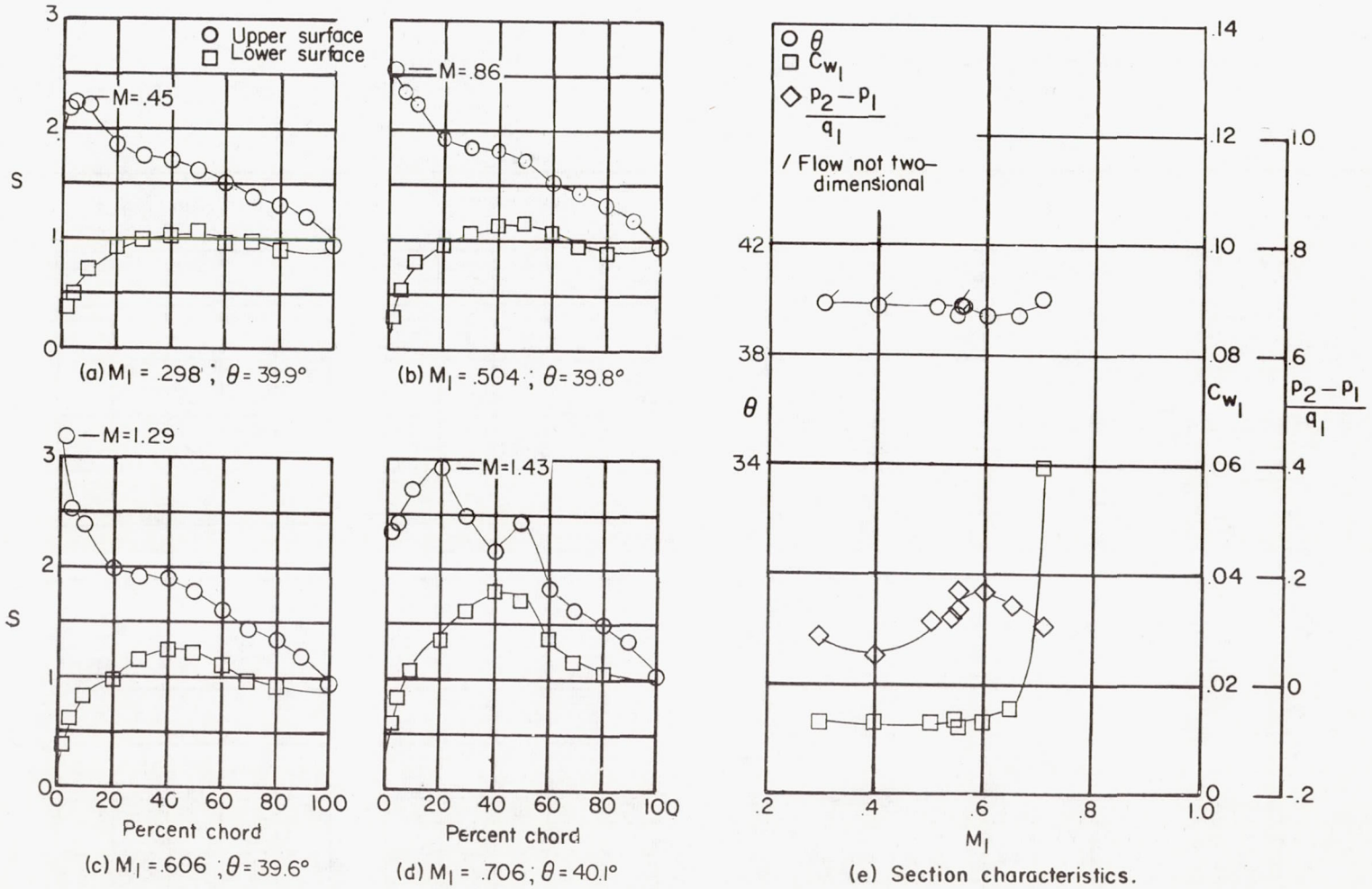


Figure 8.- Blade-surface pressure distributions and section characteristics for the cascade combination $\beta_1 = 25°$, $\sigma = 1.5$, $\alpha = 27.6°$, and NACA 65-($12A_{10}$)10 blade section.

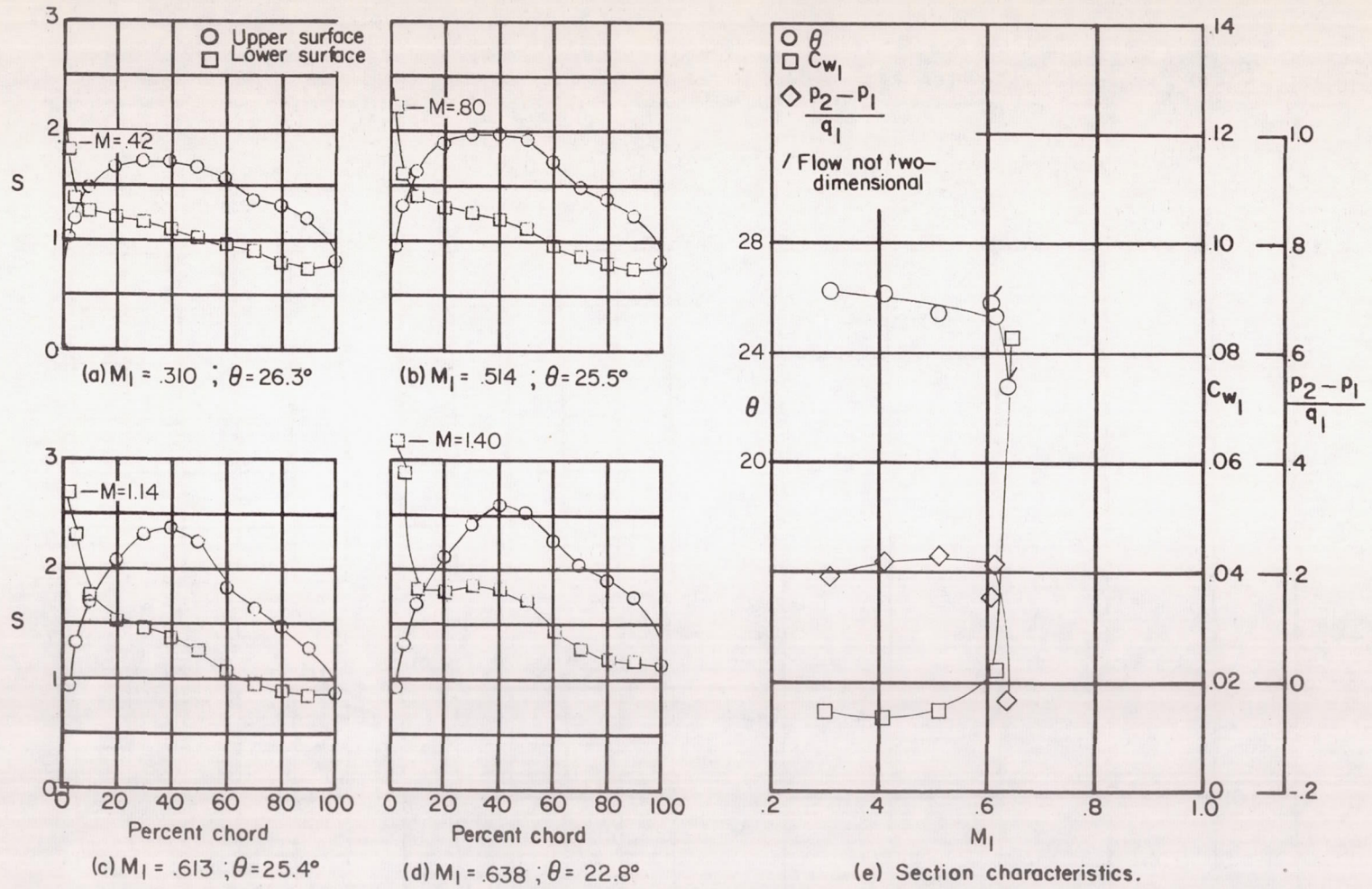


Figure 9.- Blade-surface pressure distributions and section characteristics for the cascade combination $\beta_1 = 25^\circ$, $\sigma = 1.5$, $\alpha = 11.8^\circ$, and NACA 65-($15A_{10}$)10 blade section.

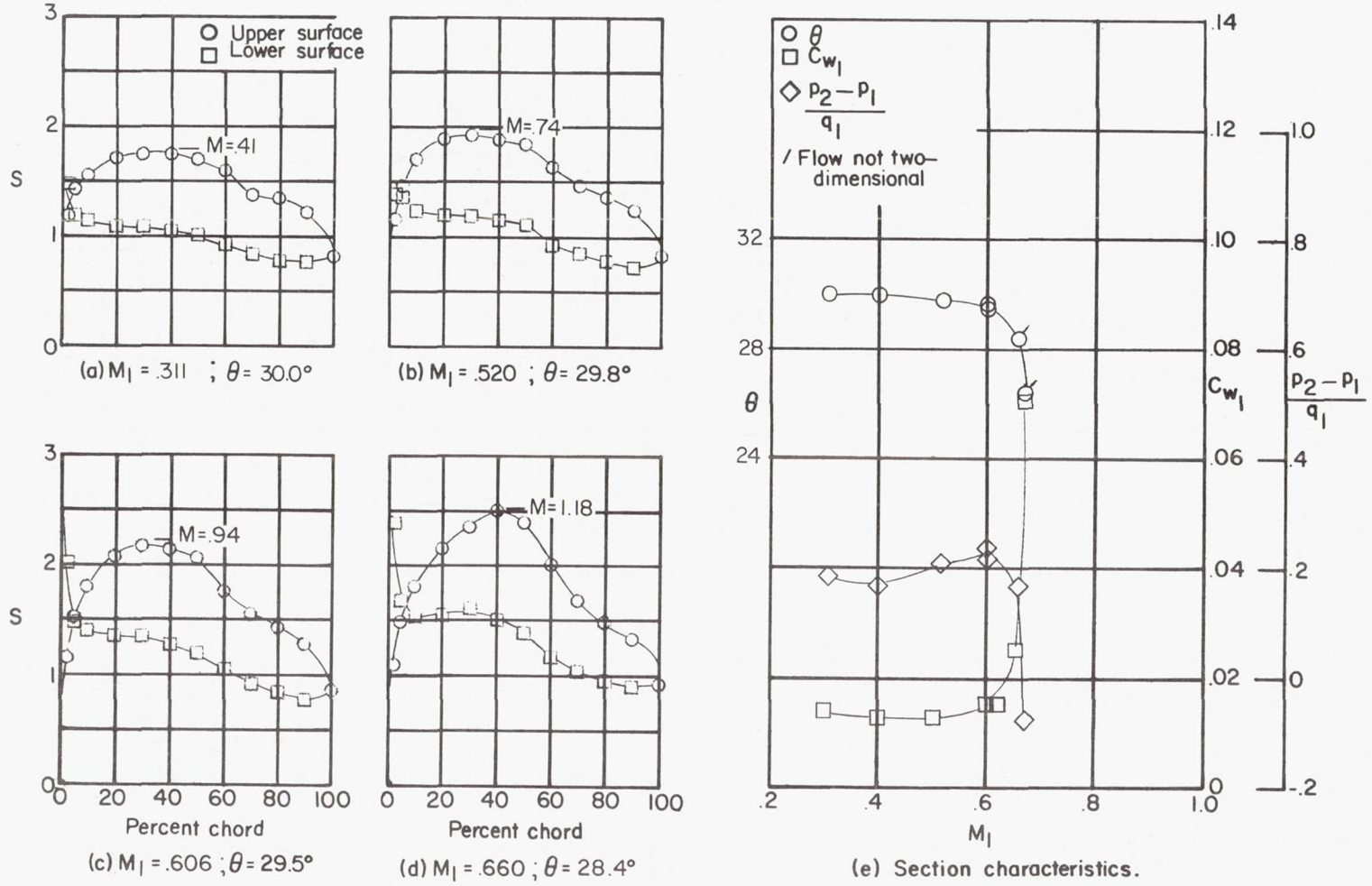


Figure 10.- Blade-surface pressure distributions and section characteristics for the cascade combination $\beta_1 = 25°$, $\sigma = 1.5$, $\alpha = 14.8°$, and NACA 65-($15A_{10}$)10 blade section.

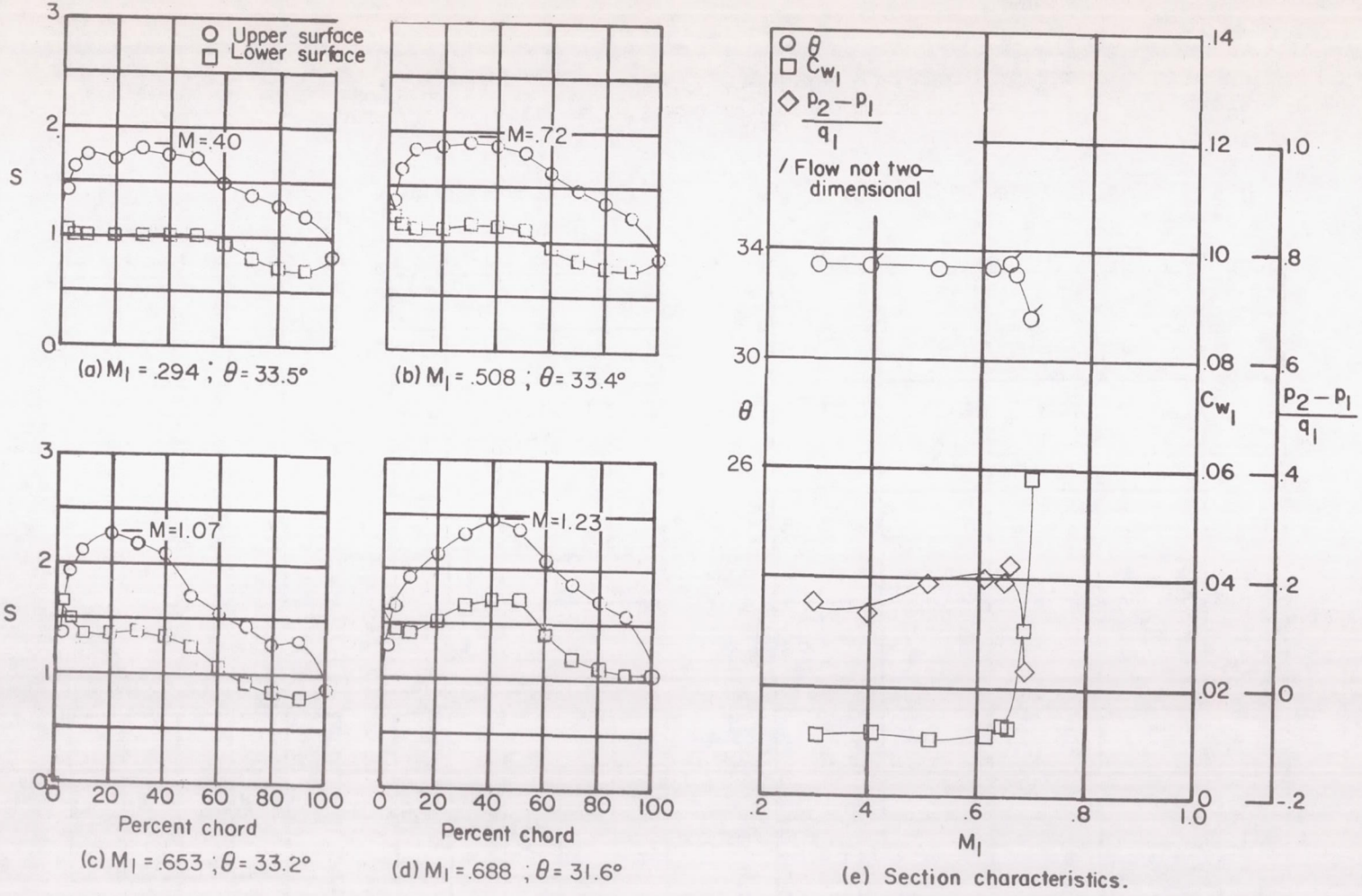


Figure 11.- Blade-surface pressure distributions and section characteristics for the cascade combination $\beta_1 = 25°$, $\sigma = 1.5$, $\alpha = 17.8°$, and NACA 65-($15A_{10}$)10 blade section.

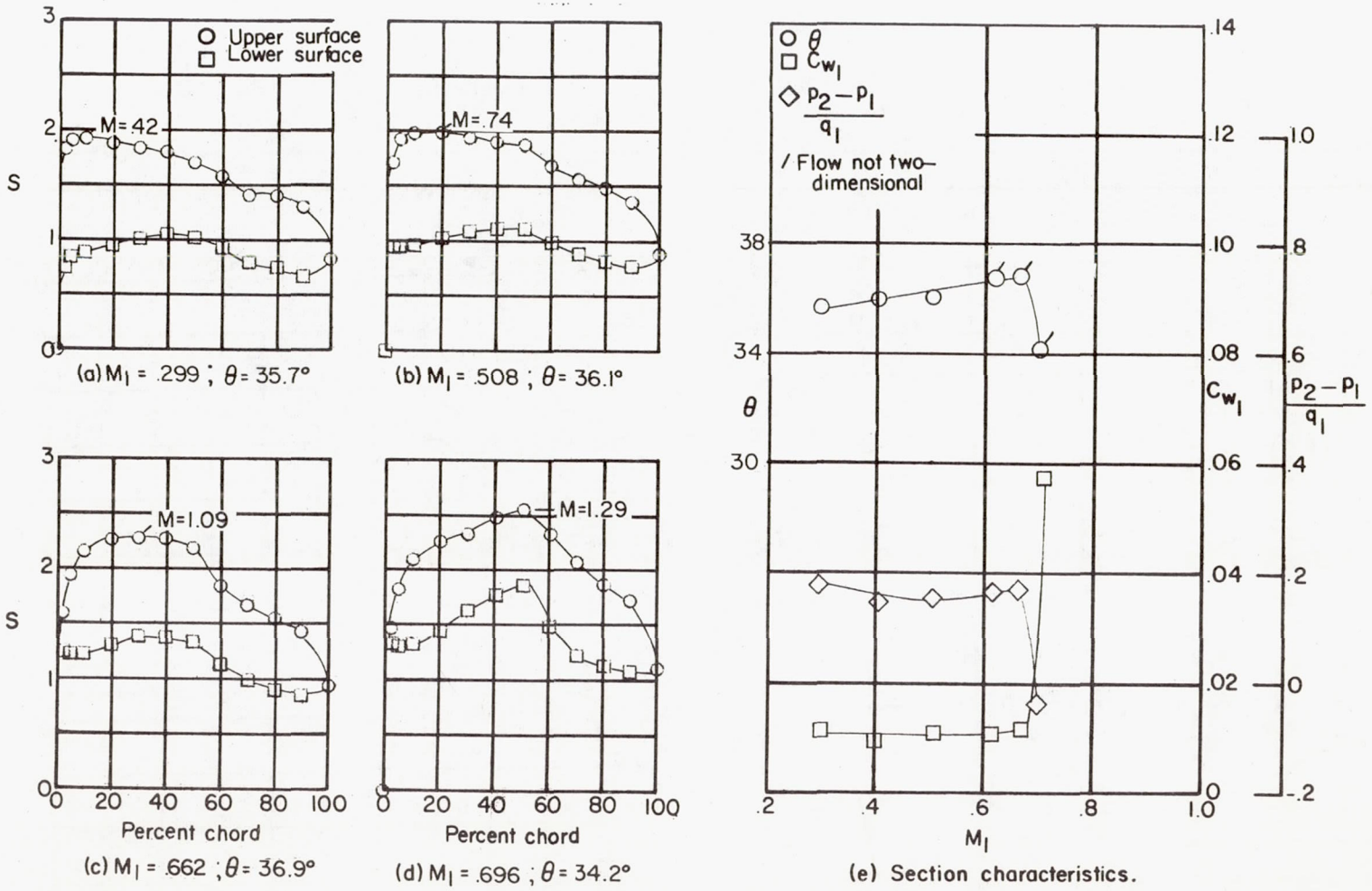


Figure 12.- Blade-surface pressure distributions and section characteristics for the cascade combination $\beta_1 = 25^\circ$, $\sigma = 1.5$, $\alpha = 20.8^\circ$, and NACA 65-($15A_{10}$)10 blade section.

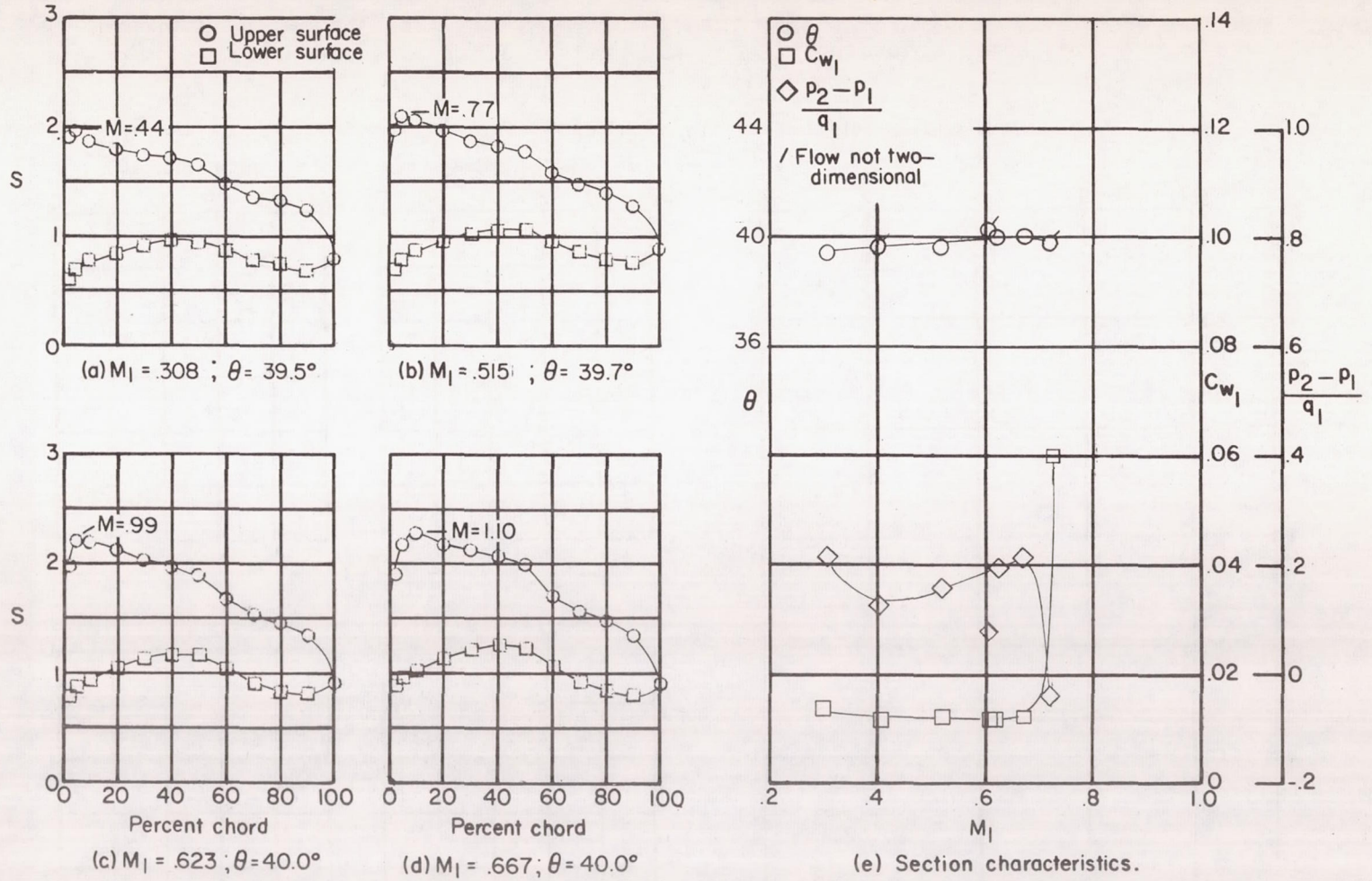


Figure 13.- Blade-surface pressure distributions and section characteristics for the cascade combination $\beta_1 = 25°$, $\sigma = 1.5$, $\alpha = 23.8°$, and NACA 65-($15A_{10}$)10 blade section.

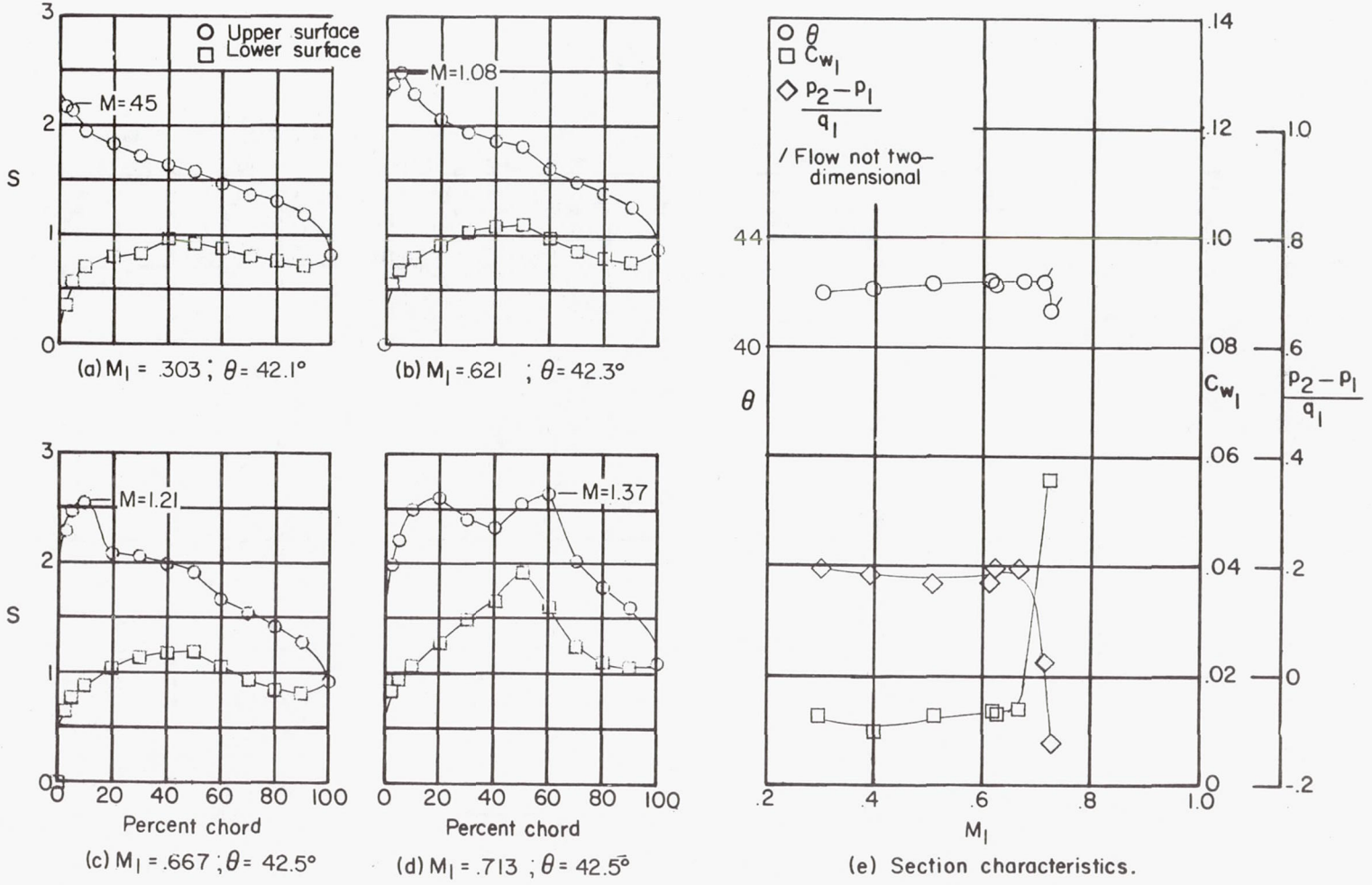


Figure 14.- Blade-surface pressure distributions and section characteristics for the cascade combination $\beta_1 = 25^\circ$, $\sigma = 1.5$, $\alpha = 26.8^\circ$, and NACA 65-($15A_{10}$)10 blade section.

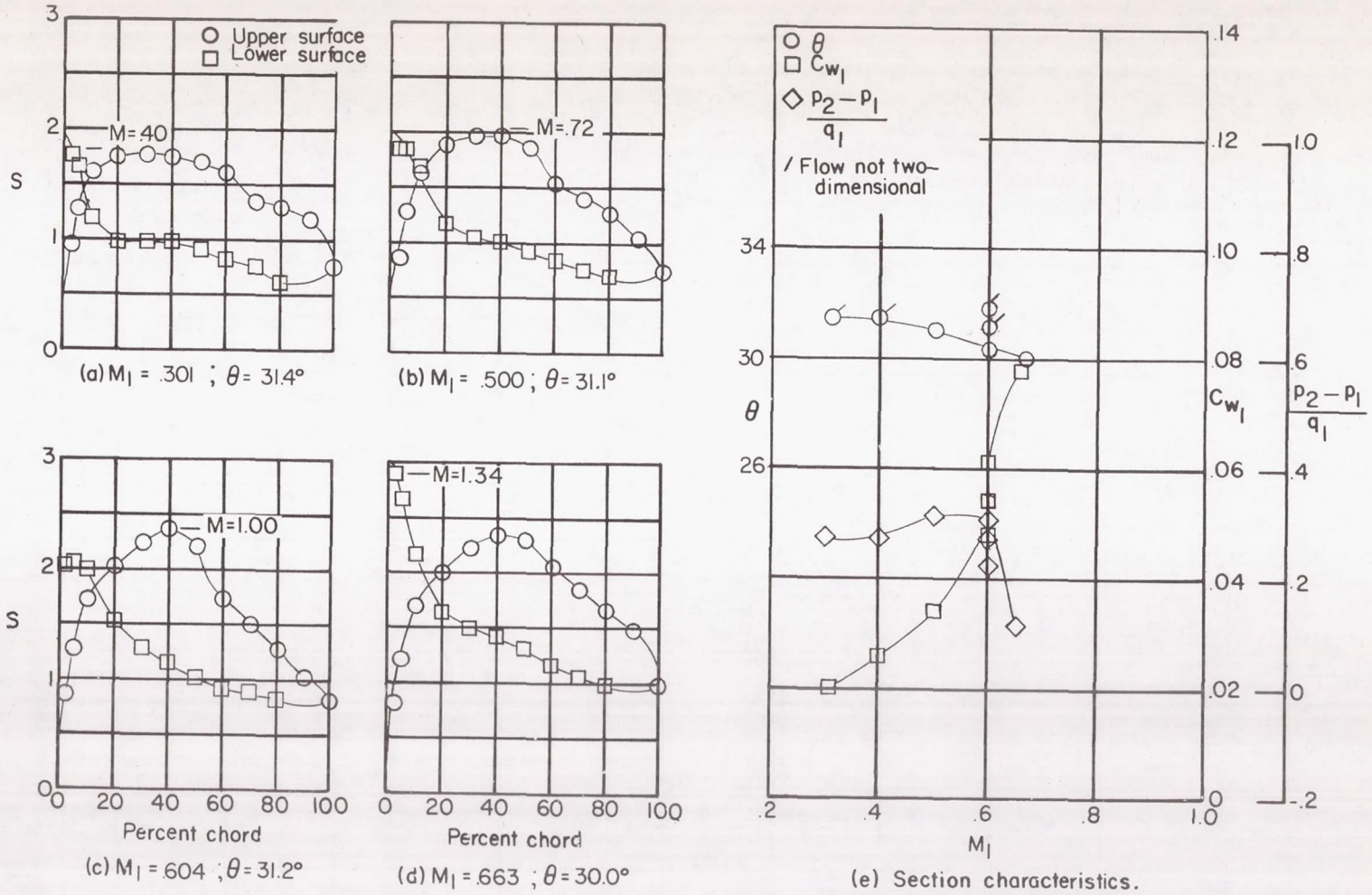


Figure 15.- Blade-surface pressure distributions and section characteristics for the cascade combination $\beta_1 = 35°$, $\sigma = 1.5$, $\alpha = 15.5°$, and NACA 65-($18A_{10}$)10 blade section.

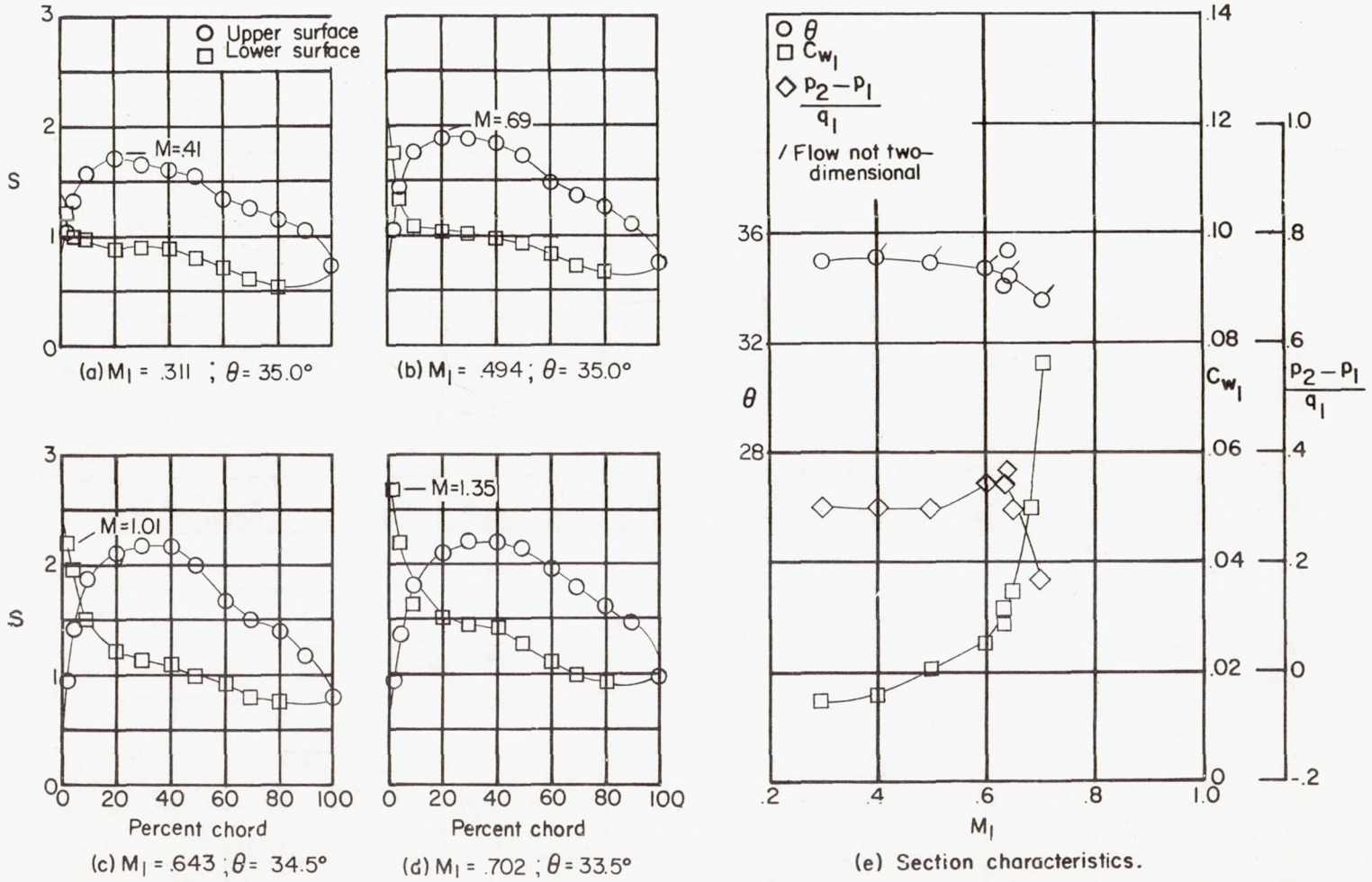


Figure 16.- Blade-surface pressure distributions and section characteristics for the cascade combination $\beta_1 = 35^\circ$, $\sigma = 1.5$, $\alpha = 18.5^\circ$, and NACA 65-($18A_{10}$)10 blade section.

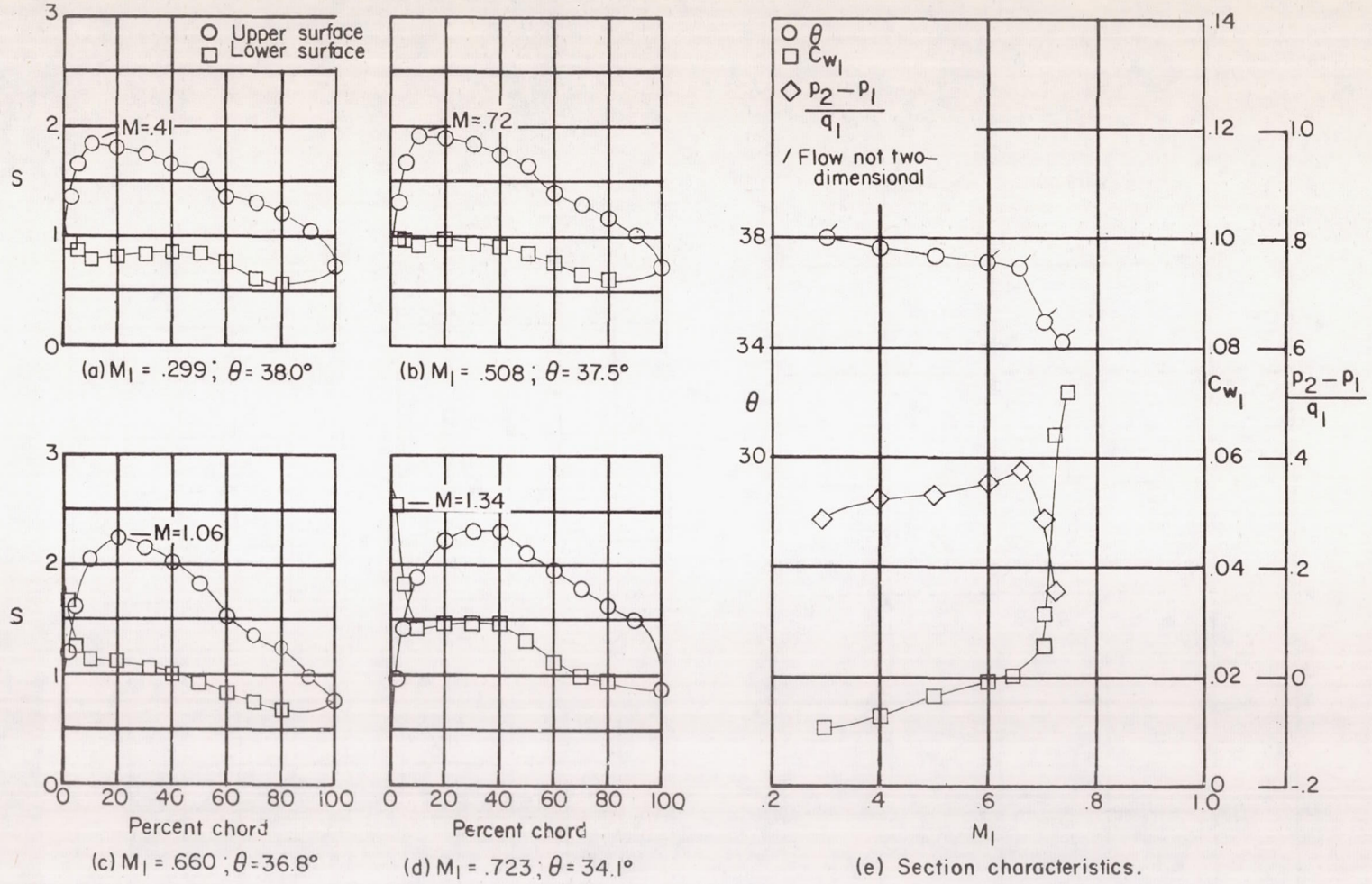


Figure 17.- Blade-surface pressure distributions and section characteristics for the cascade combination $\beta_1 = 35°$, $\sigma = 1.5$, $\alpha = 21.5°$, and NACA 65-($18A_{10}$)10 blade section.

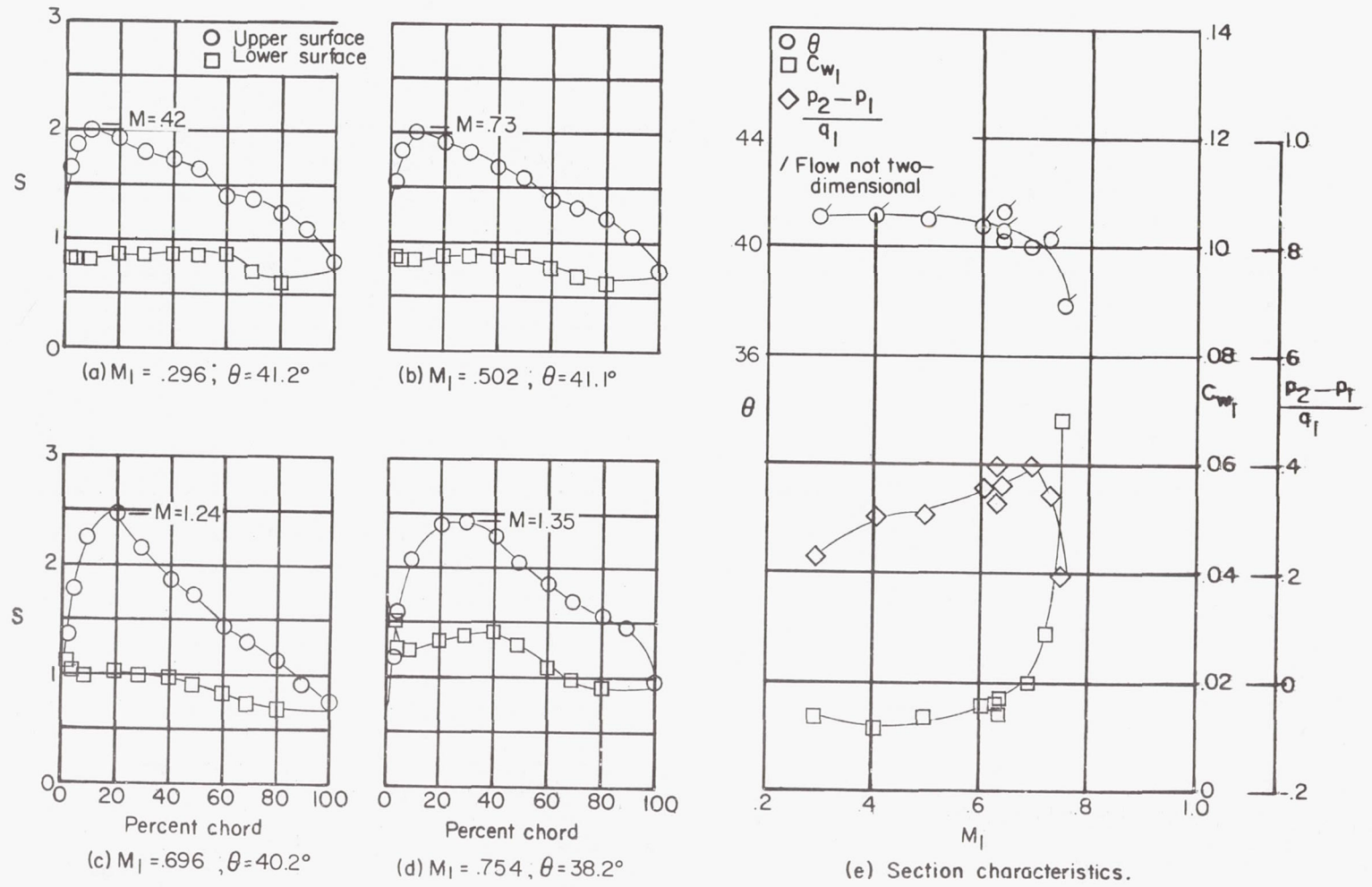


Figure 18.- Blade-surface pressure distributions and section characteristics for the cascade combination $\beta_1 = 35°$, $\sigma = 1.5$, $\alpha = 24.5°$, and NACA 65-($18A_{10}$)10 blade section.

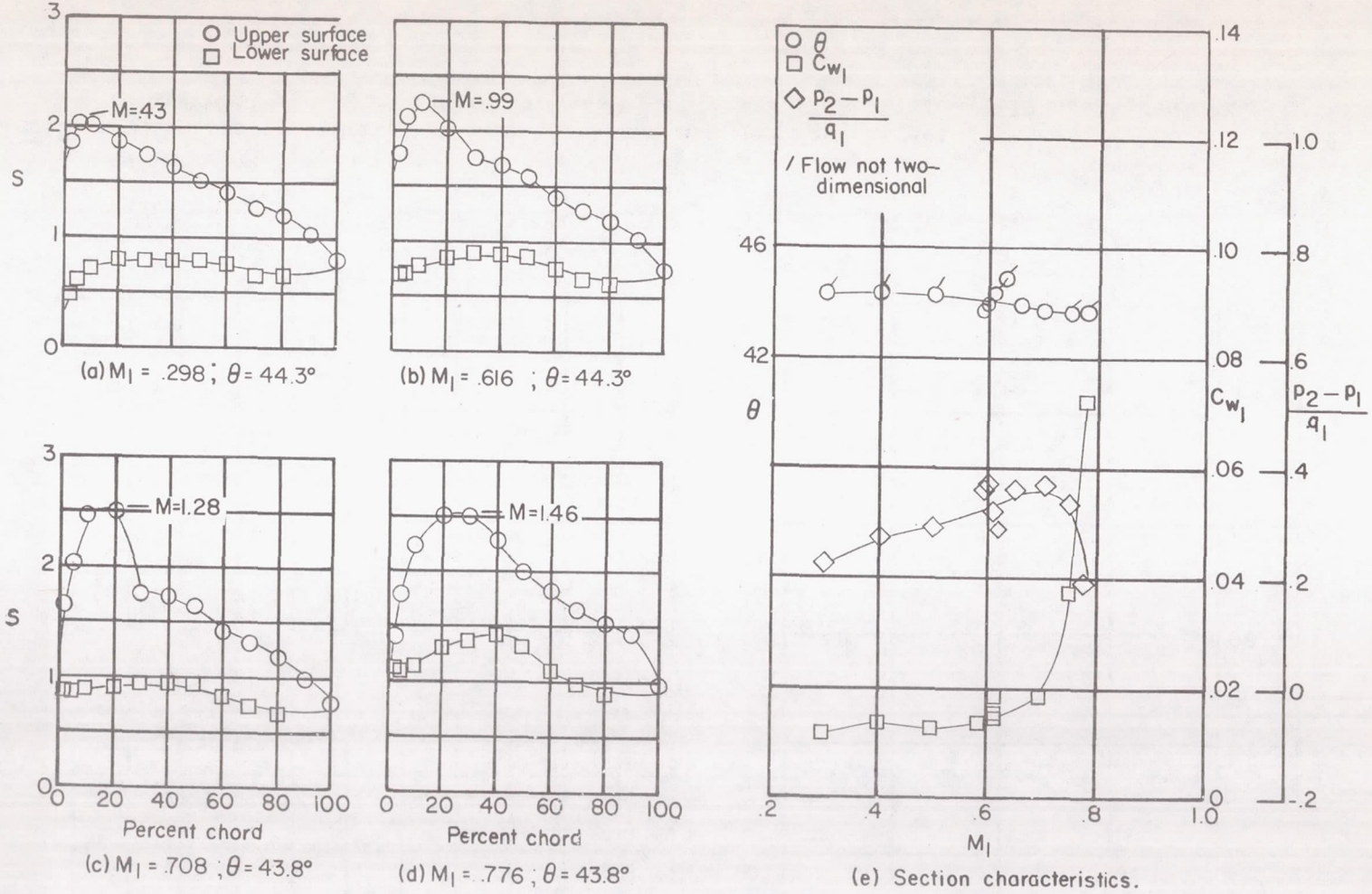


Figure 19.- Blade-surface pressure distributions and section characteristics for the cascade combination $\beta_1 = 35°$, $\sigma = 1.5$, $\alpha = 27.5°$, and NACA 65-($18A_{10}$)10 blade section.

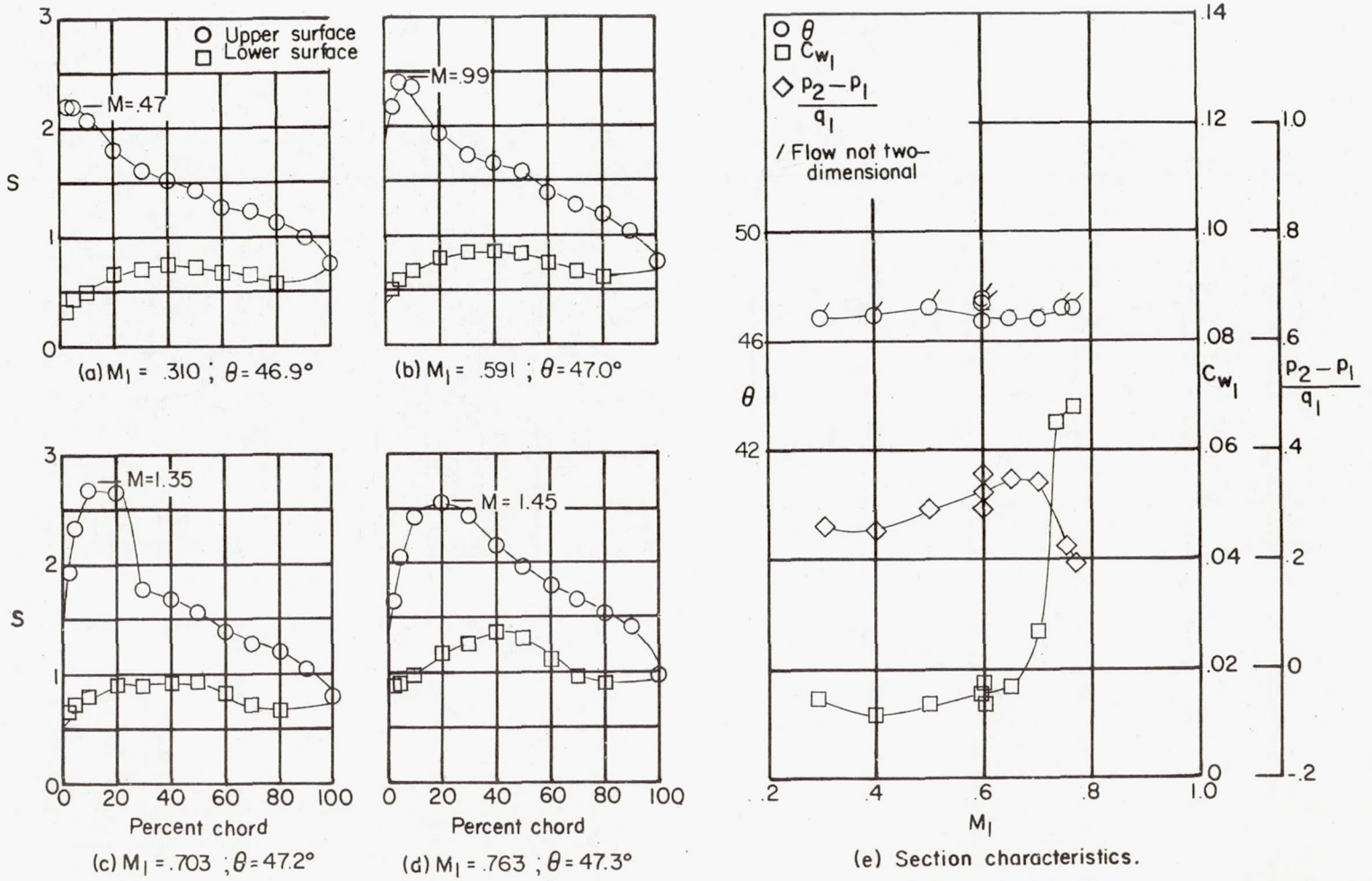


Figure 20.- Blade-surface pressure distributions and section characteristics for the cascade combination $\beta_1 = 35^\circ$, $\sigma = 1.5$, $\alpha = 30.5^\circ$, and NACA 65-($18A_{10}$)10 blade section.

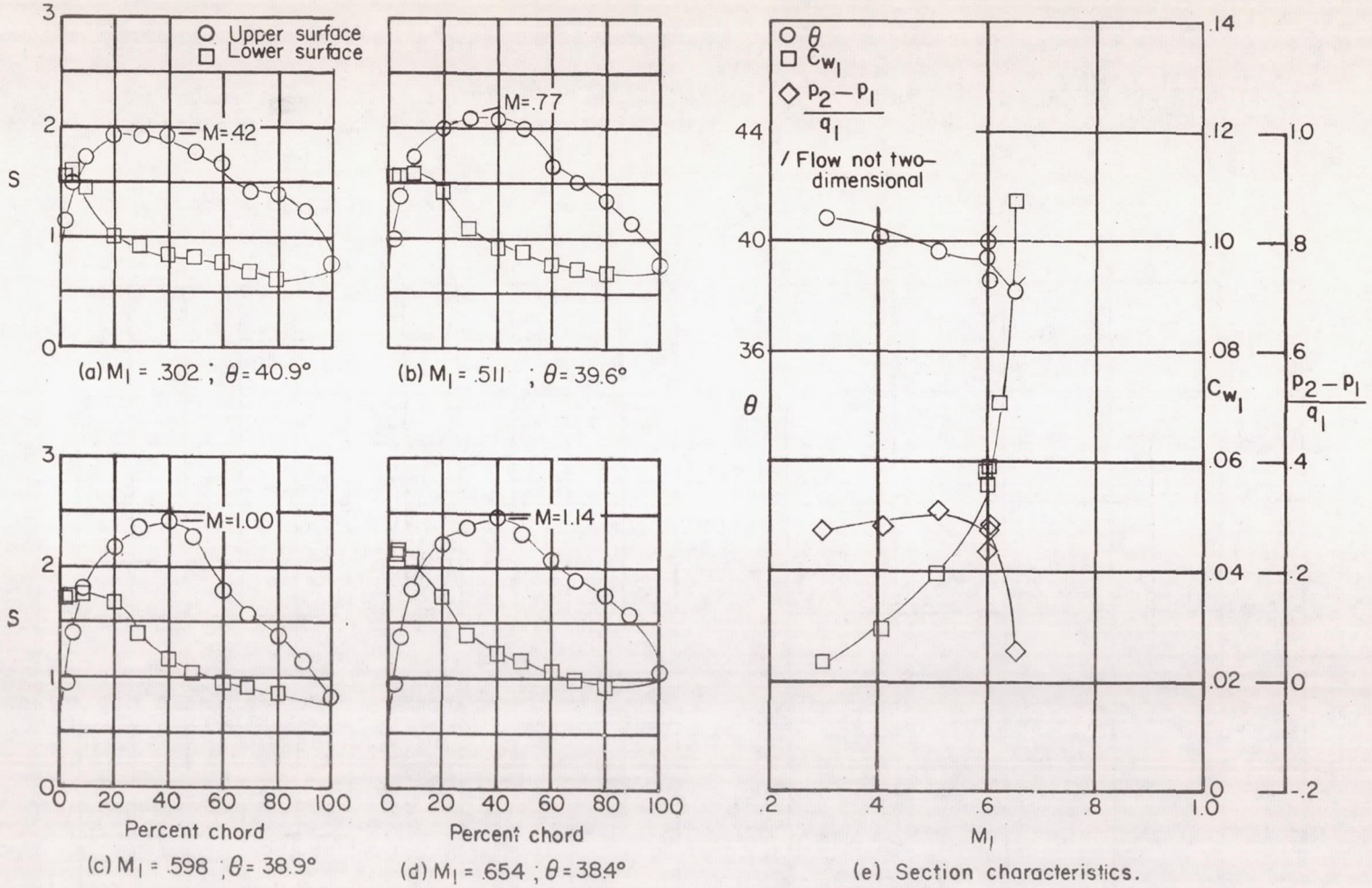


Figure 21.- Blade-surface pressure distributions and section characteristics for the cascade combination $\beta_1 = 35^\circ$, $\sigma = 1.5$, $\alpha = 20.5^\circ$, and NACA 65-($21A_{10}$)10 blade section.

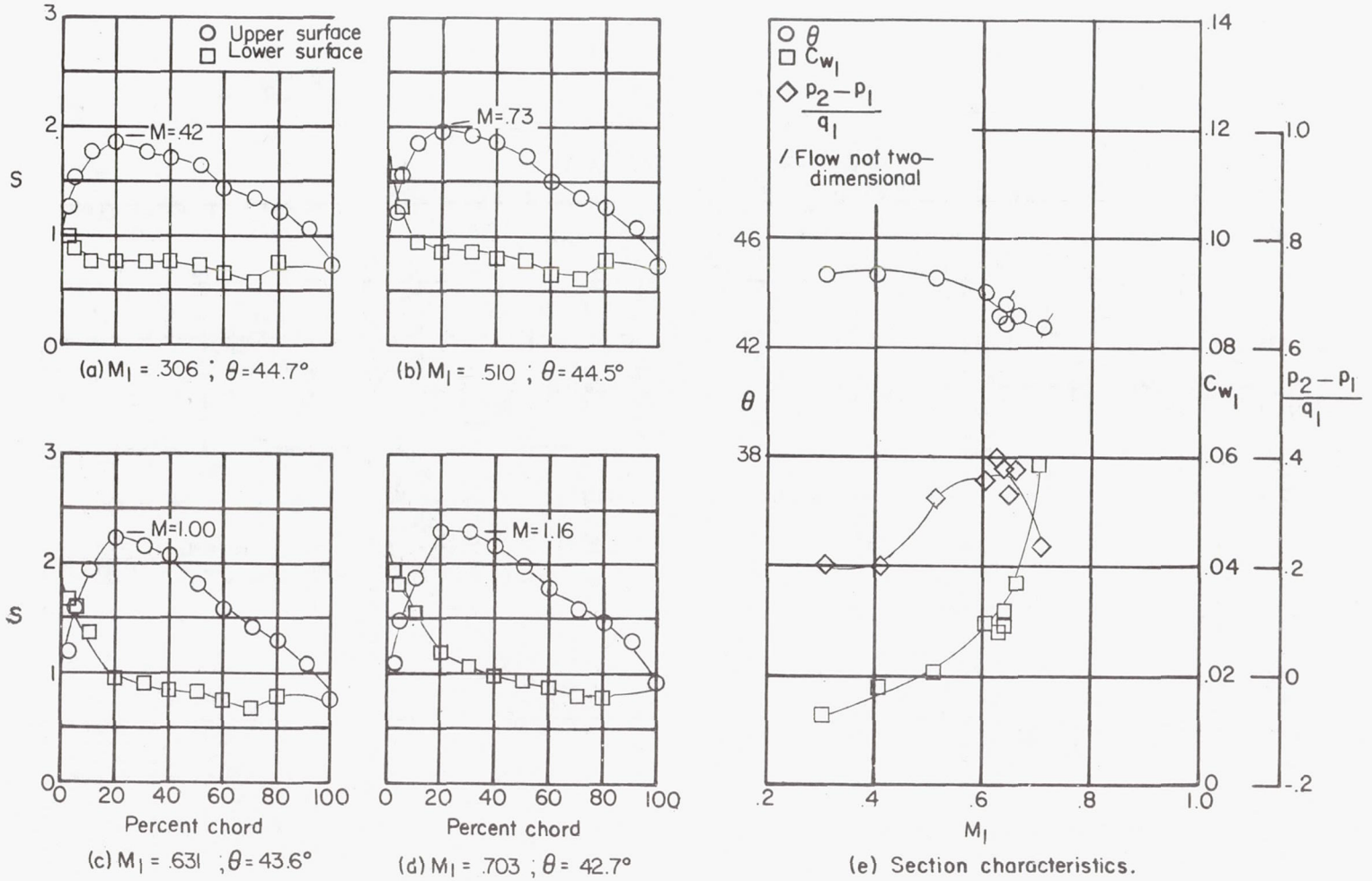


Figure 22.- Blade-surface pressure distributions and section characteristics for the cascade combination $\beta_1 = 35°$, $\sigma = 1.5$, $\alpha = 23.5°$, and NACA 65-$(21A_{10})$10 blade section.

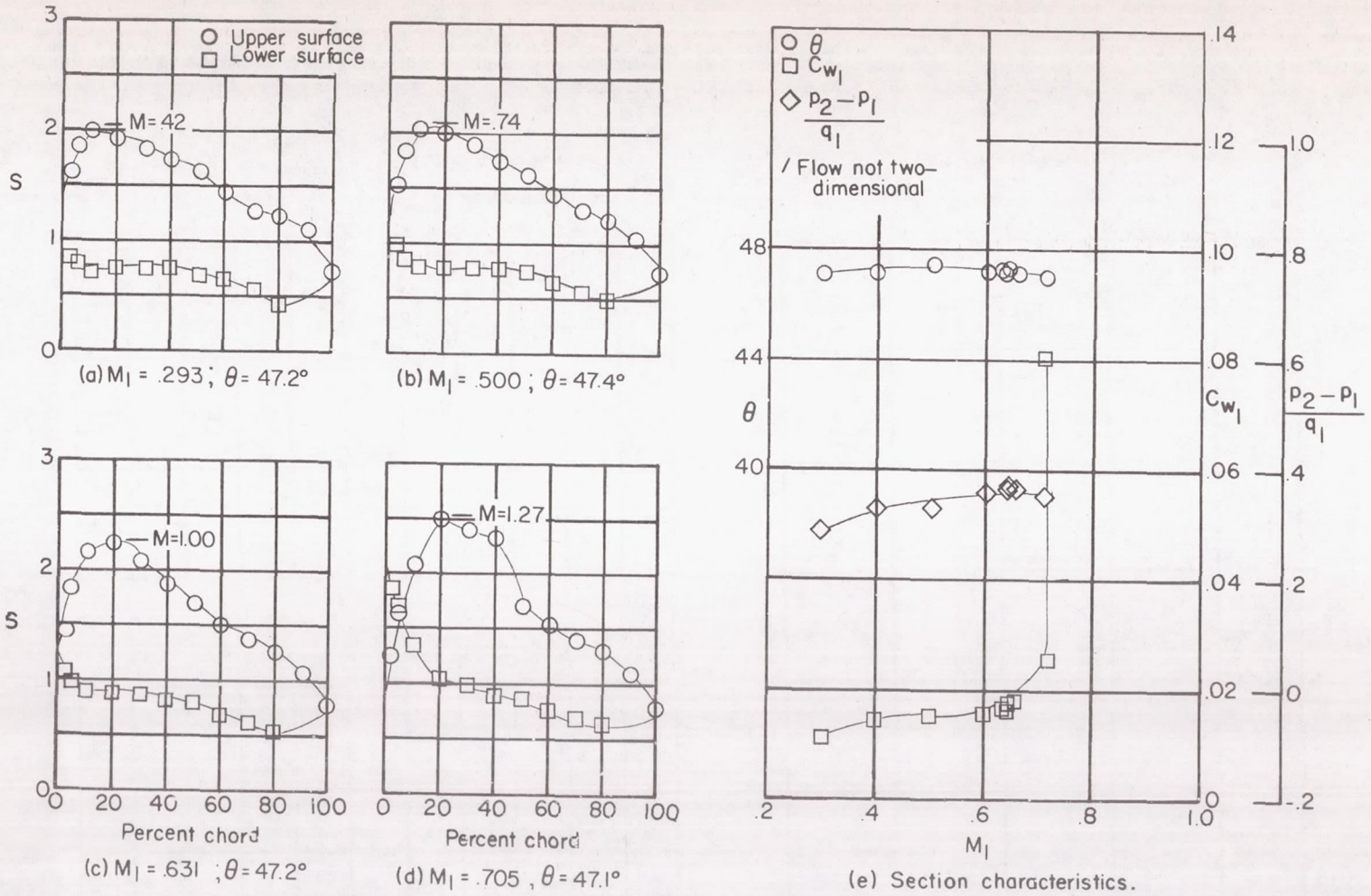


Figure 23.- Blade-surface pressure distributions and section characteristics for the cascade combination $\beta_1 = 35°$, $\sigma = 1.5$, $\alpha = 26.5°$, and NACA 65-$(21A_{10})$10 blade section.

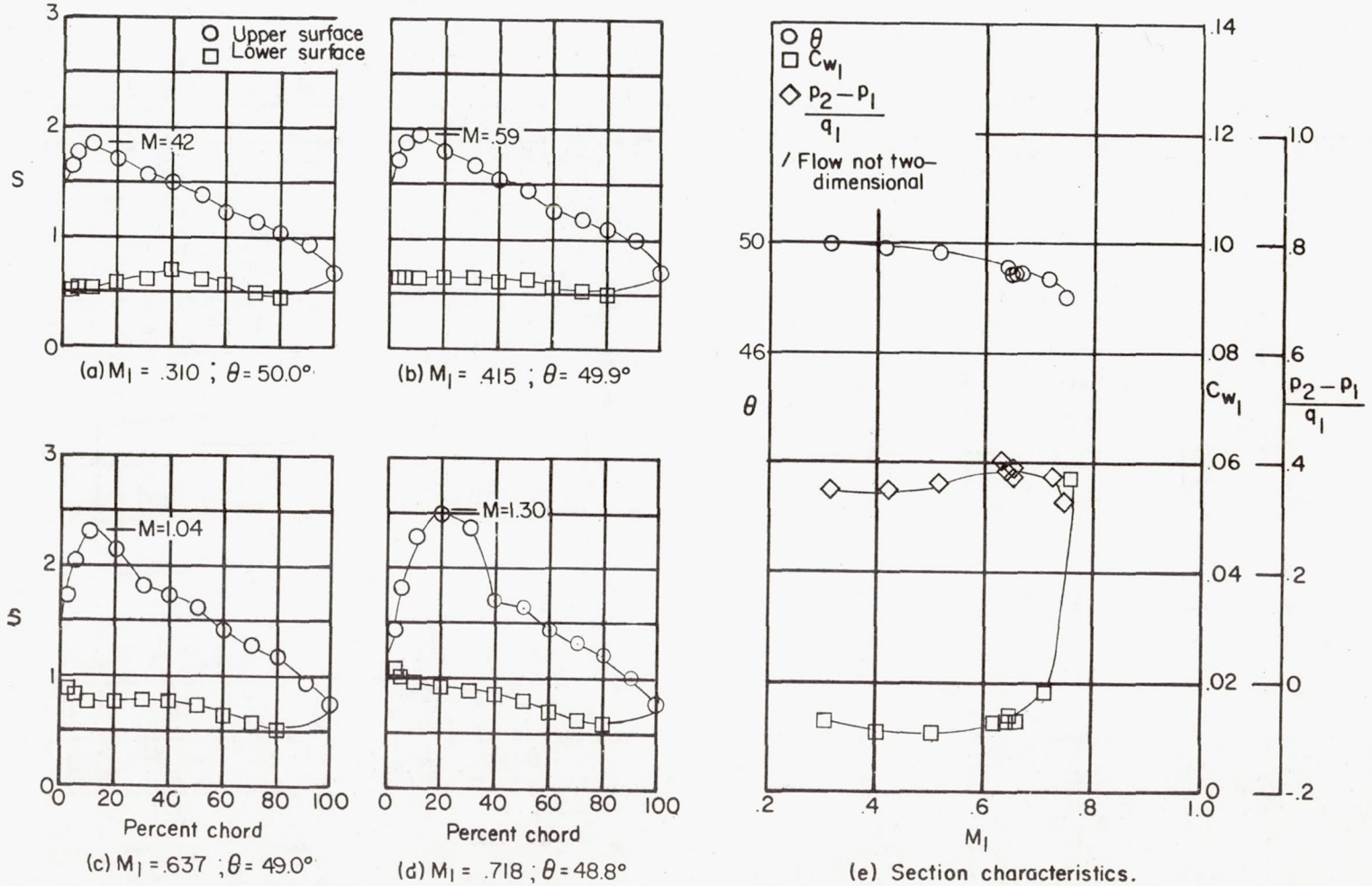


Figure 24.- Blade-surface pressure distributions and section characteristics for the cascade combination $\beta_1 = 35°$, $\sigma = 1.5$, $\alpha = 29.5°$, and NACA 65-($21A_{10}$)10 blade section.

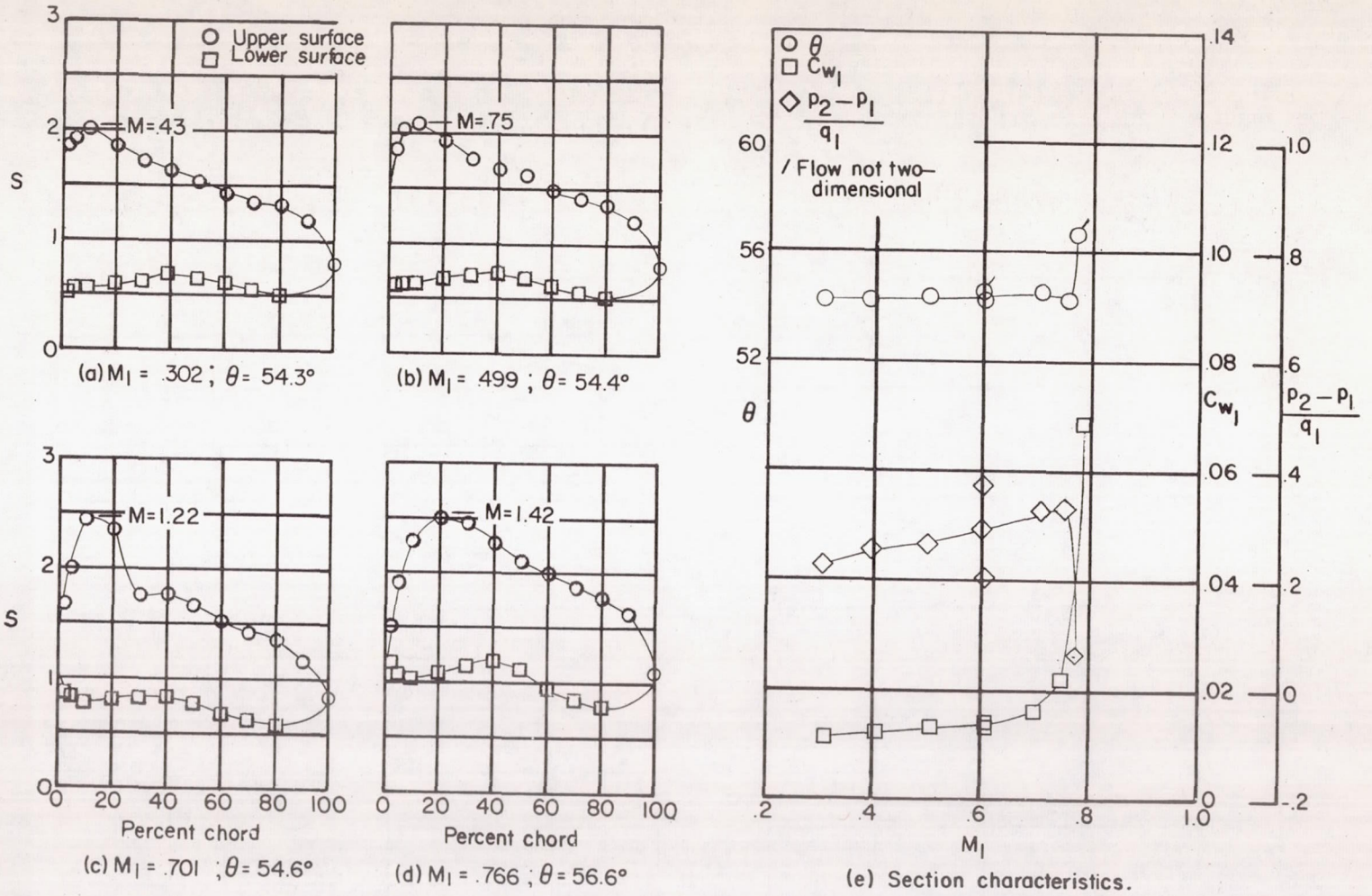


Figure 25.- Blade-surface pressure distributions and section characteristics for the cascade combination $\beta_1 = 35^\circ$, $\sigma = 1.5$, $\alpha = 32.4^\circ$, and NACA 65-($21A_{10}$)10 blade section.

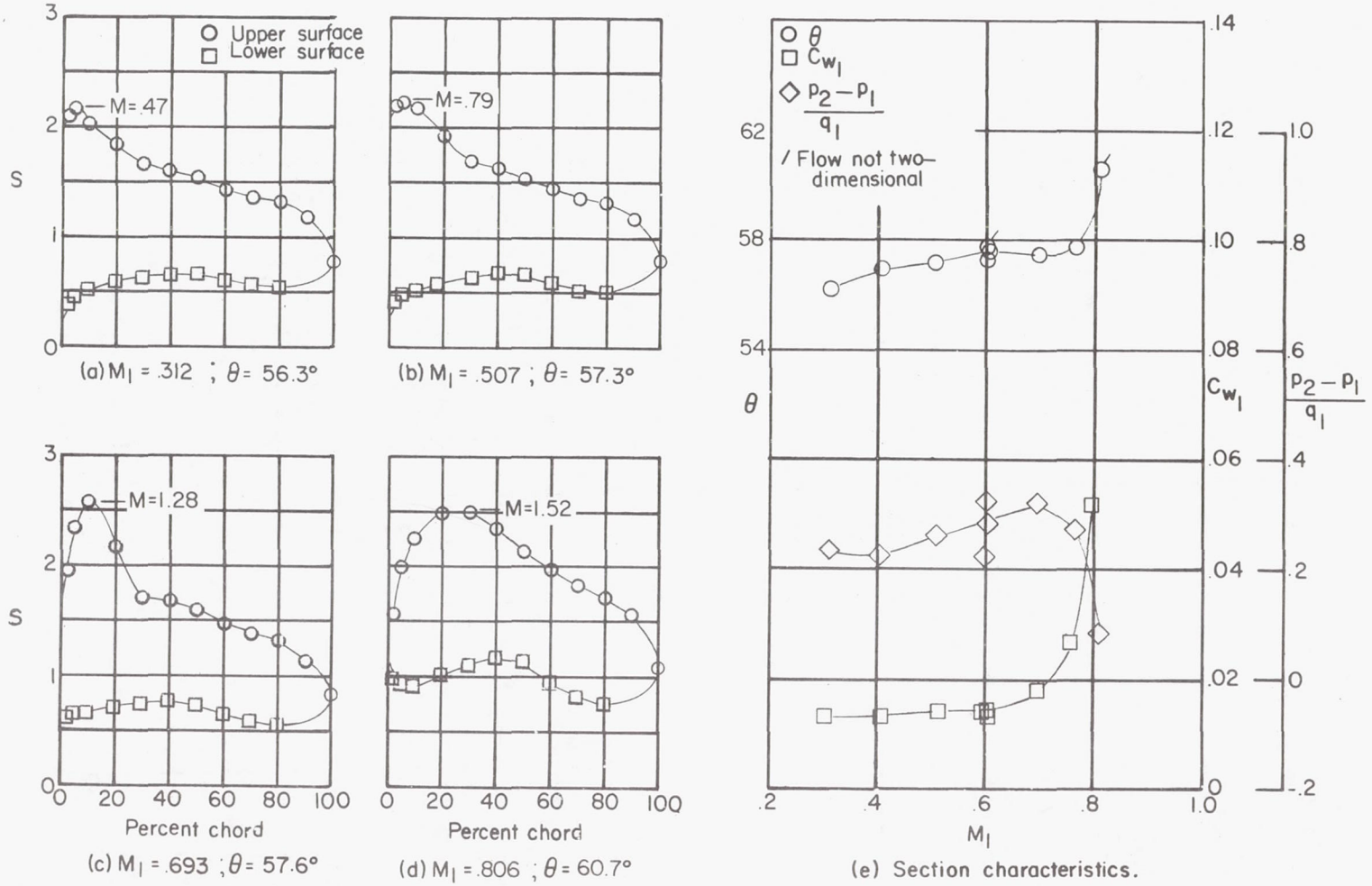


Figure 26.- Blade-surface pressure distributions and section characteristics for the cascade combination $\beta_1 = 35^\circ$, $\sigma = 1.5$, $\alpha = 35.4^\circ$, and NACA 65-(21A10)10 blade section.

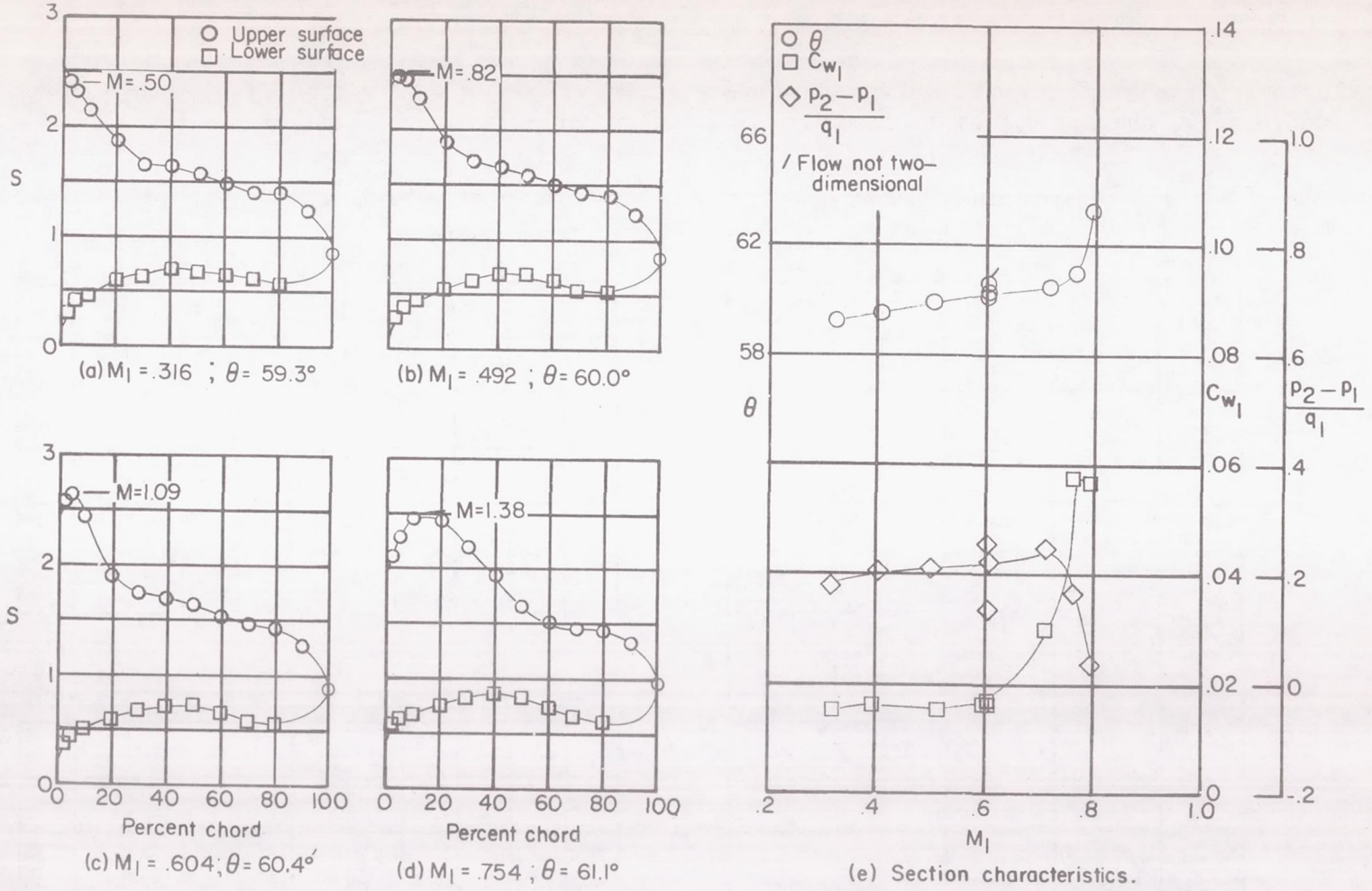


Figure 27.- Blade-surface pressure distributions and section characteristics for the cascade combination $\beta_1 = 35^\circ$, $\sigma = 1.5$, $\alpha = 38.4^\circ$, and NACA 65-$(21A_{10})$10 blade section.

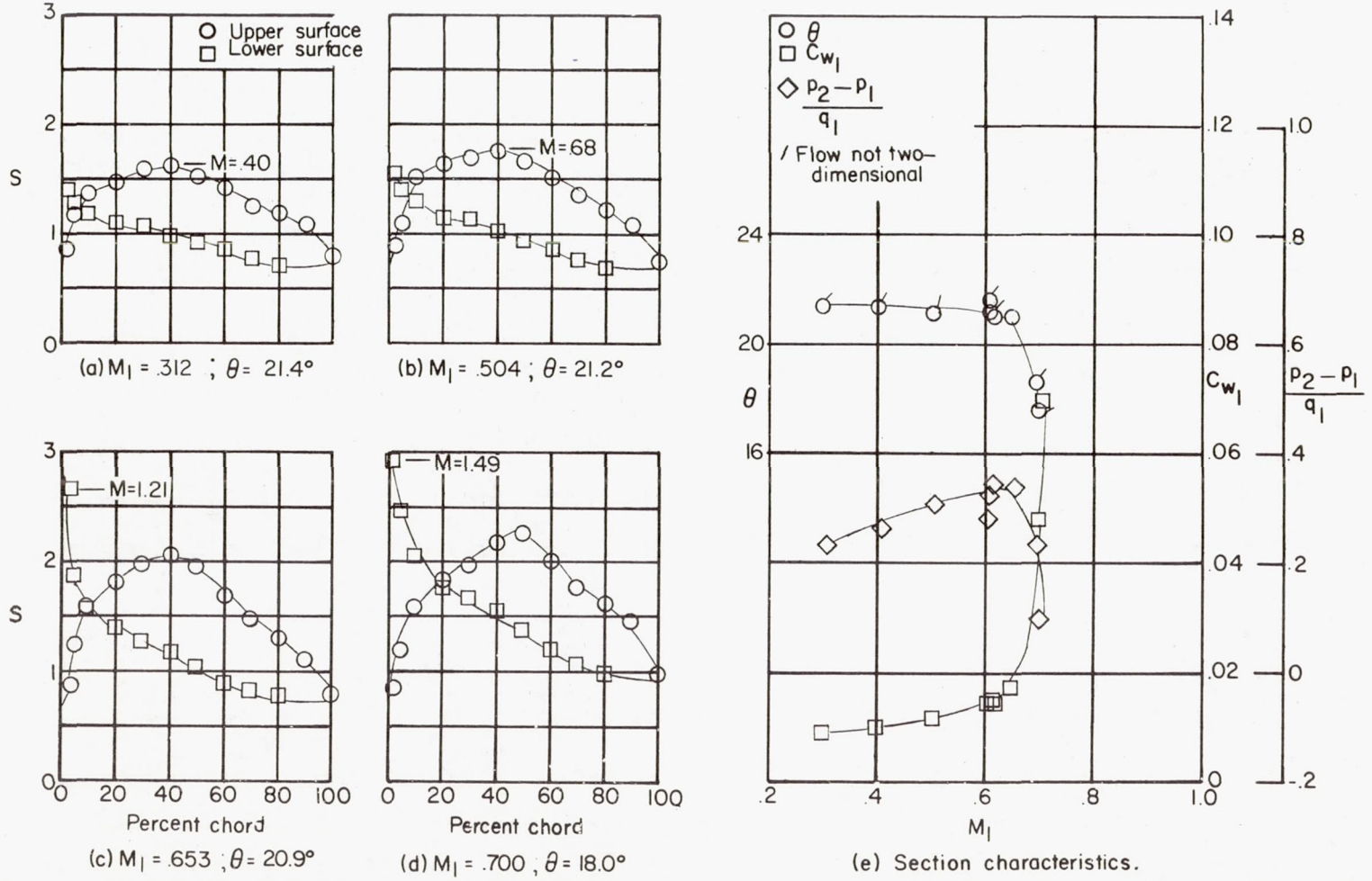


Figure 28.- Blade-surface pressure distributions and section characteristics for the cascade combination $\beta_1 = 35°$, $\sigma = 1.25$, $\alpha = 11.1°$, and NACA 65-$(12A_{10})$10 blade section.

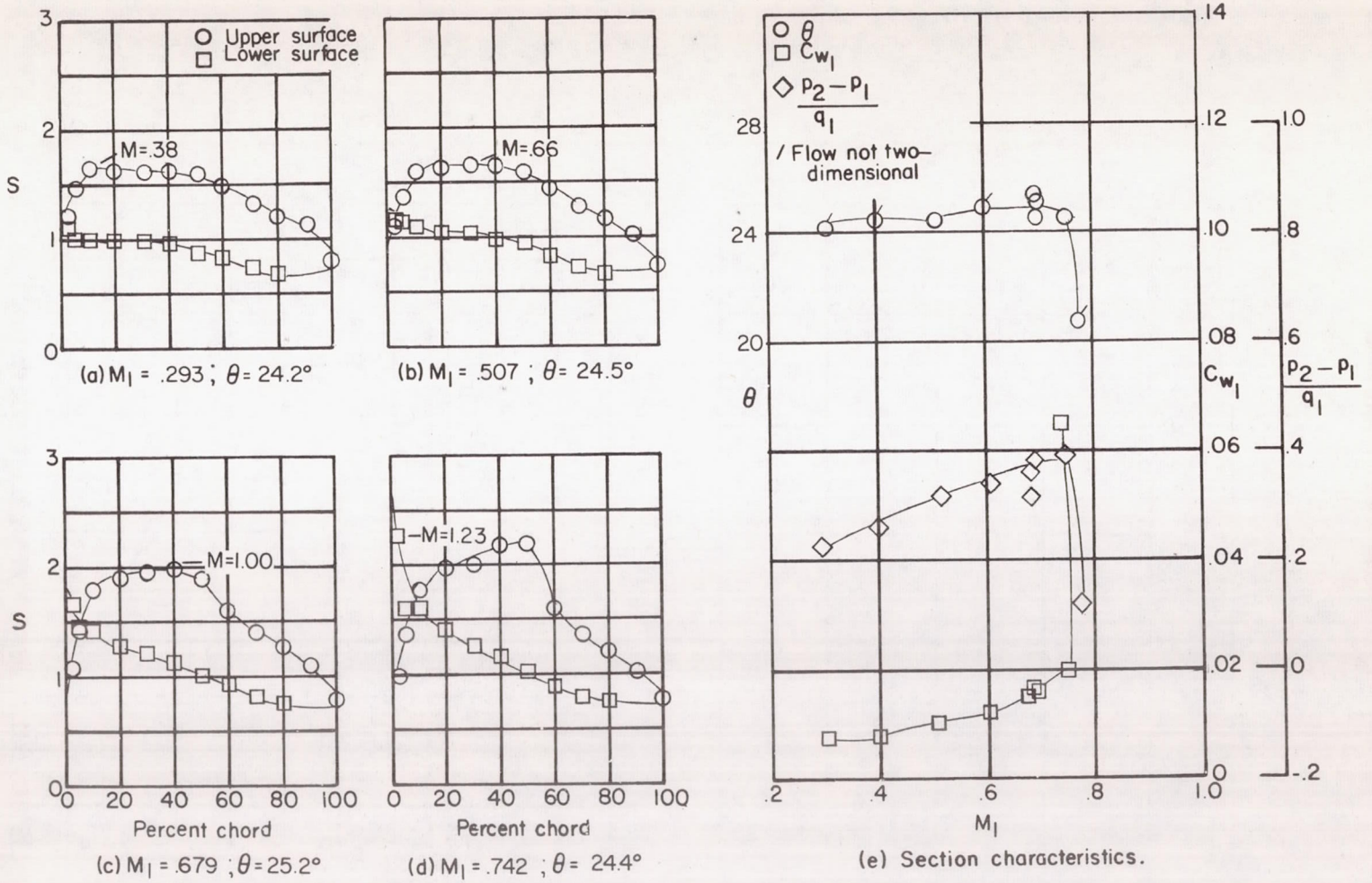


Figure 29.- Blade-surface pressure distributions and section characteristics for the cascade combination $\beta_1 = 35^\circ$, $\sigma = 1.25$, $\alpha = 14.1^\circ$, and NACA 65-(12A10)10 blade section.

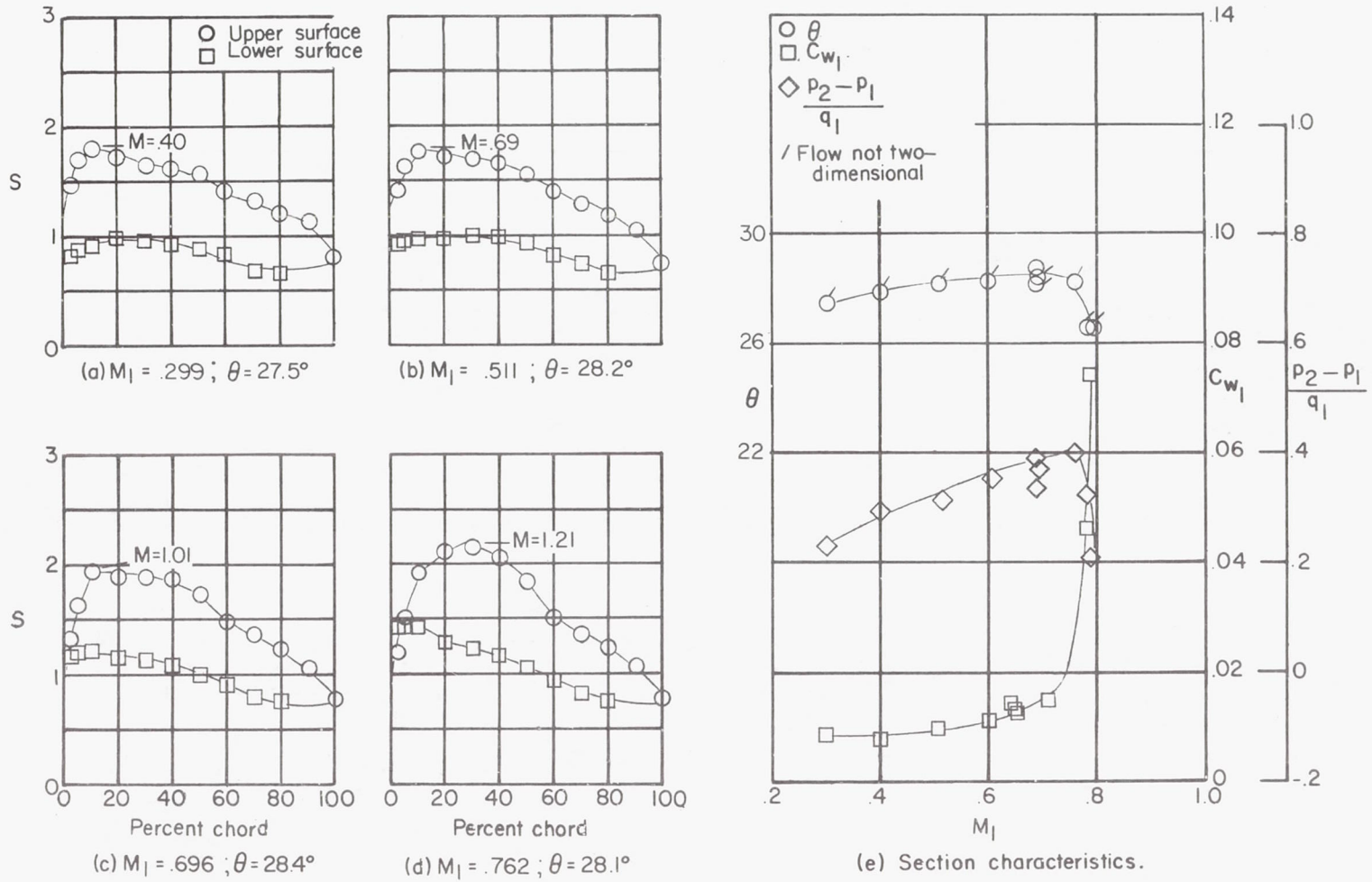


Figure 30.- Blade-surface pressure distributions and section characteristics for the cascade combination $\beta_1 = 35^\circ$, $\sigma = 1.25$, $\alpha = 17.1^\circ$, and NACA 65-(12A10)10 blade section.

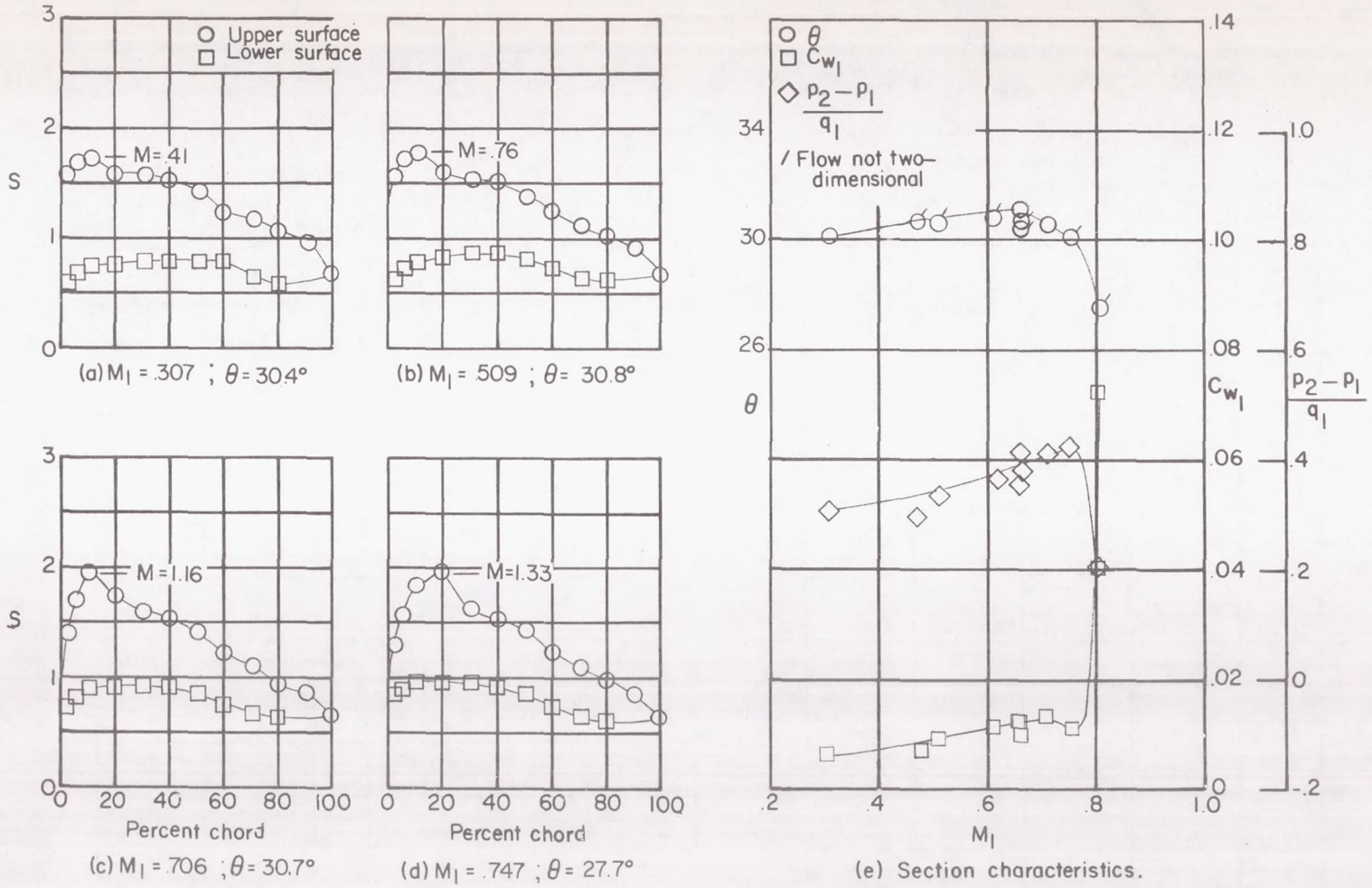


Figure 31.- Blade-surface pressure distributions and section characteristics for the cascade combination $\beta_1 = 35^\circ$, $\sigma = 1.25$, $\alpha = 20.1^\circ$, and NACA 65-(12A10)10 blade section.

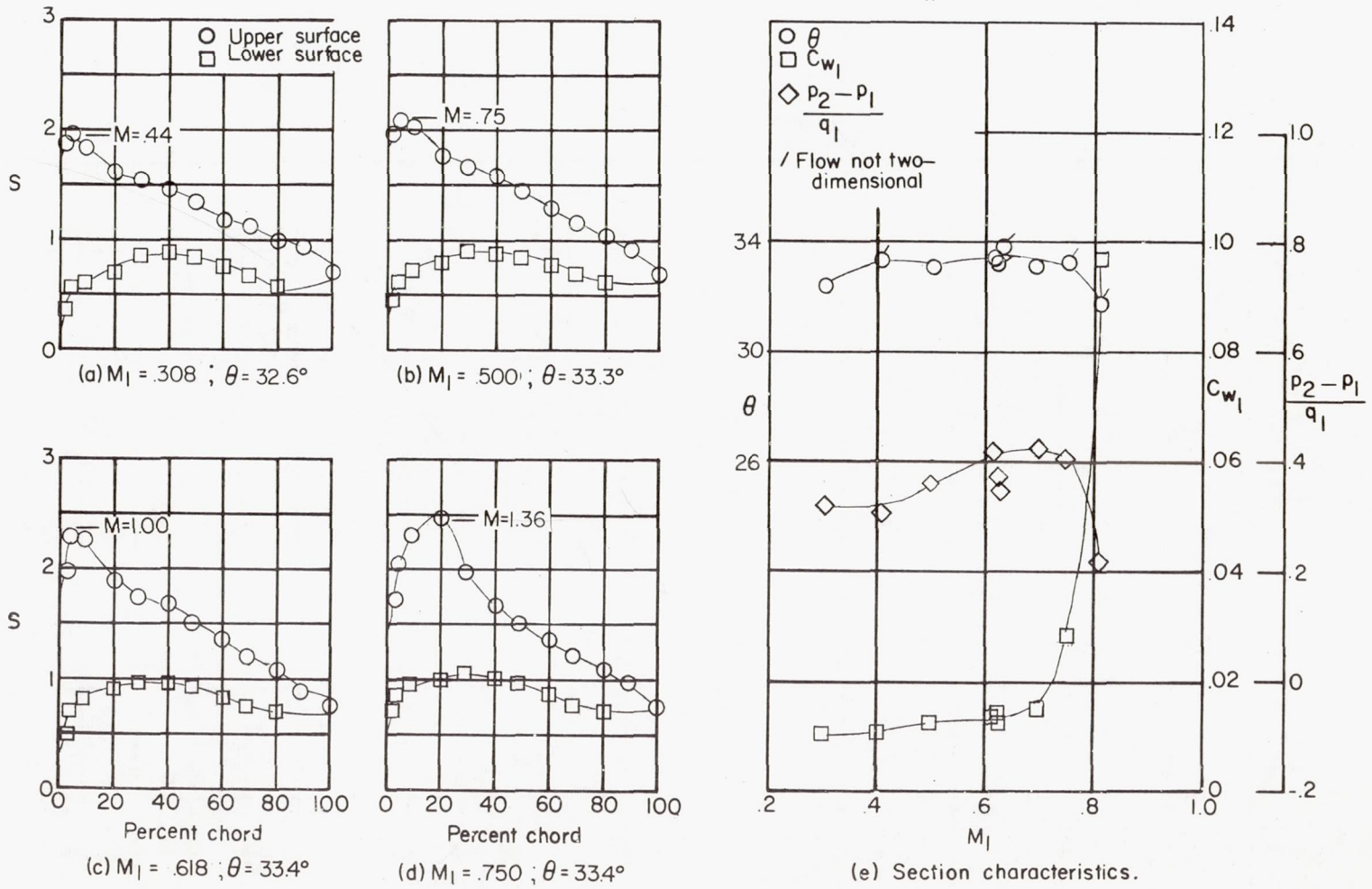


Figure 32.- Blade-surface pressure distributions and section characteristics for the cascade combination $\beta_1 = 35^\circ$, $\sigma = 1.25$, $\alpha = 23.1^\circ$, and NACA 65-($12A_{10}$)10 blade section.

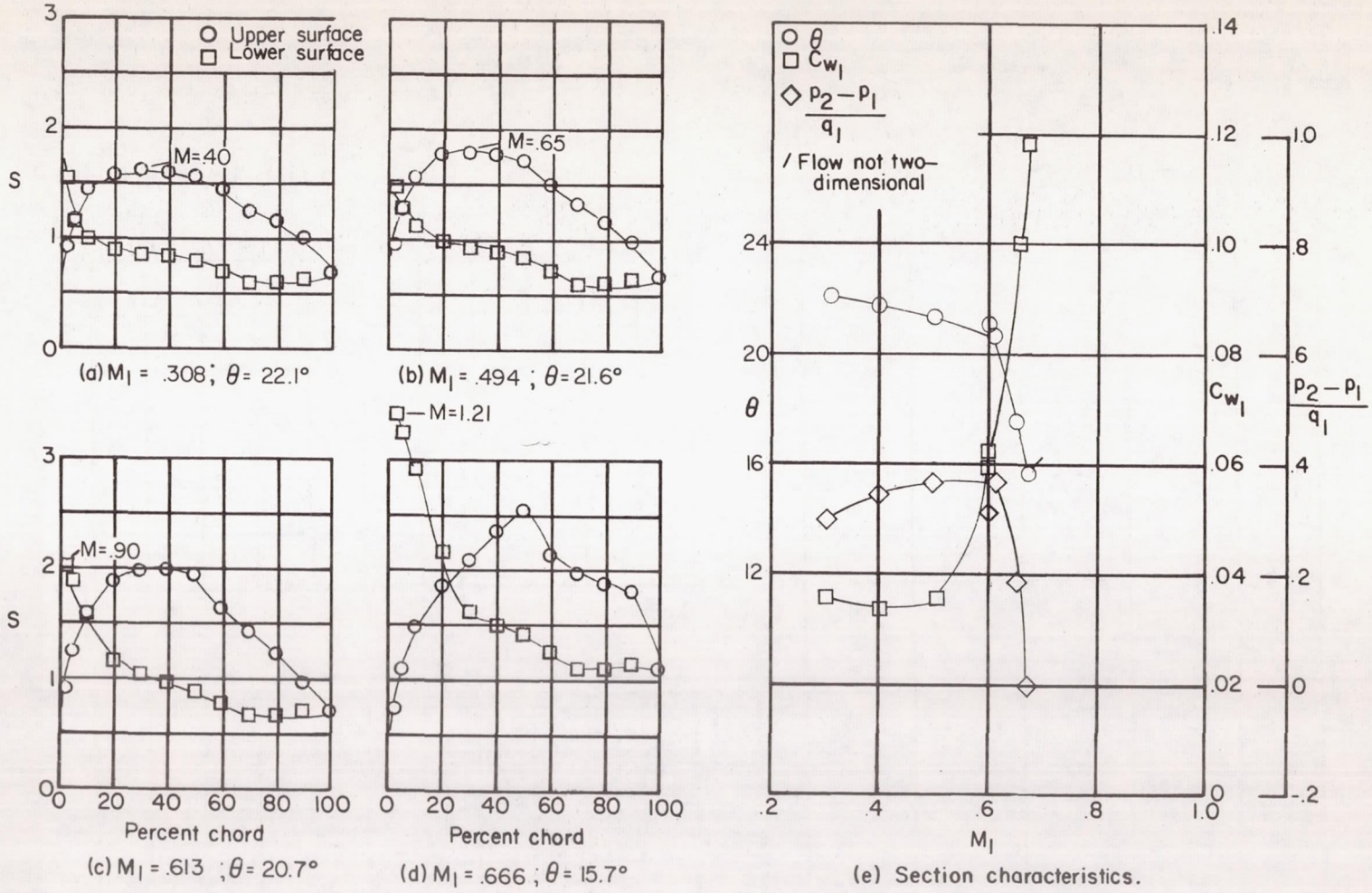


Figure 33.- Blade-surface pressure distributions and section characteristics for the cascade combination $\beta_1 = 35^\circ$, $\sigma = 1.25$, $\alpha = 10.3^\circ$, and NACA 65-($15A_{10}$)10 blade section.

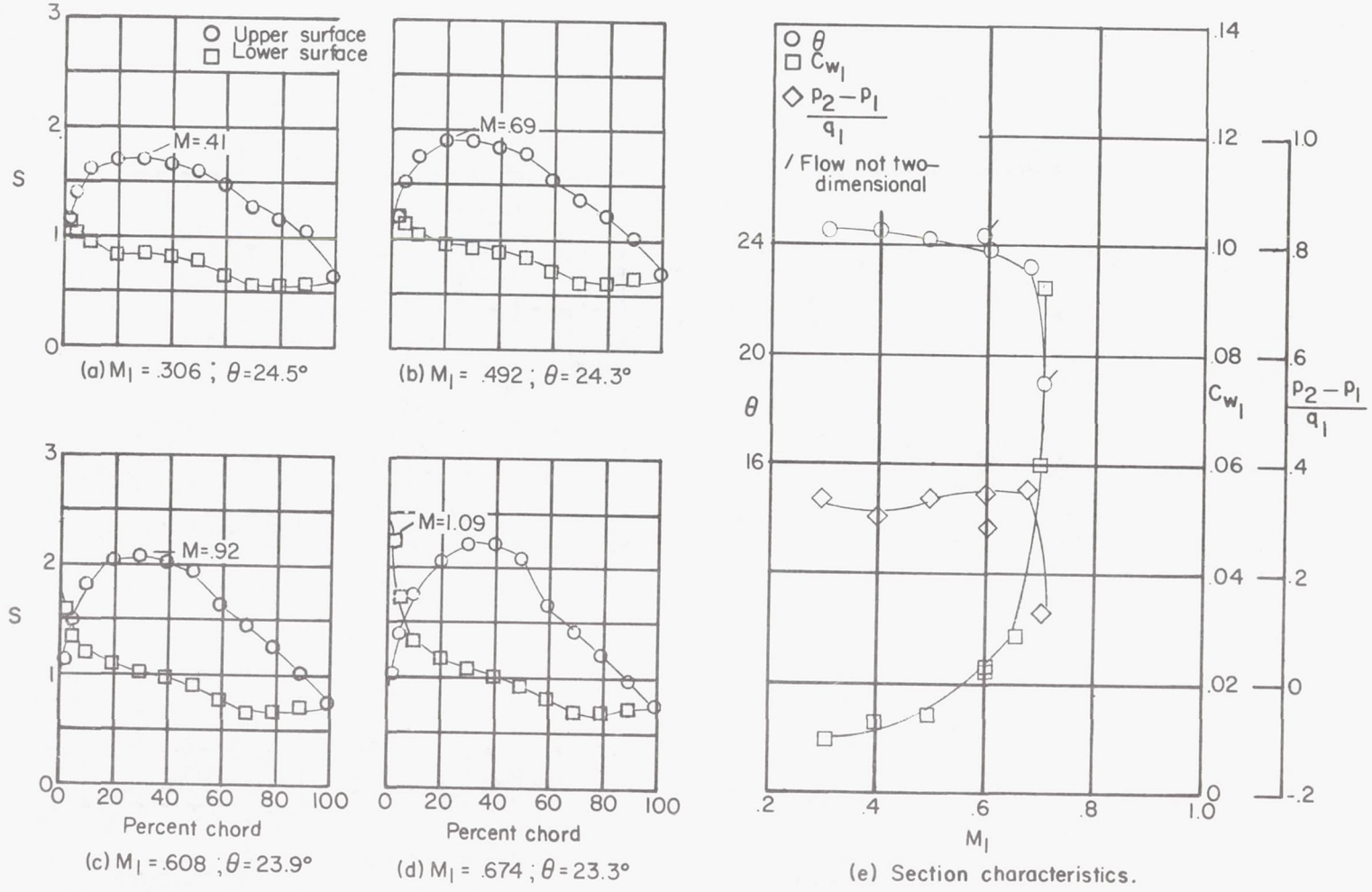


Figure 34.- Blade-surface pressure distributions and section characteristics for the cascade combination $\beta_1 = 35^\circ$, $\sigma = 1.25$, $\alpha = 13.3^\circ$, and NACA 65-($15A_{10}$)10 blade section.

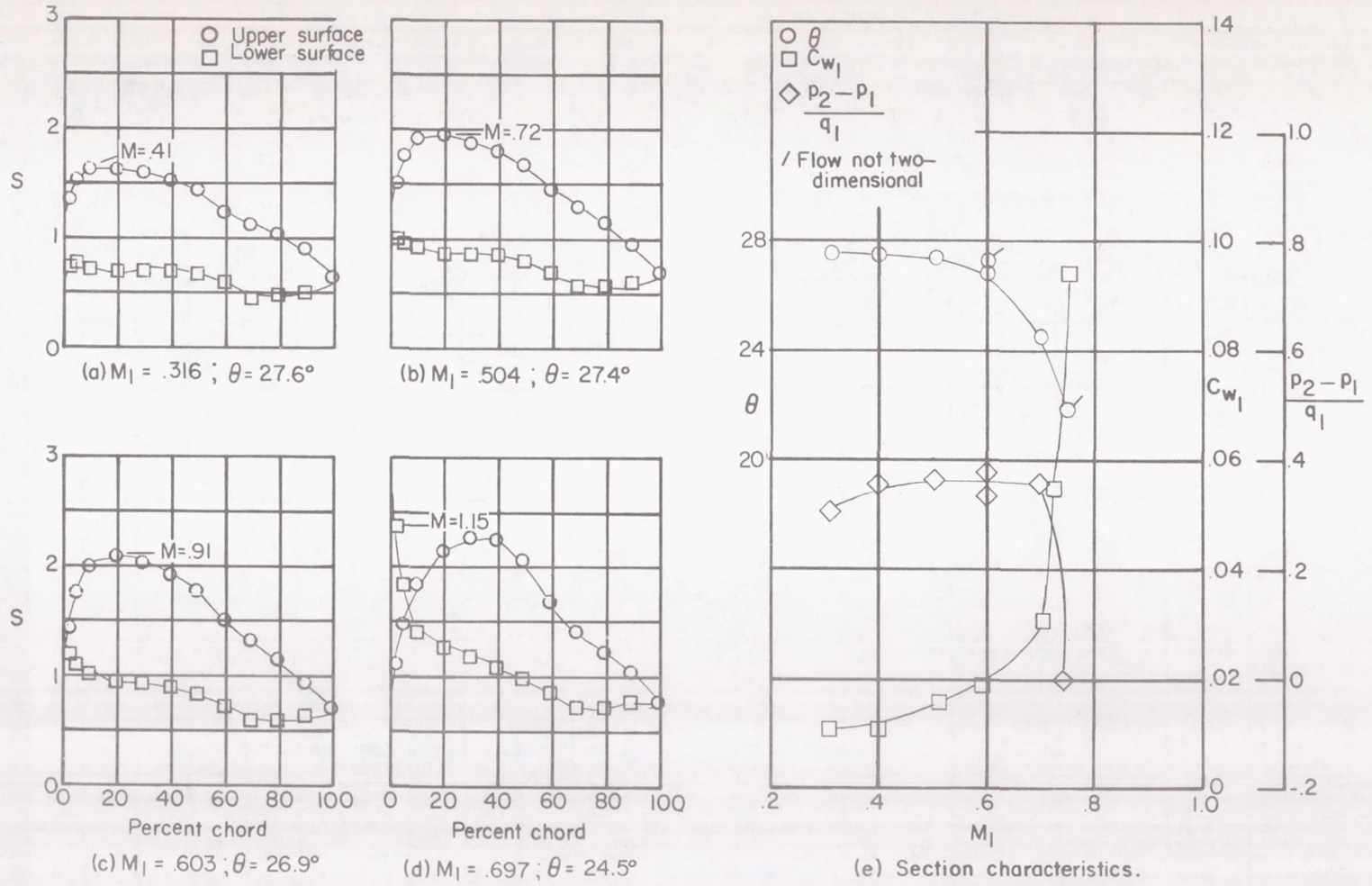


Figure 35.- Blade-surface pressure distributions and section characteristics for the cascade combination $\beta_1 = 35°$, $\sigma = 1.25$, $\alpha = 16.3°$, and NACA 65-$(15A_{10})$10 blade section.

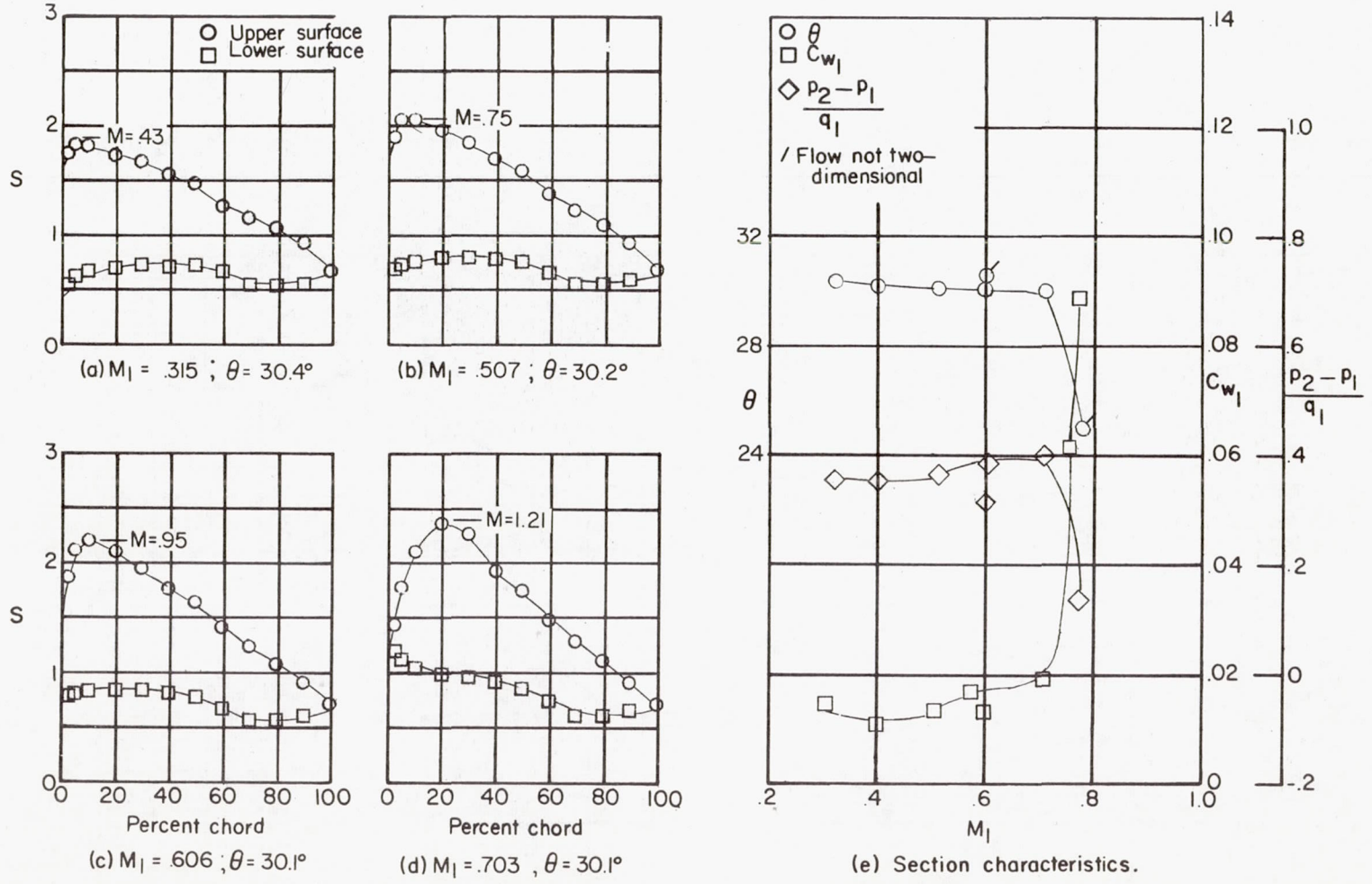


Figure 36.- Blade-surface pressure distributions and section characteristics for the cascade combination $\beta_1 = 35^\circ$, $\sigma = 1.25$, $\alpha = 19.3^\circ$, and NACA 65-($15A_{10}$)10 blade section.

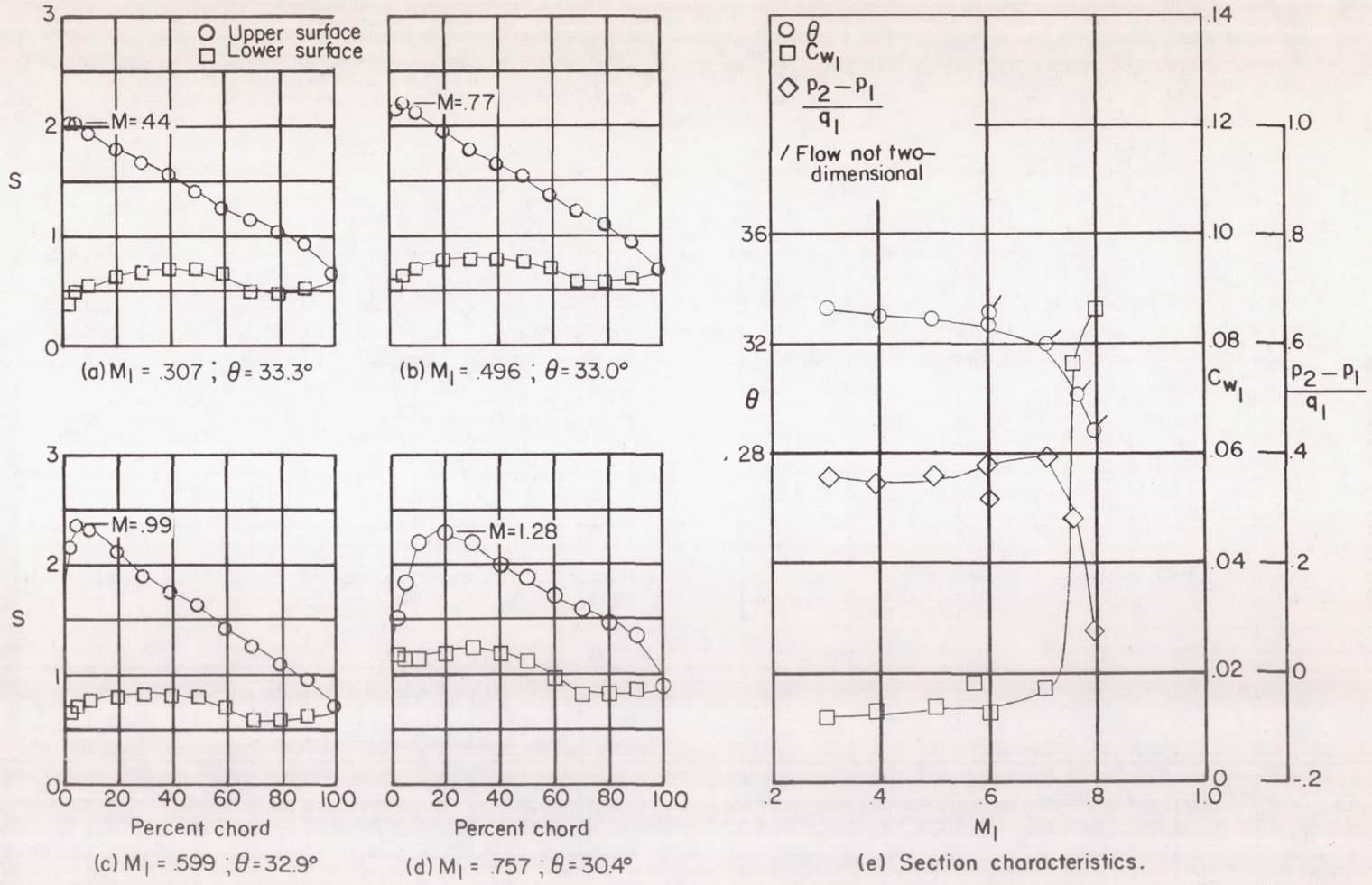


Figure 37.- Blade-surface pressure distributions and section characteristics for the cascade combination $\beta_1 = 35°$, $\sigma = 1.25$, $\alpha = 22.3°$, and NACA 65-($15A_{10}$)10 blade section.

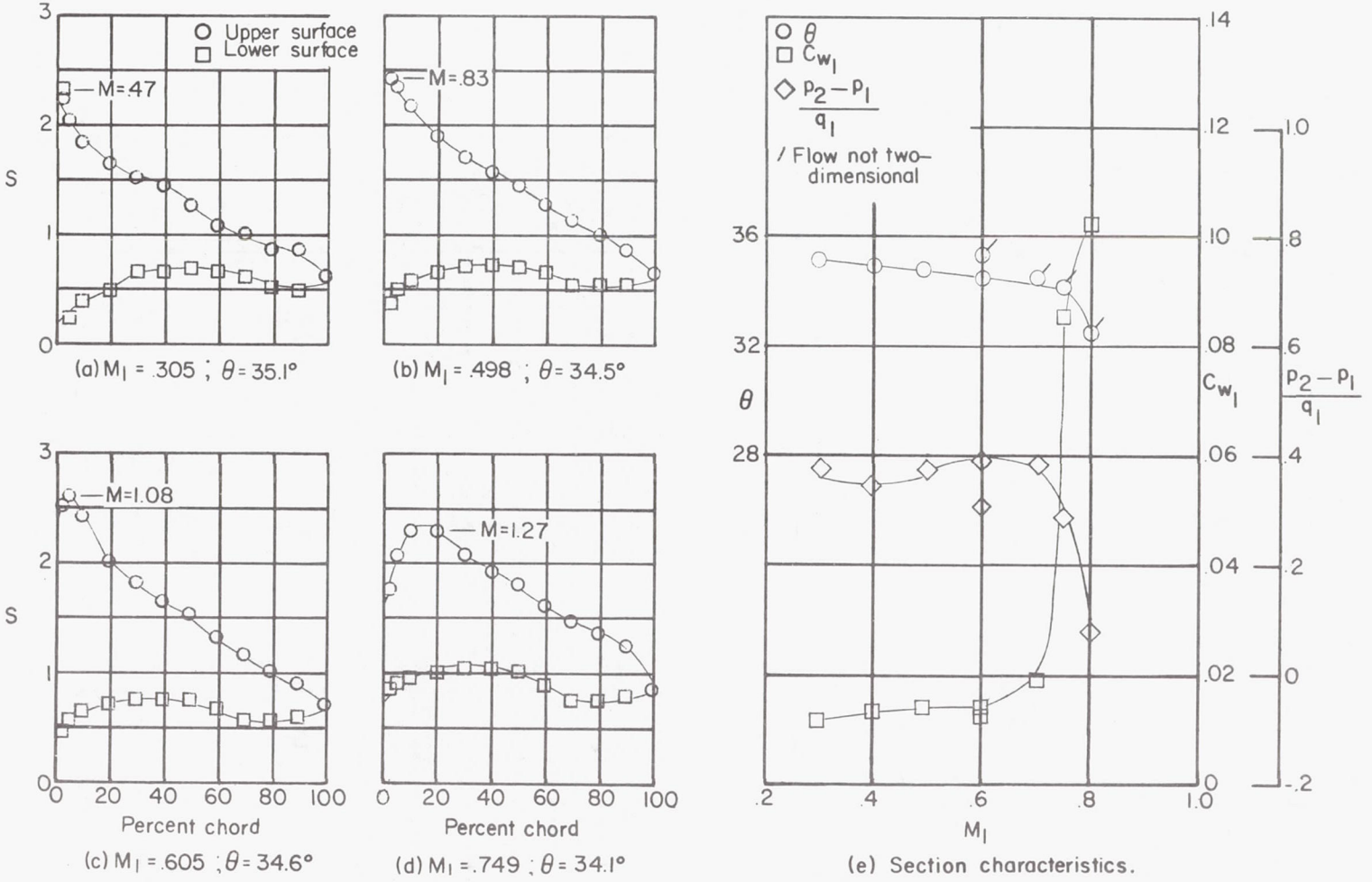


Figure 38.- Blade-surface pressure distributions and section characteristics for the cascade combination $\beta_1 = 35°$, $\sigma = 1.25$, $\alpha = 24.8°$, and NACA 65-($15A_{10}$)10 blade section.

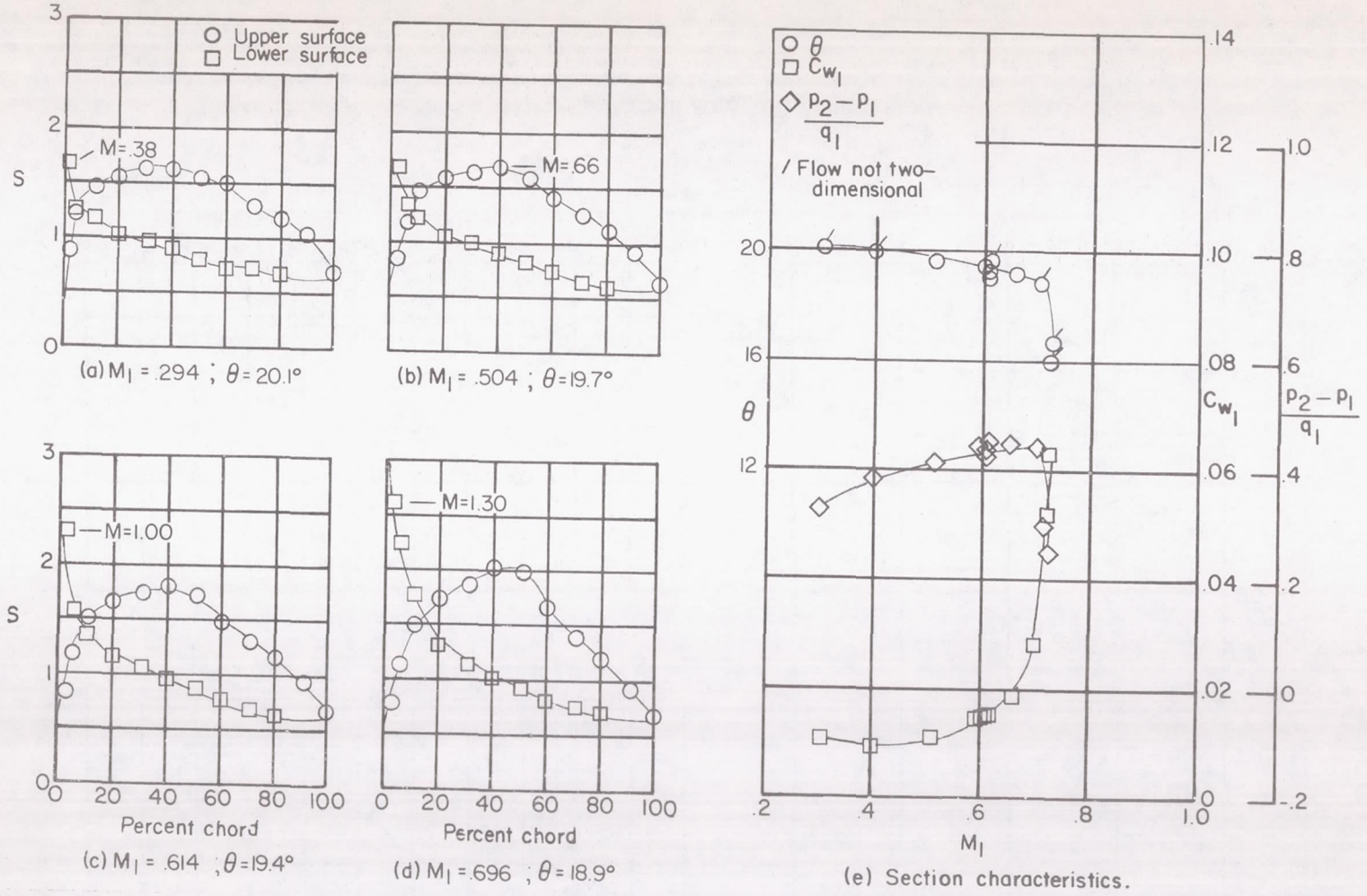


Figure 39.- Blade-surface pressure distributions and section characteristics for the cascade combination $\beta_1 = 45^\circ$, $\sigma = 1.25$, $\alpha = 11.1^\circ$, and NACA 65-($12A_{10}$)10 blade section.

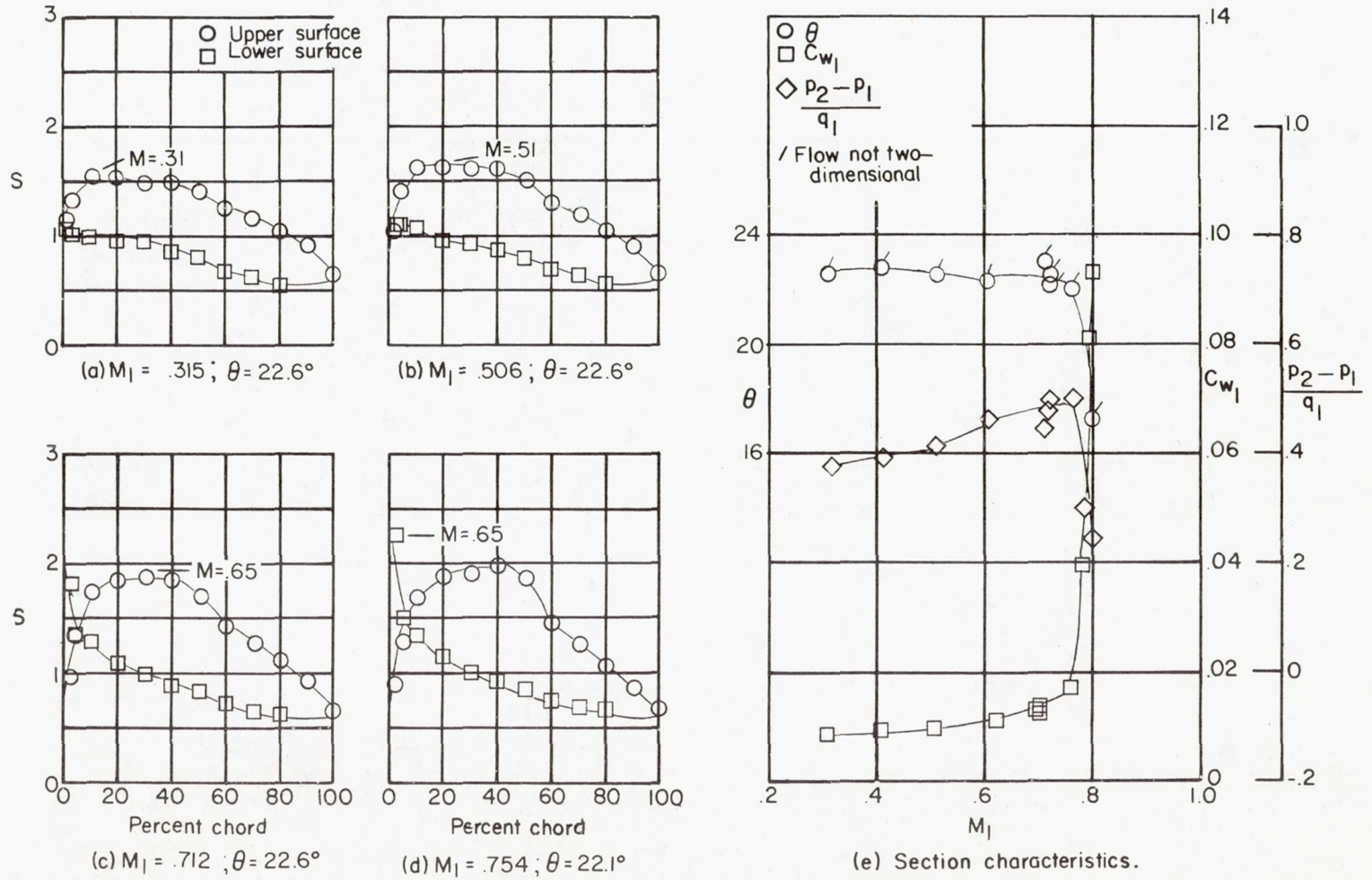


Figure 40.- Blade-surface pressure distributions and section characteristics for the cascade combination $\beta_1 = 45^\circ$, $\sigma = 1.25$, $\alpha = 14.1^\circ$, and NACA 65-($12A_{10}$)10 blade section.

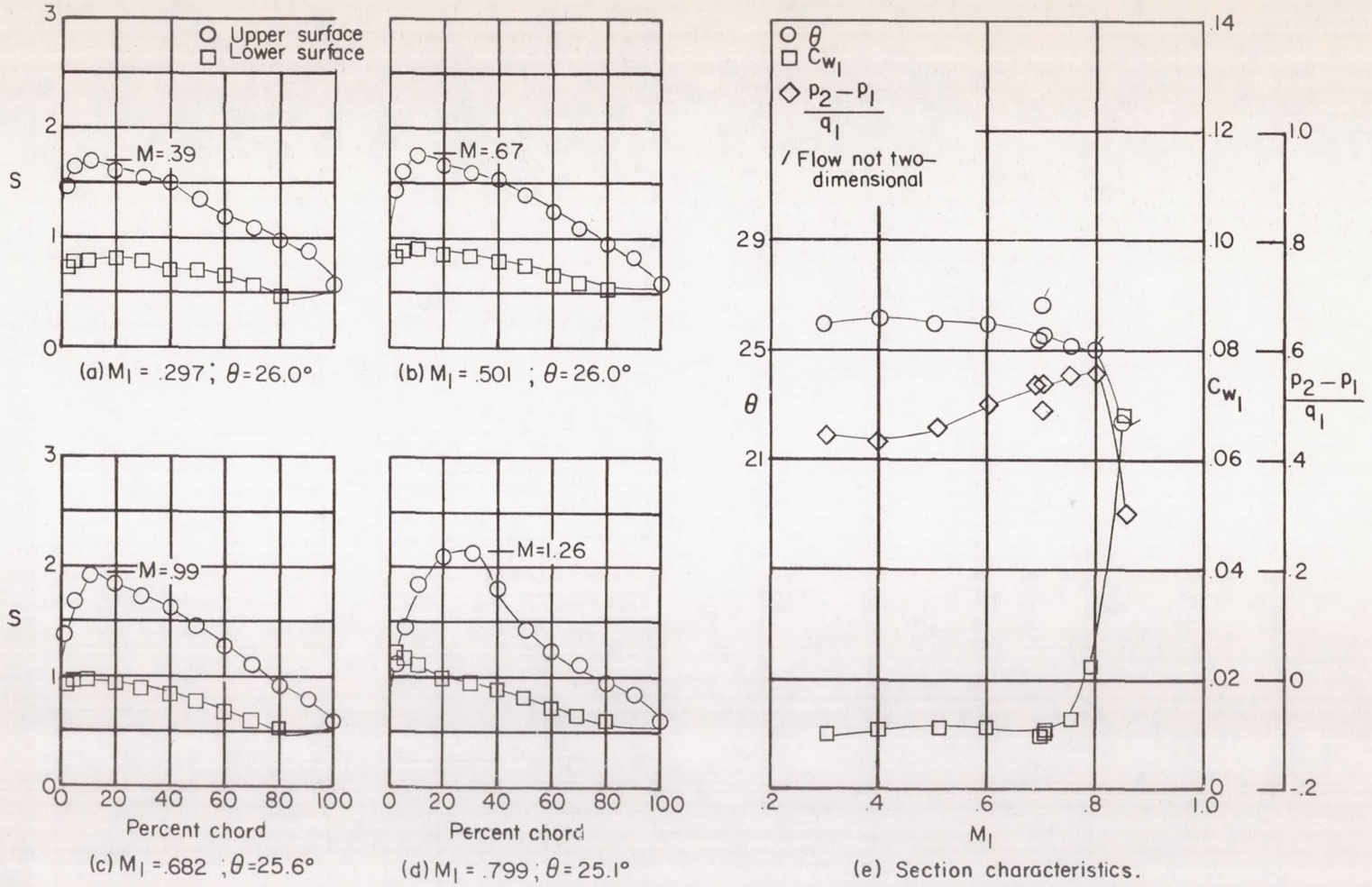


Figure 41.- Blade-surface pressure distributions and section characteristics for the cascade combination $\beta_1 = 45°$, $\sigma = 1.25$, $\alpha = 17.1°$, and NACA 65-(12A10)10 blade section.

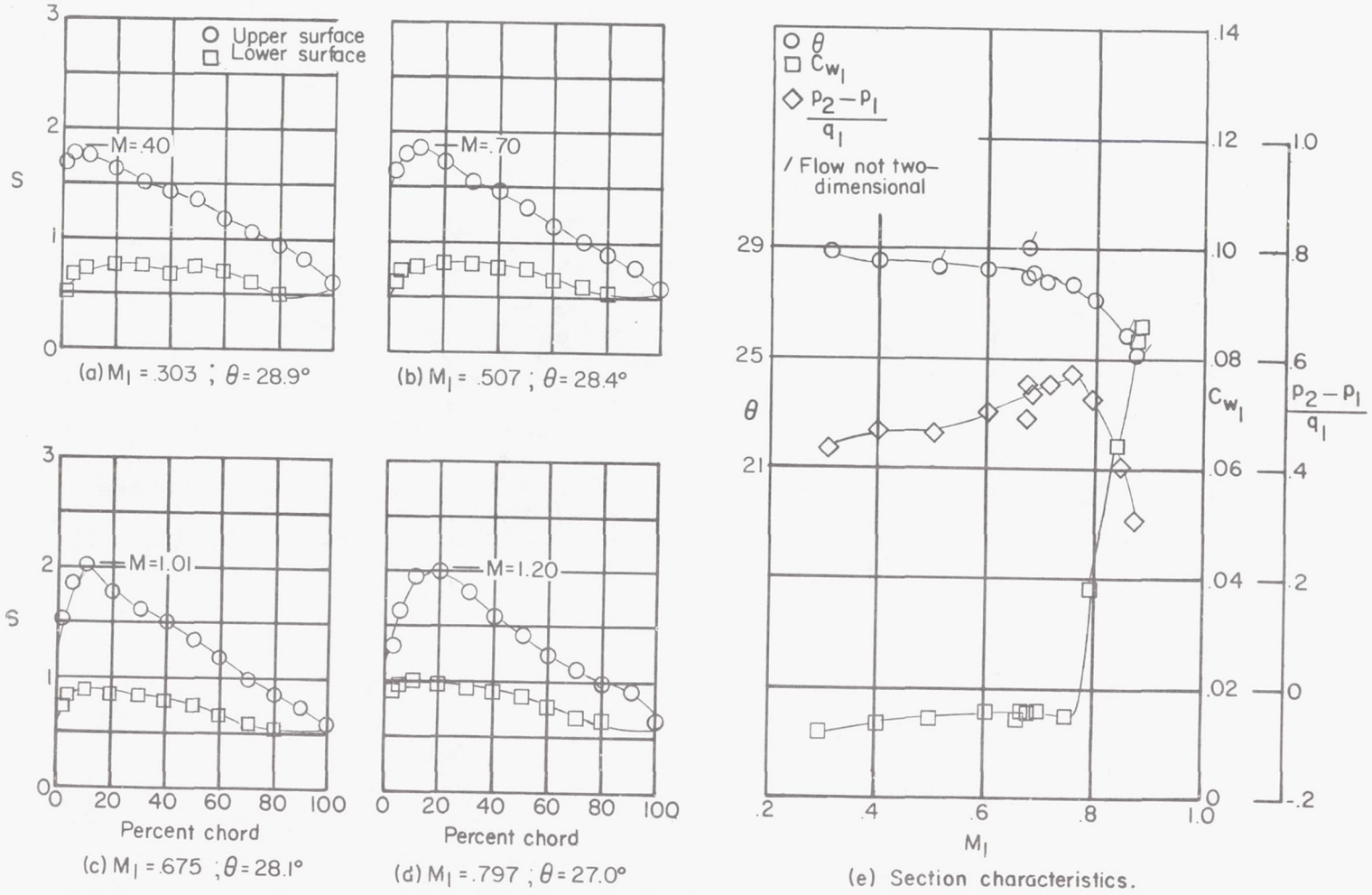


Figure 42.- Blade-surface pressure distributions and section characteristics for the cascade combination $\beta_1 = 45°$, $\sigma = 1.25$, $\alpha = 20.1°$, and NACA 65-($12A_{10}$)10 blade section.

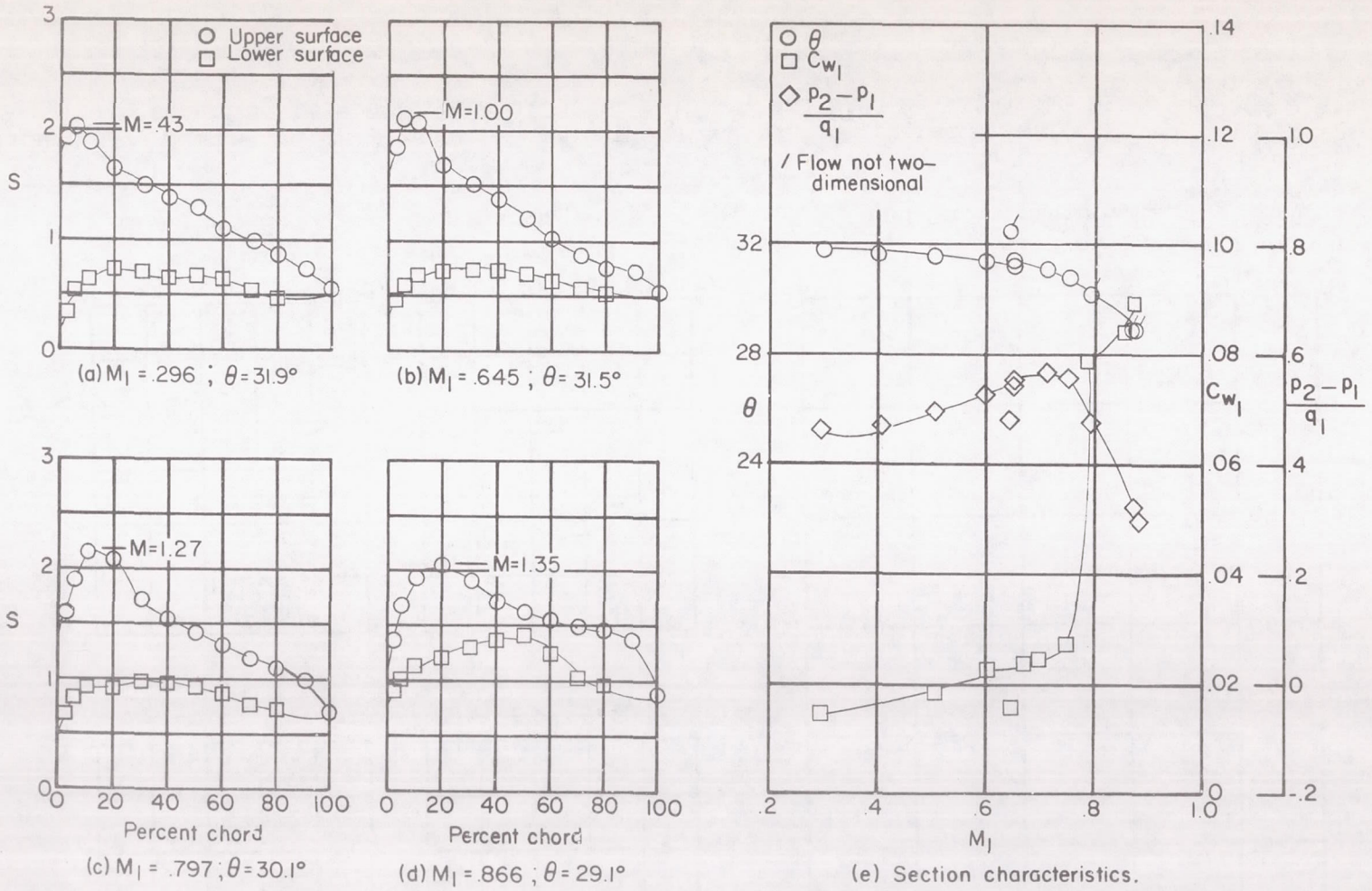


Figure 43.- Blade-surface pressure distributions and section characteristics for the cascade combination $\beta_1 = 45°$, $\sigma = 1.25$, $\alpha = 23.1°$, and NACA 65-($12A_{10}$)10 blade section.

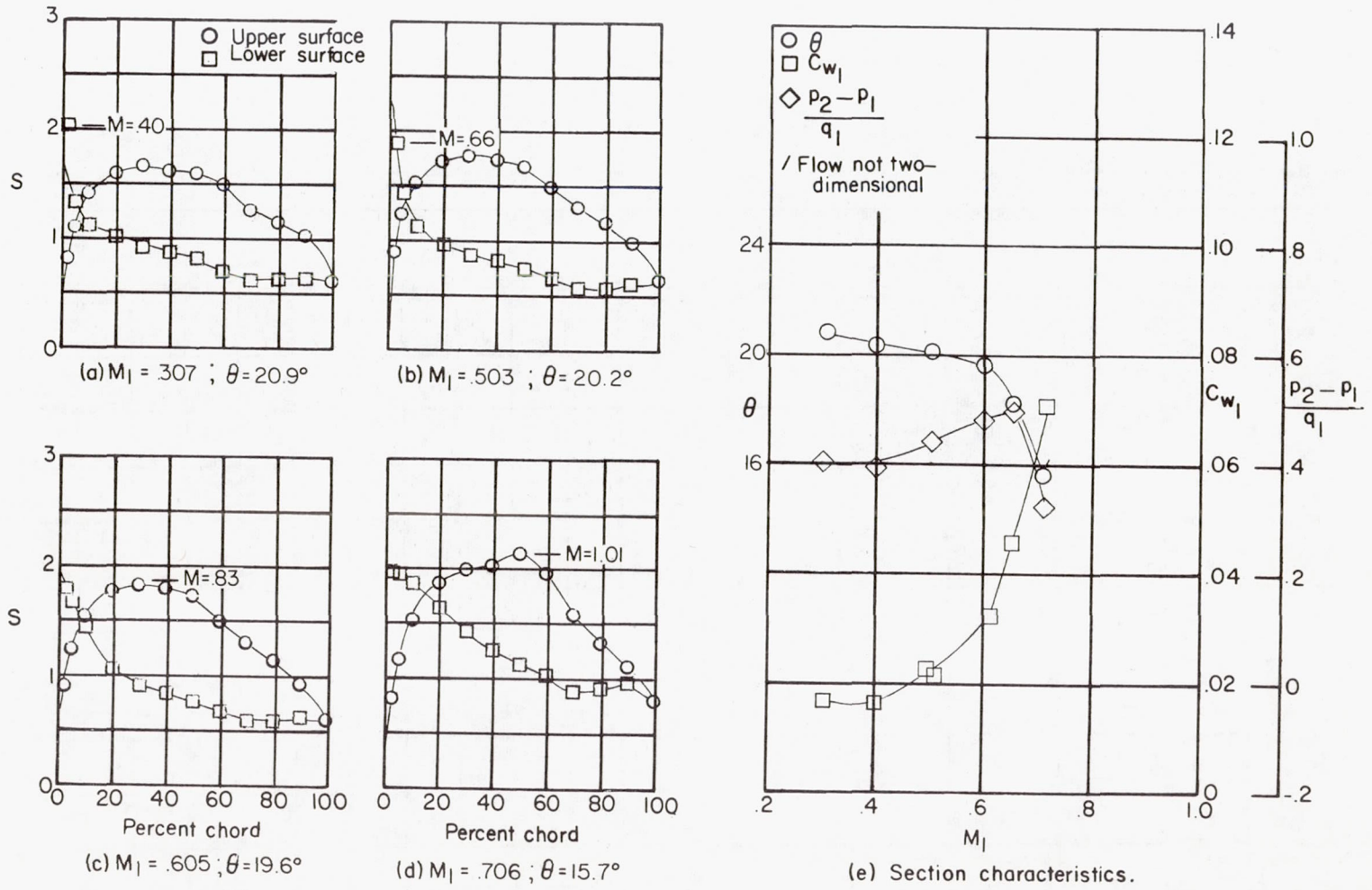


Figure 44.- Blade-surface pressure distributions and section characteristics for the cascade combination $\beta_1 = 45°$, $\sigma = 1.25$, $\alpha = 10.3°$, and NACA 65-(15A_{10})10 blade section.

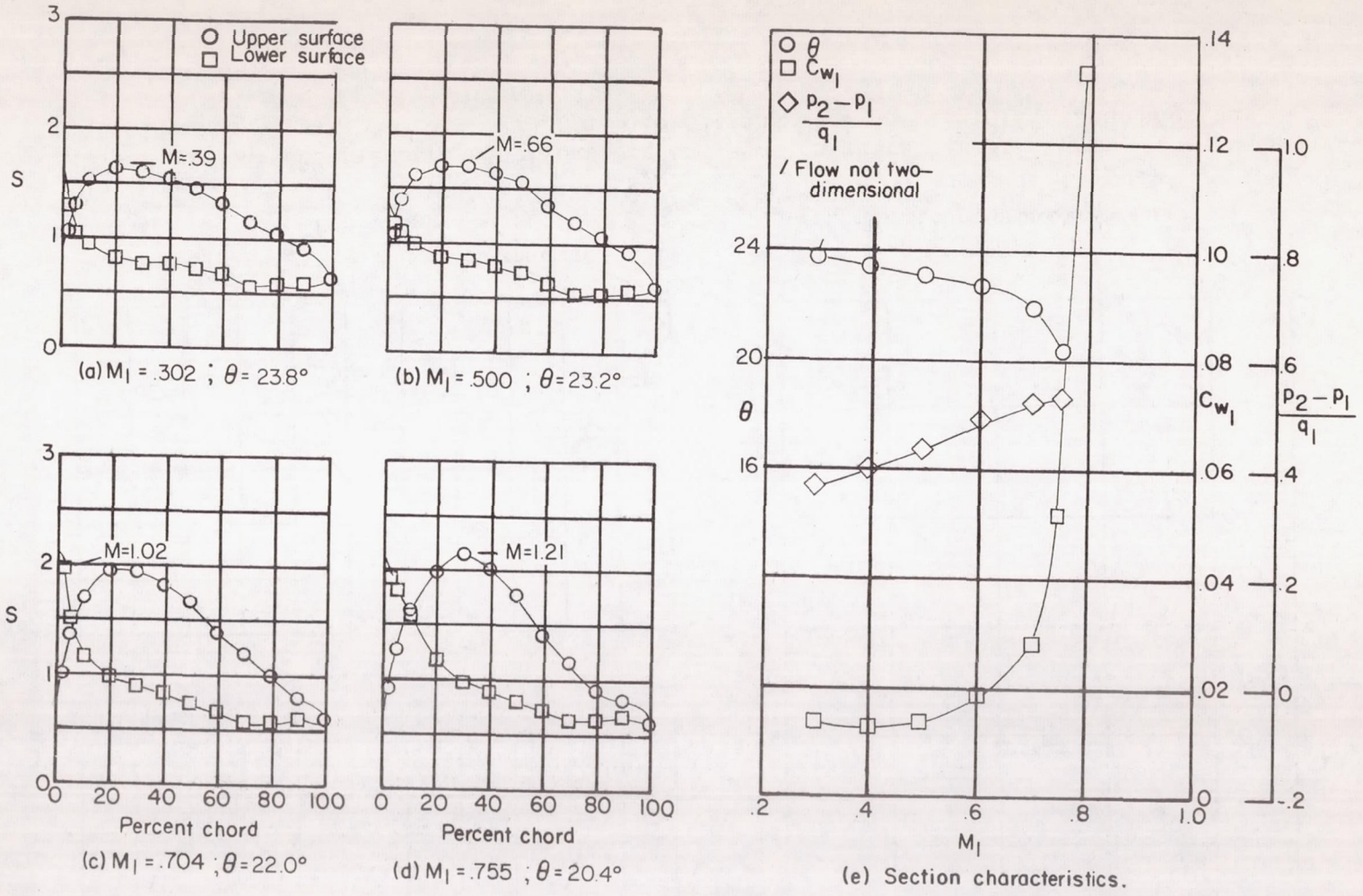


Figure 45.- Blade-surface pressure distributions and section characteristics for the cascade combination $\beta_1 = 45°$, $\sigma = 1.25$, $\alpha = 13.3°$, and NACA 65-($15A_{10}$)10 blade section.

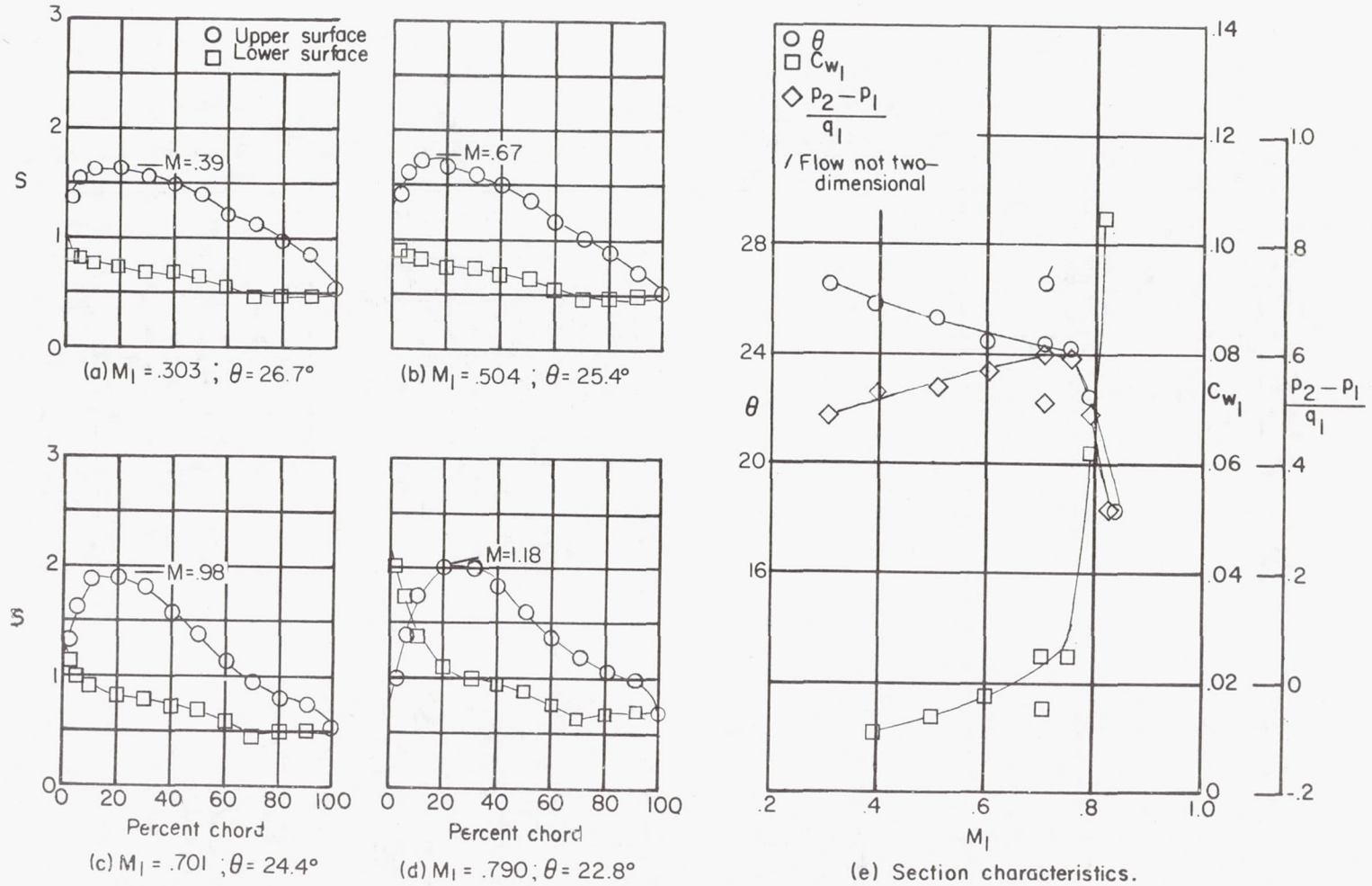


Figure 46.- Blade-surface pressure distributions and section characteristics for the cascade combination $\beta_1 = 45°$, $\sigma = 1.25$, $\alpha = 16.3°$, and NACA 65-(15A10)10 blade section.

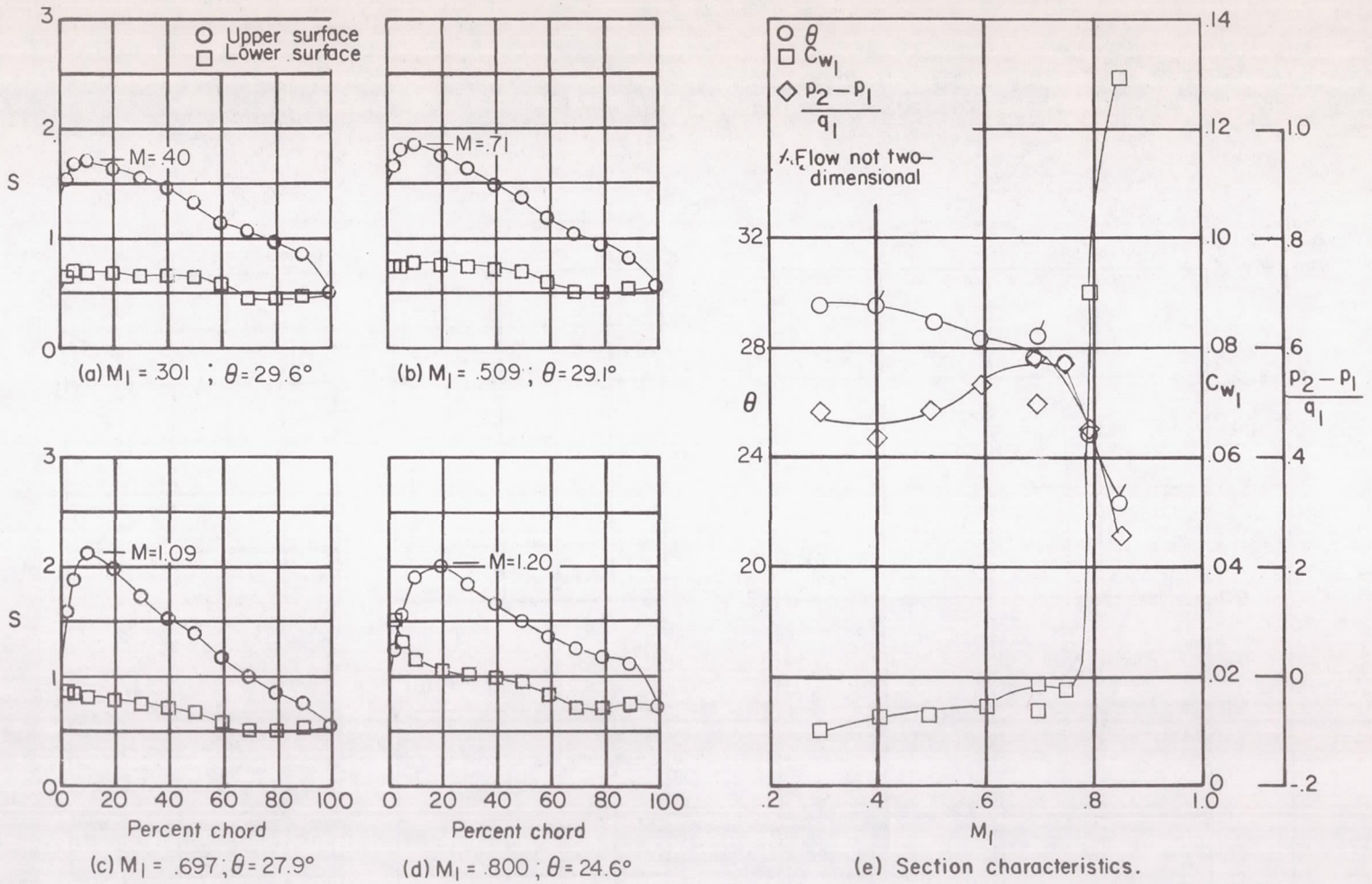


Figure 47.- Blade-surface pressure distributions and section characteristics for the cascade combination $\beta_1 = 45°$, $\sigma = 1.25$, $\alpha = 19.3°$, and NACA 65-($15A_{10}$)10 blade section.

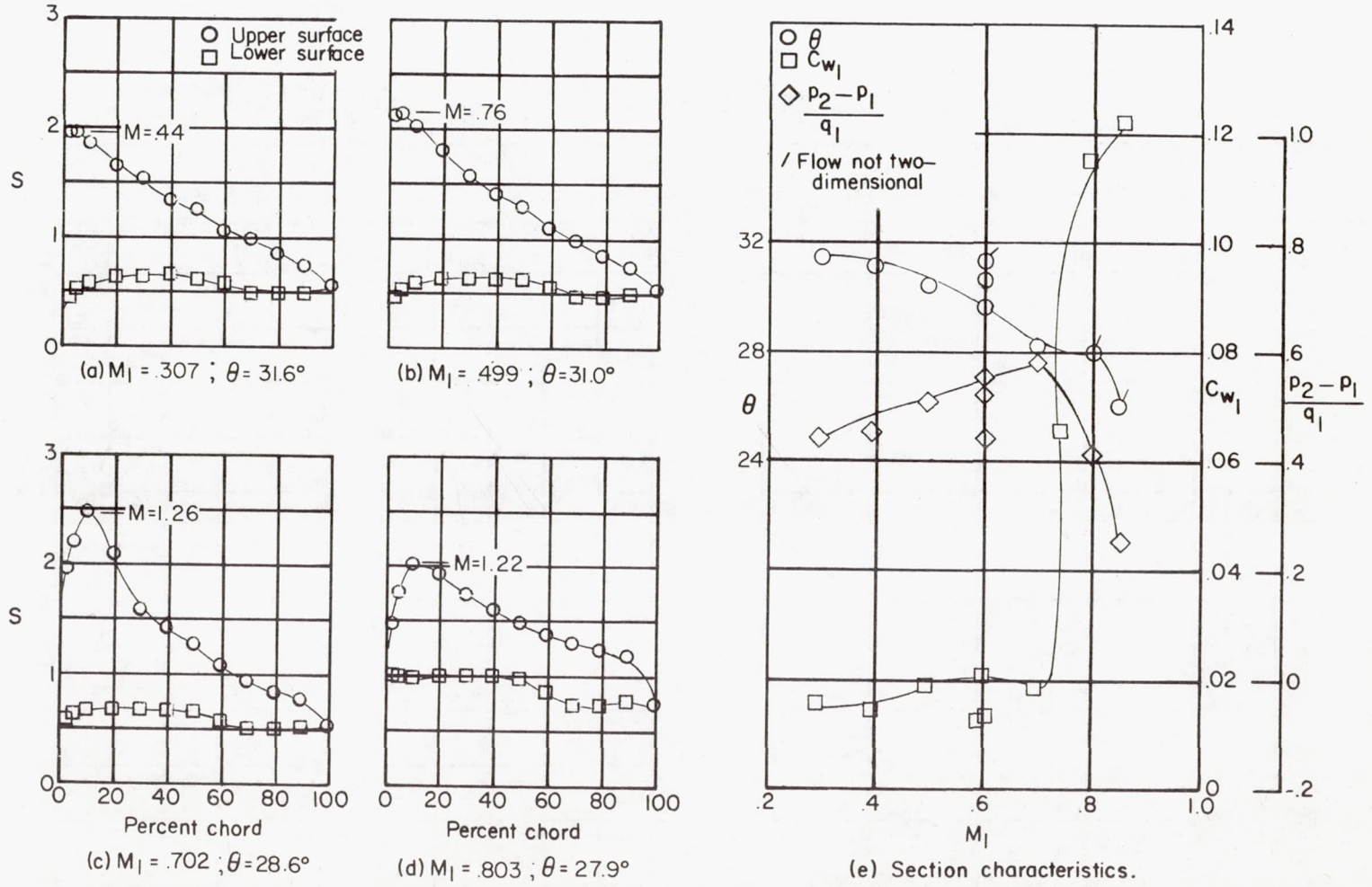


Figure 48.- Blade-surface pressure distributions and section characteristics for the cascade combination $\beta_1 = 45°$, $\sigma = 1.25$, $\alpha = 22.3°$, and NACA 65-(15A10)10 blade section.

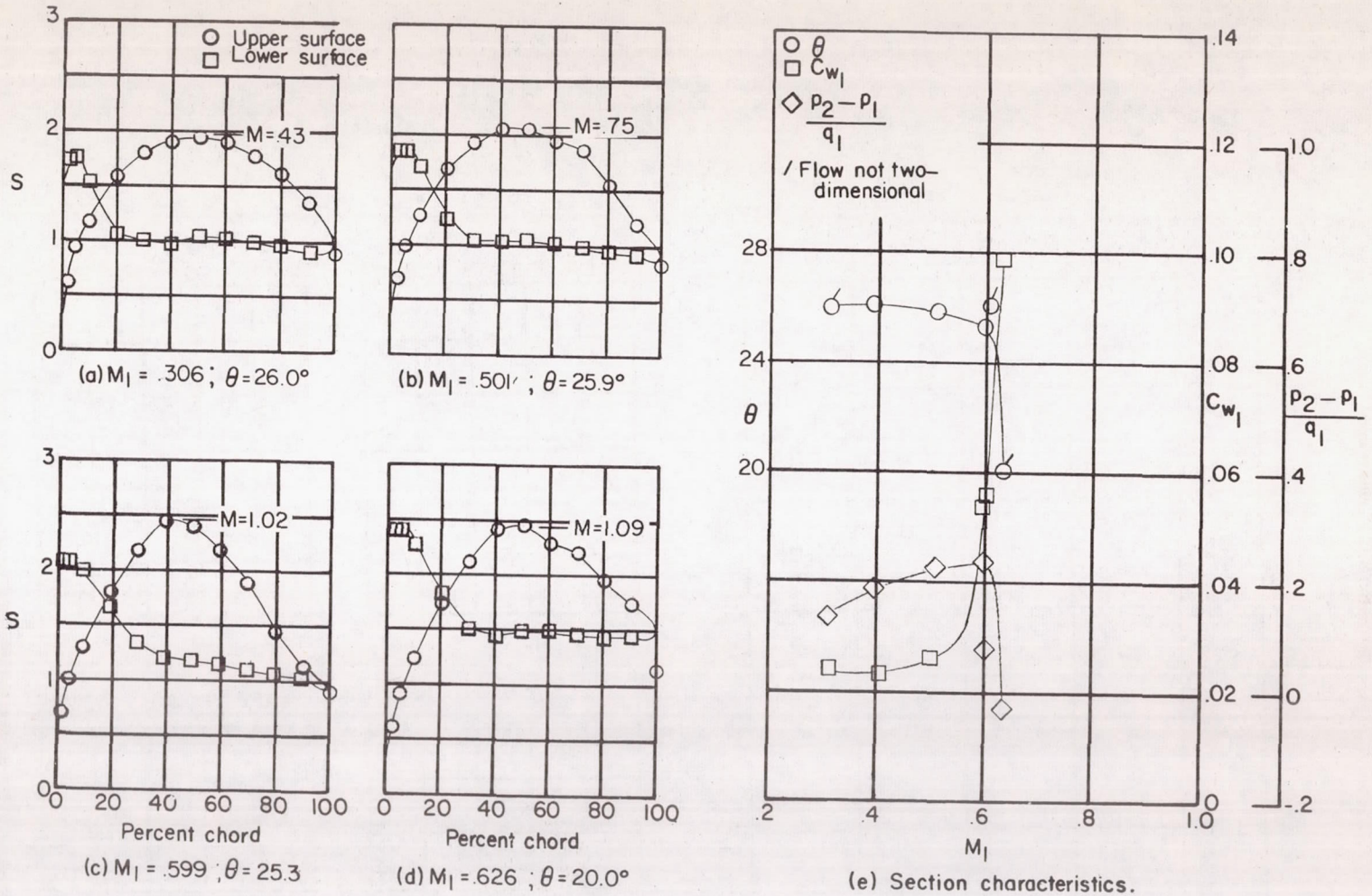


Figure 49.- Blade-surface pressure distributions and section characteristics for the cascade combination $\beta_1 = 25°$, $\sigma = 1.5$, $\alpha = 11.2°$, and circular-arc configuration I.

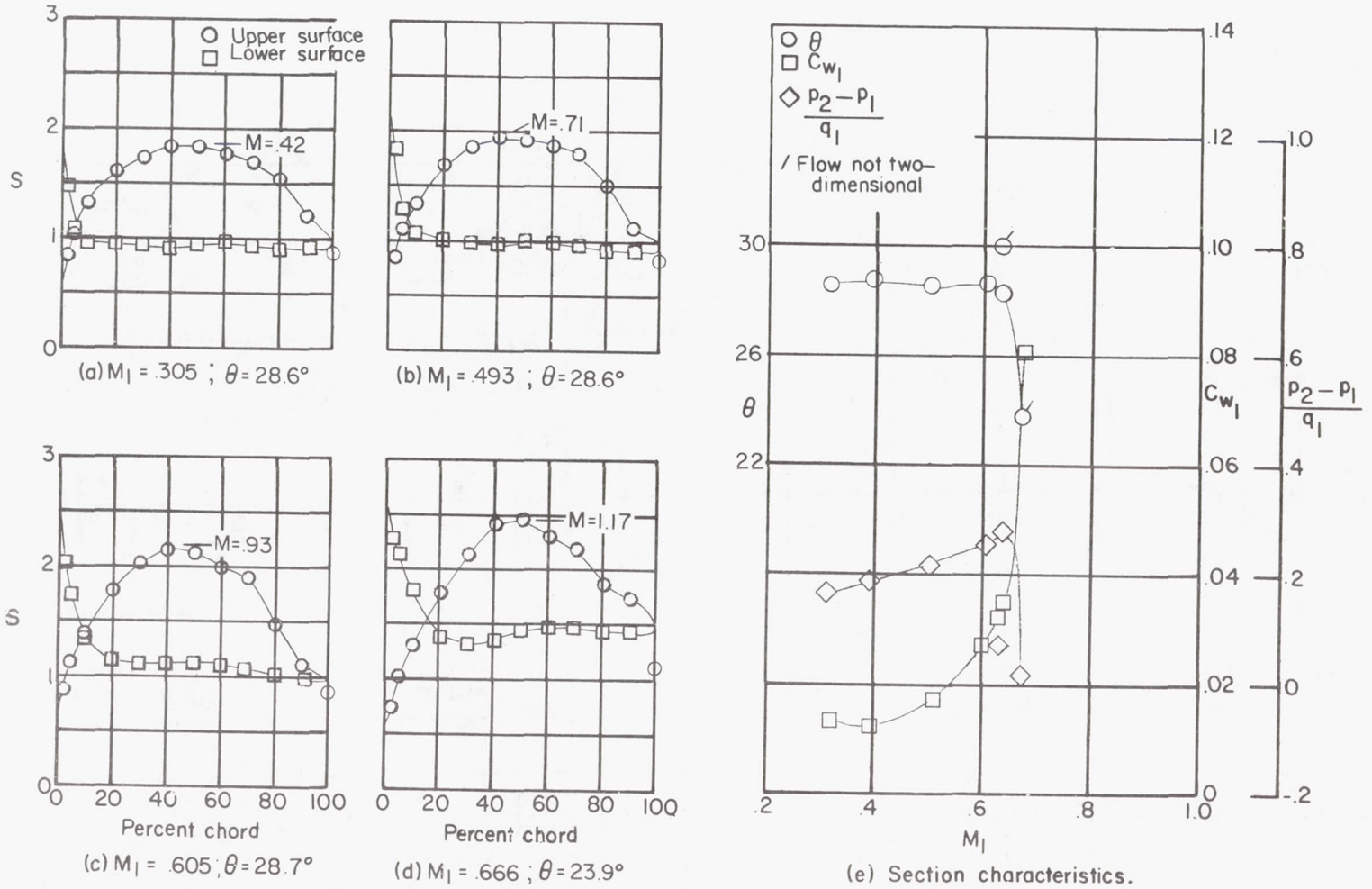


Figure 50.- Blade-surface pressure distributions and section characteristics for the cascade combination $\beta_1 = 25°$, $\sigma = 1.5$, $\alpha = 14.2°$, and circular-arc configuration I.

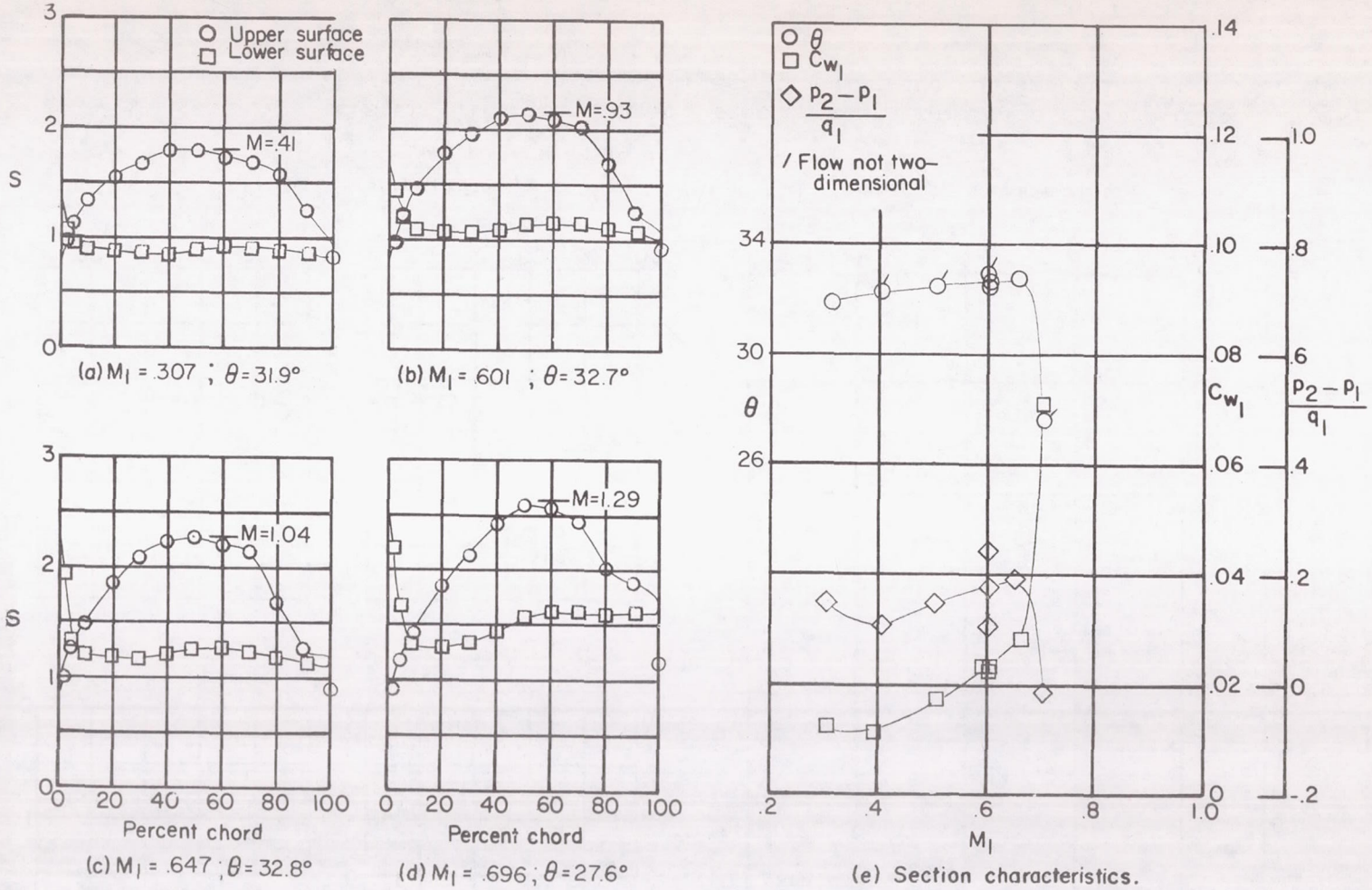


Figure 51.- Blade-surface pressure distributions and section characteristics for the cascade combination $\beta_1 = 25^\circ$, $\sigma = 1.5$, $\alpha = 17.2^\circ$, and circular-arc configuration I.

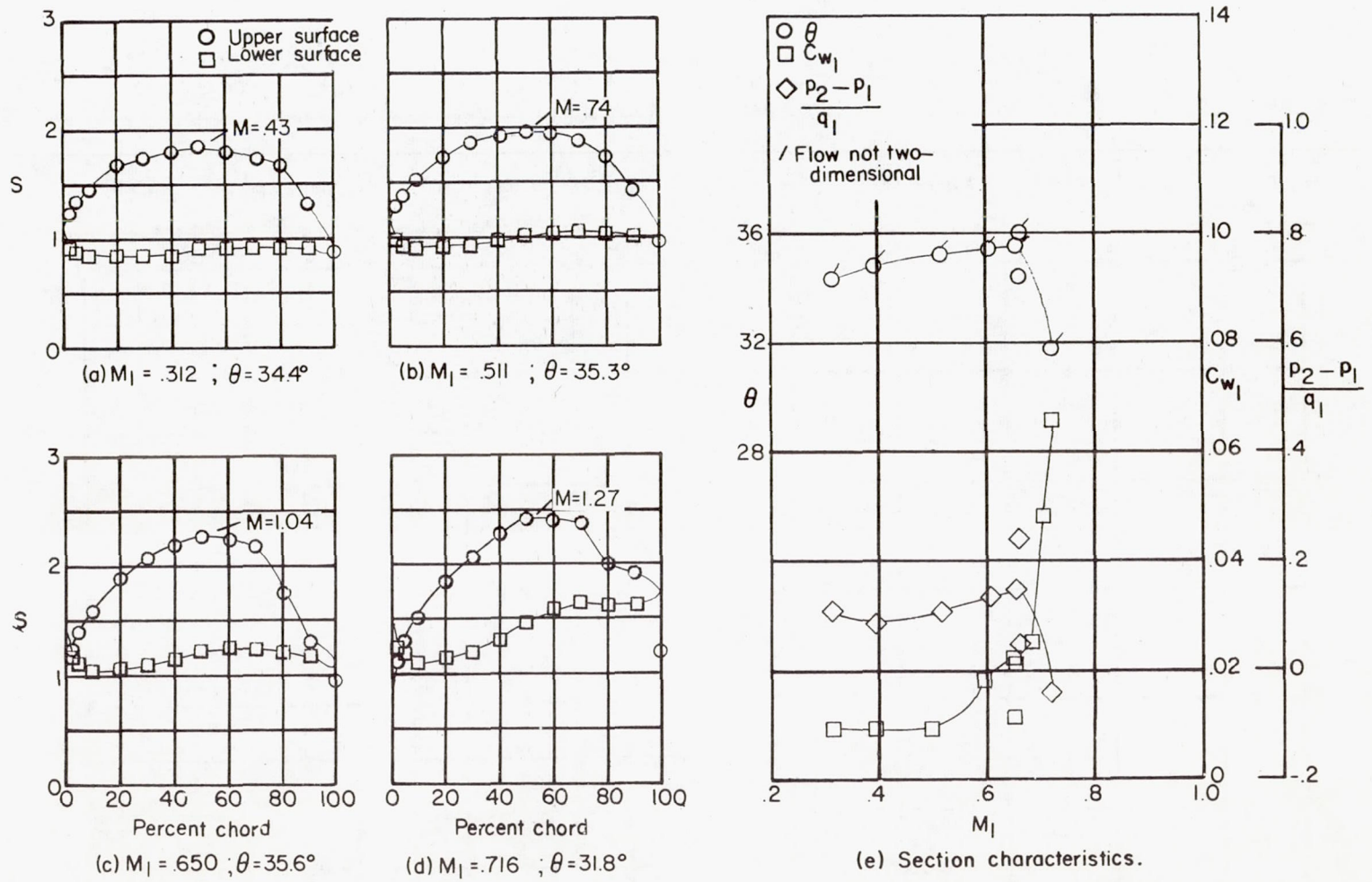


Figure 52.- Blade-surface pressure distributions and section characteristics for the cascade combination $\beta_1 = 25^\circ$, $\sigma = 1.5$, $\alpha = 20.2^\circ$, and circular-arc configuration I.

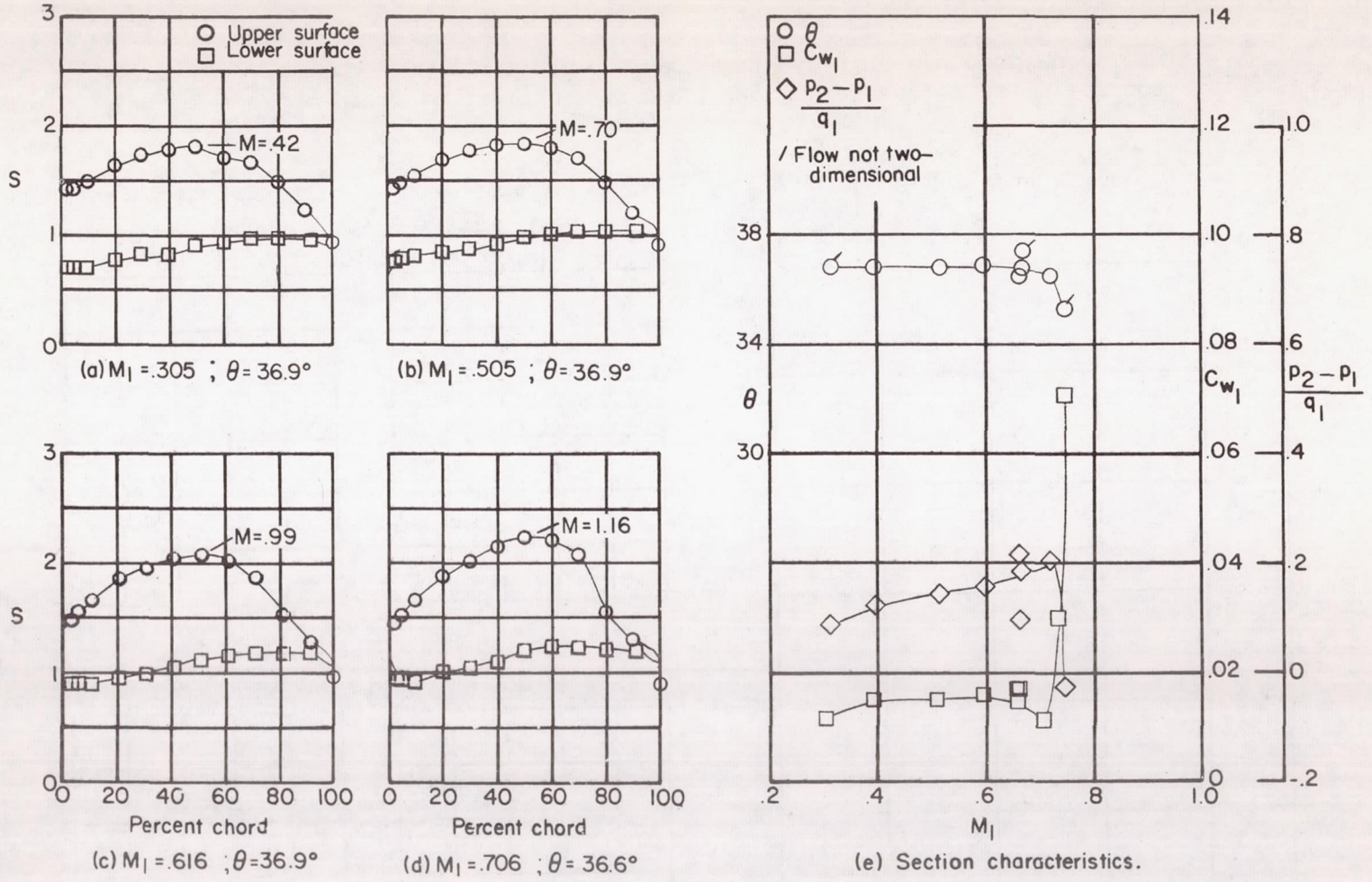


Figure 53.- Blade-surface pressure distributions and section characteristics for the cascade combination $\beta_1 = 25^\circ$, $\sigma = 1.5$, $\alpha = 23.2^\circ$, and circular-arc configuration I.

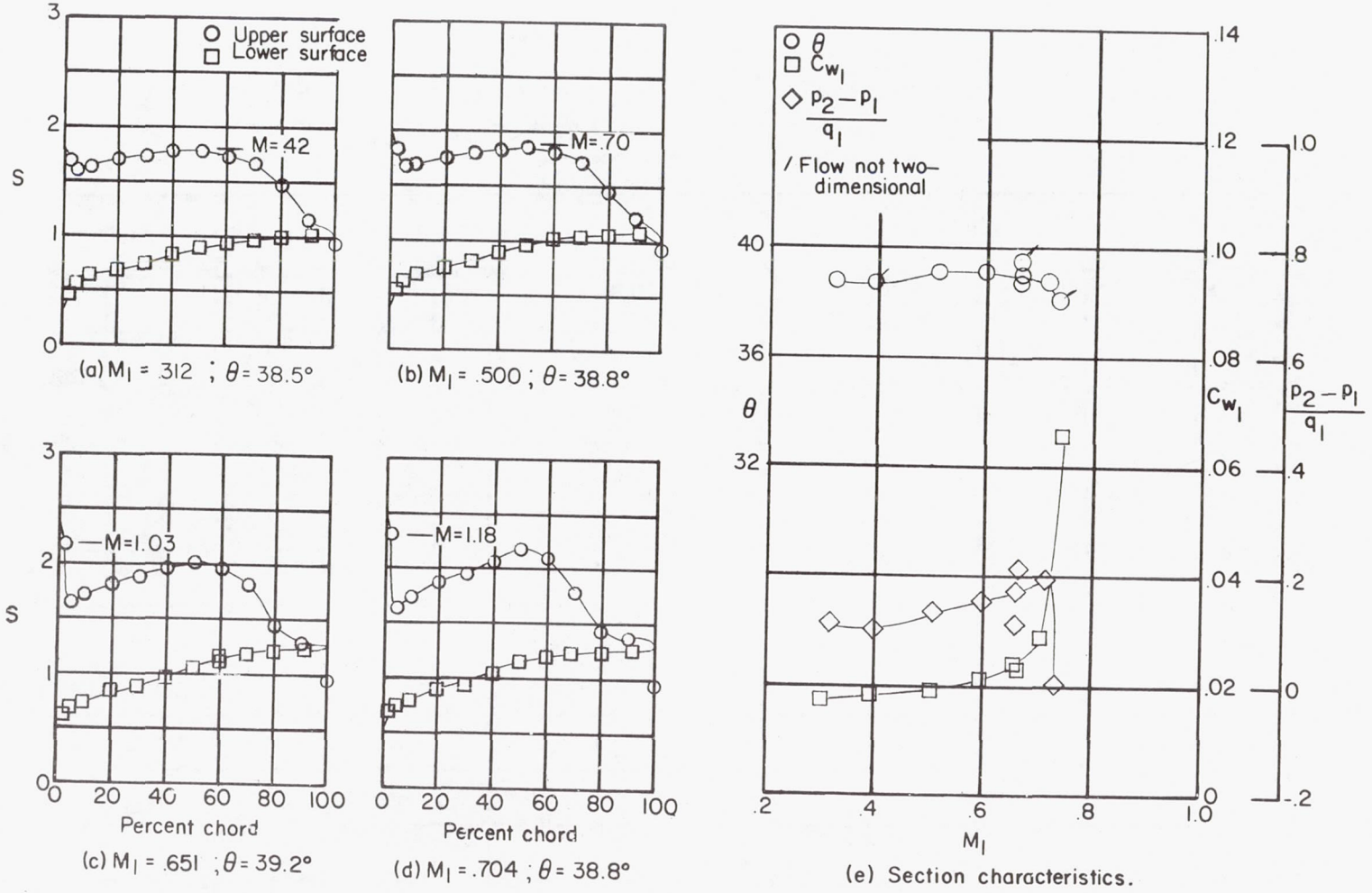


Figure 54.- Blade-surface pressure distributions and section characteristics for the cascade combination $\beta_1 = 25^\circ$, $\sigma = 1.5$, $\alpha = 26.2^\circ$, and circular-arc configuration I.

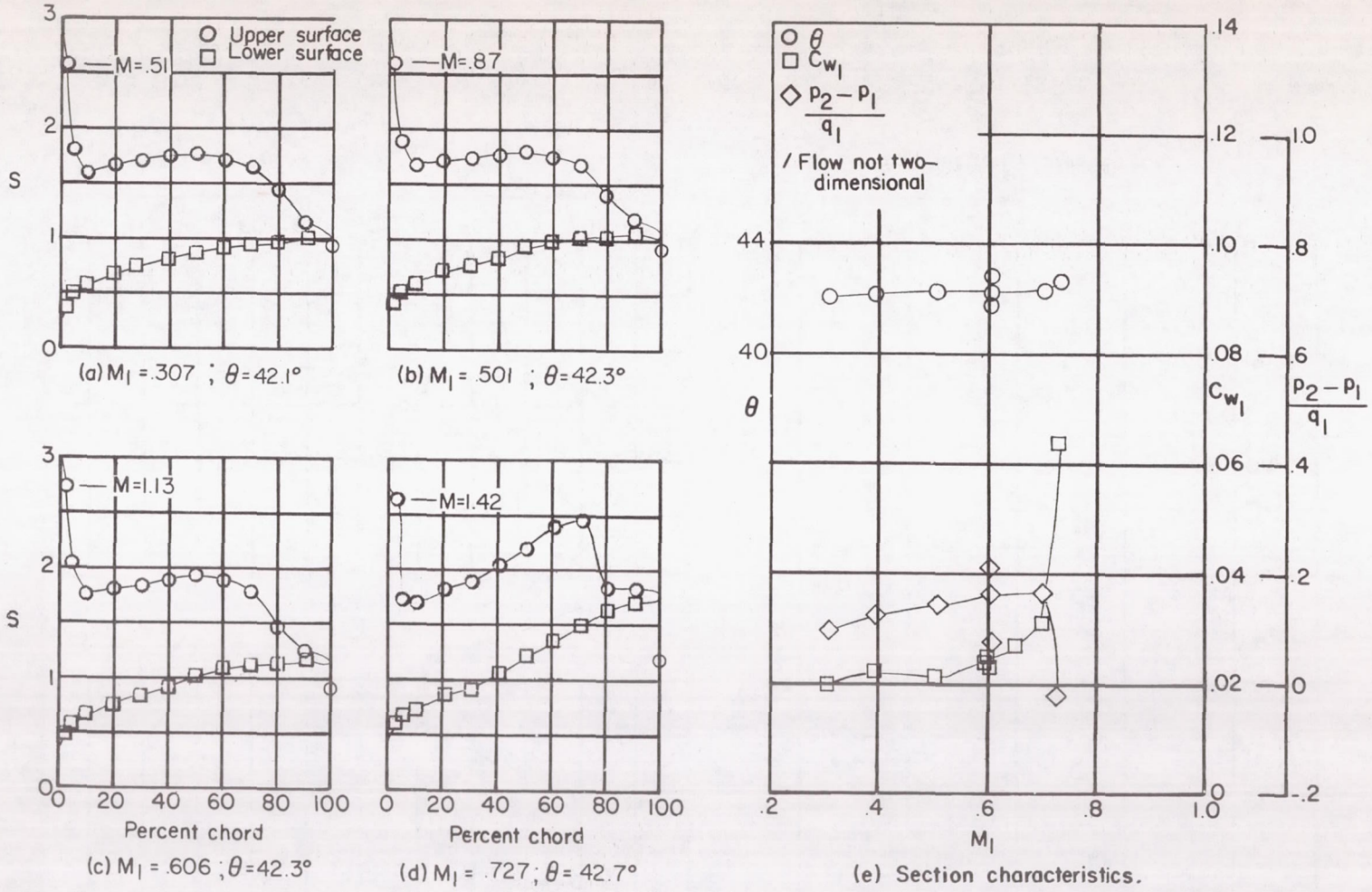


Figure 55.- Blade-surface pressure distributions and section characteristics for the cascade combination $\beta_1 = 25°$, $\sigma = 1.5$, $\alpha = 29.2°$, and circular-arc configuration I.

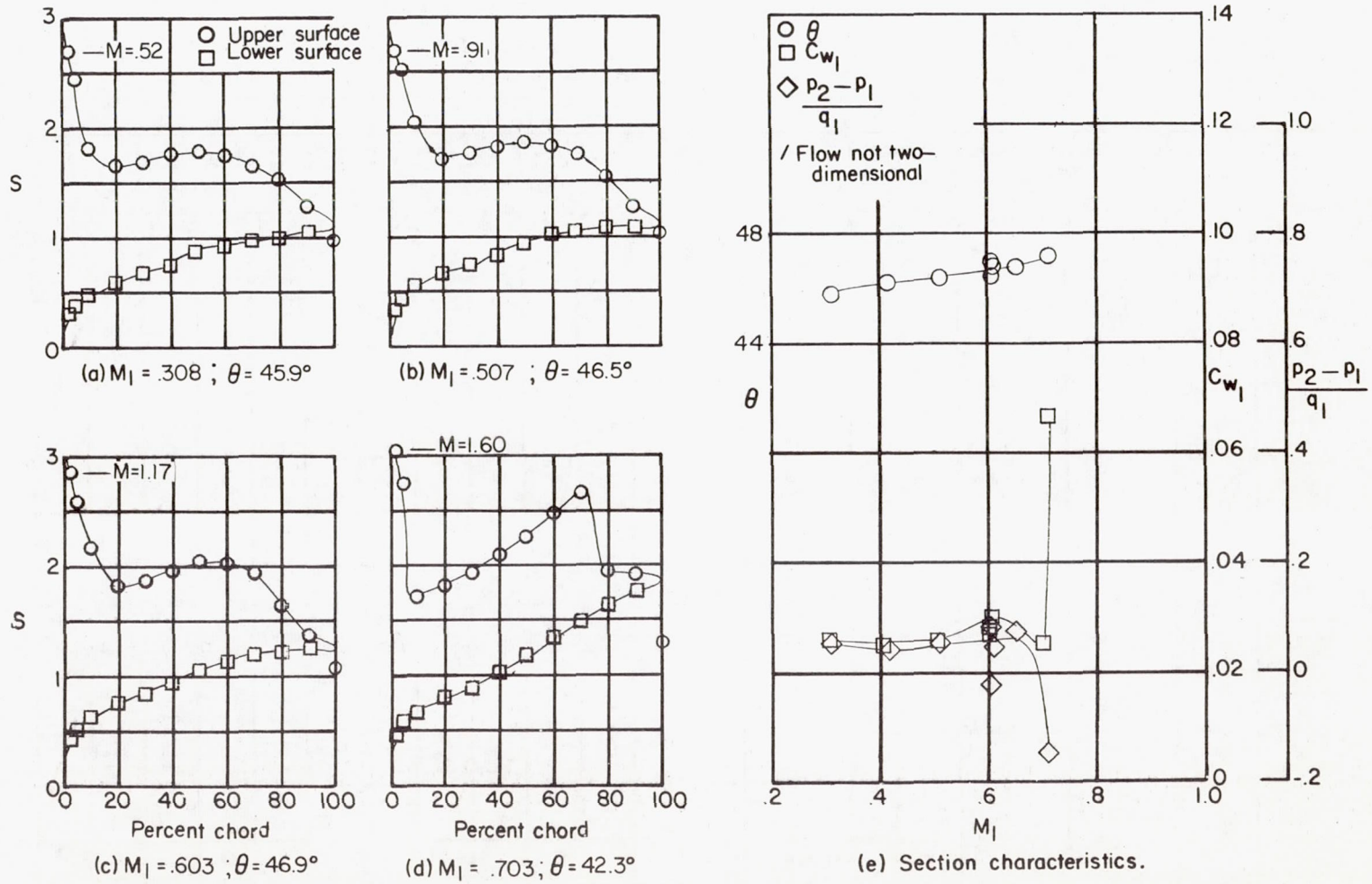


Figure 56.- Blade-surface pressure distributions and section characteristics for the cascade combination $\beta_1 = 25^\circ$, $\sigma = 1.5$, $\alpha = 32.2^\circ$, and circular-arc configuration I.

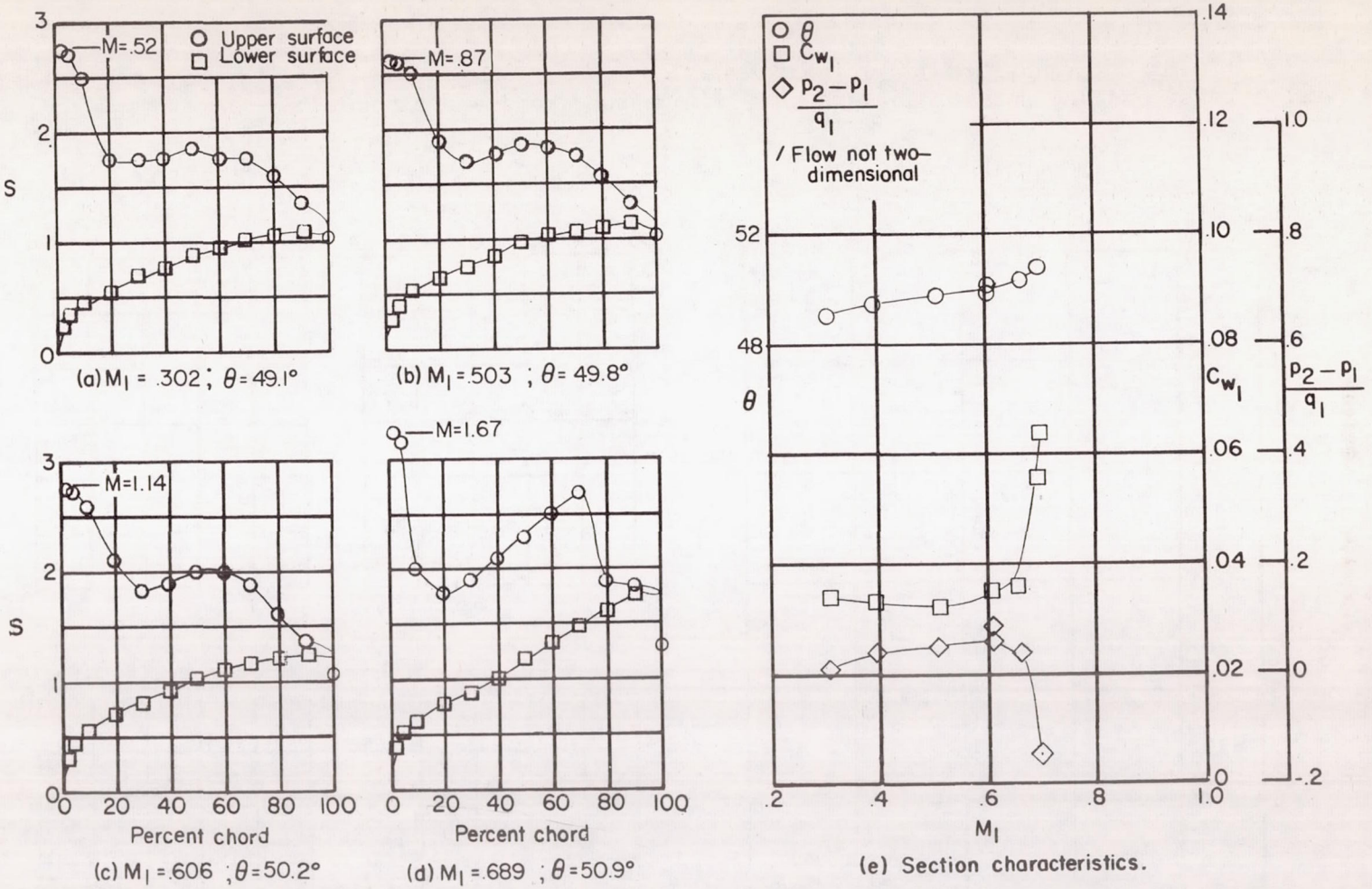


Figure 57.- Blade-surface pressure distributions and section characteristics for the cascade combination $\beta_1 = 25^\circ$, $\sigma = 1.5$, $\alpha = 35.2^\circ$, and circular-arc configuration I.

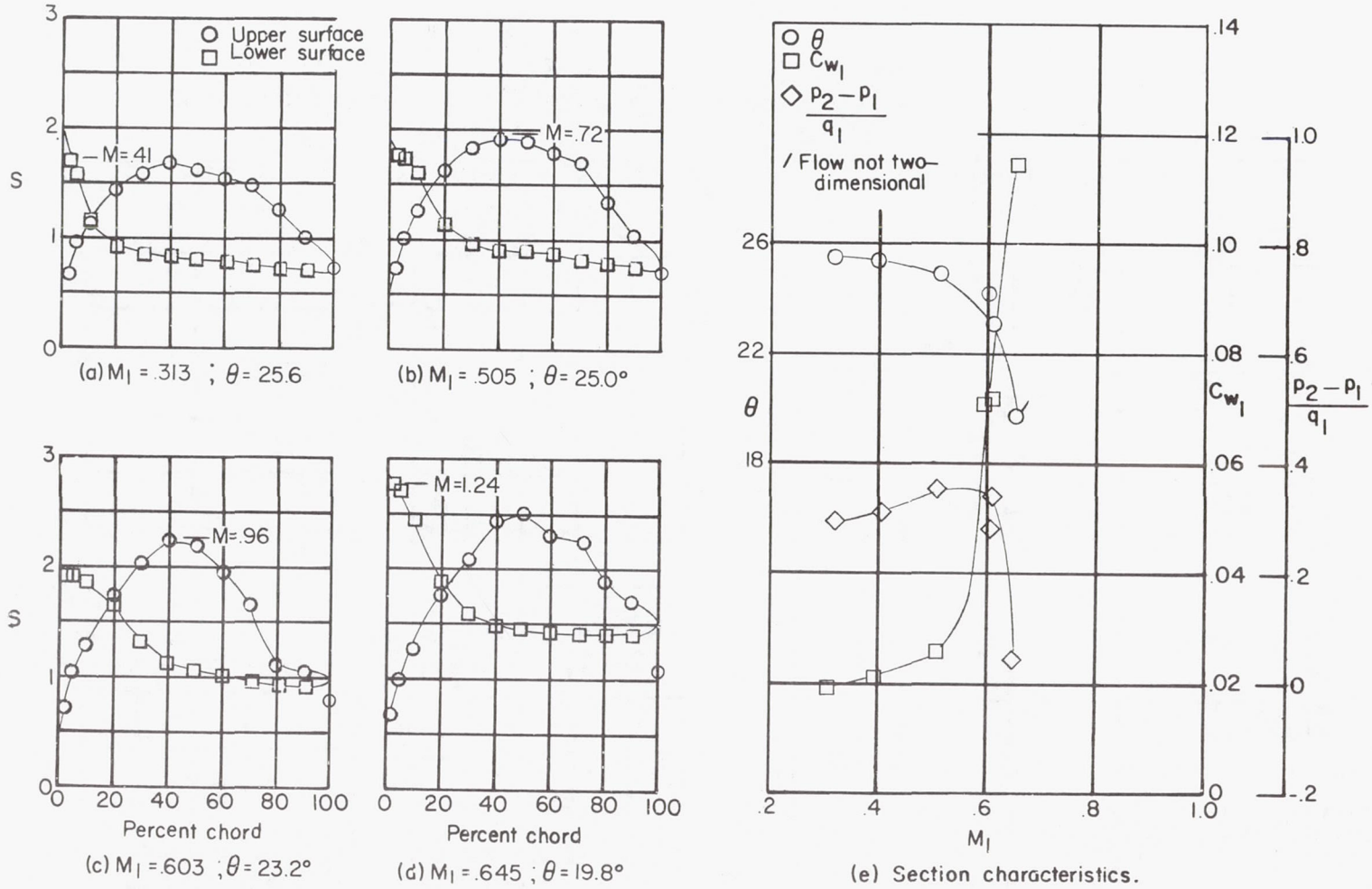


Figure 58.- Blade-surface pressure distributions and section characteristics for the cascade combination $\beta_1 = 35^\circ$, $\sigma = 1.5$, $\alpha = 12.2^\circ$, and circular-arc configuration I.

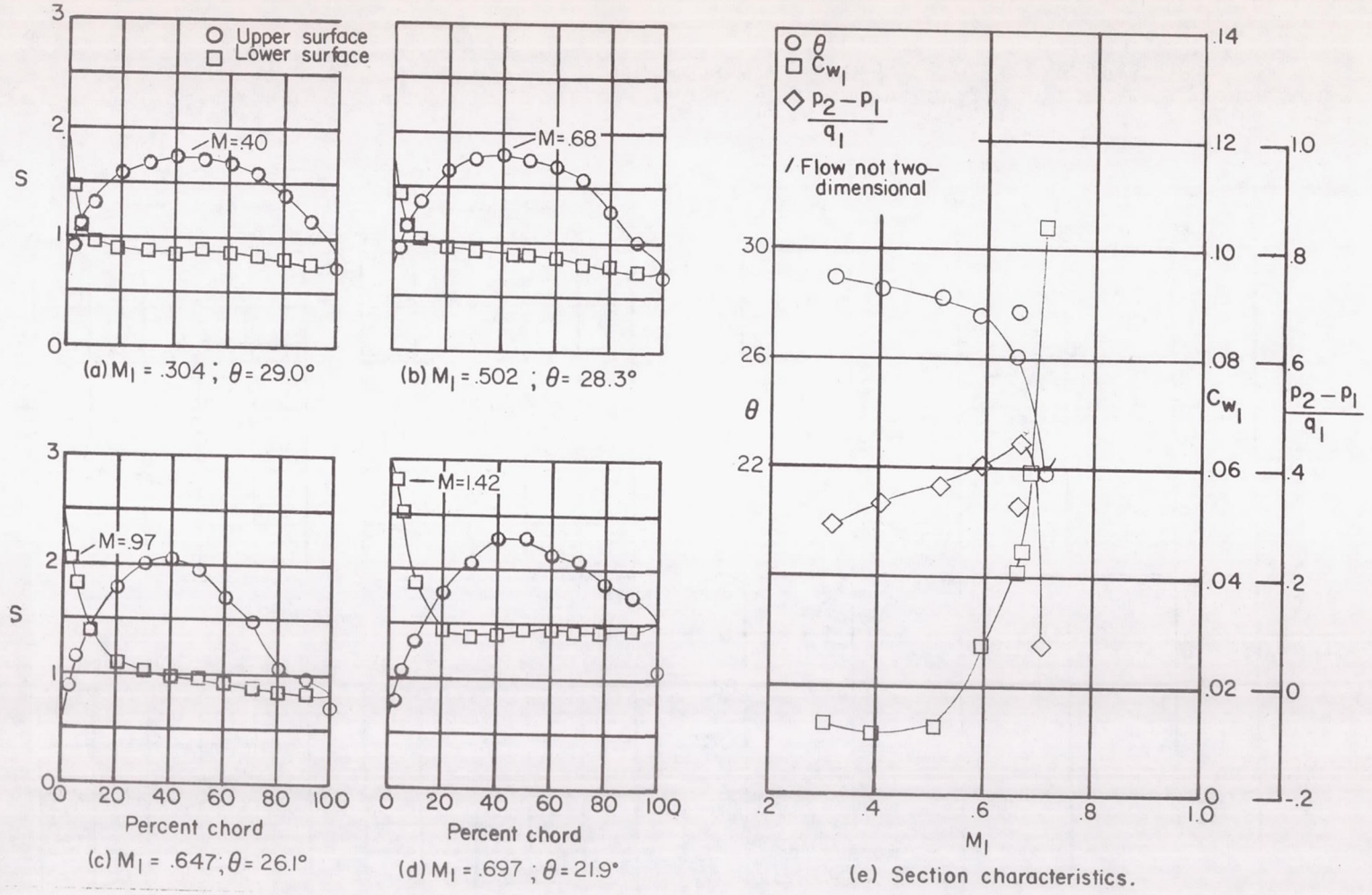


Figure 59.- Blade-surface pressure distributions and section characteristics for the cascade combination $\beta_1 = 35^\circ$, $\sigma = 1.5$, $\alpha = 15.2^\circ$, and circular-arc configuration I.

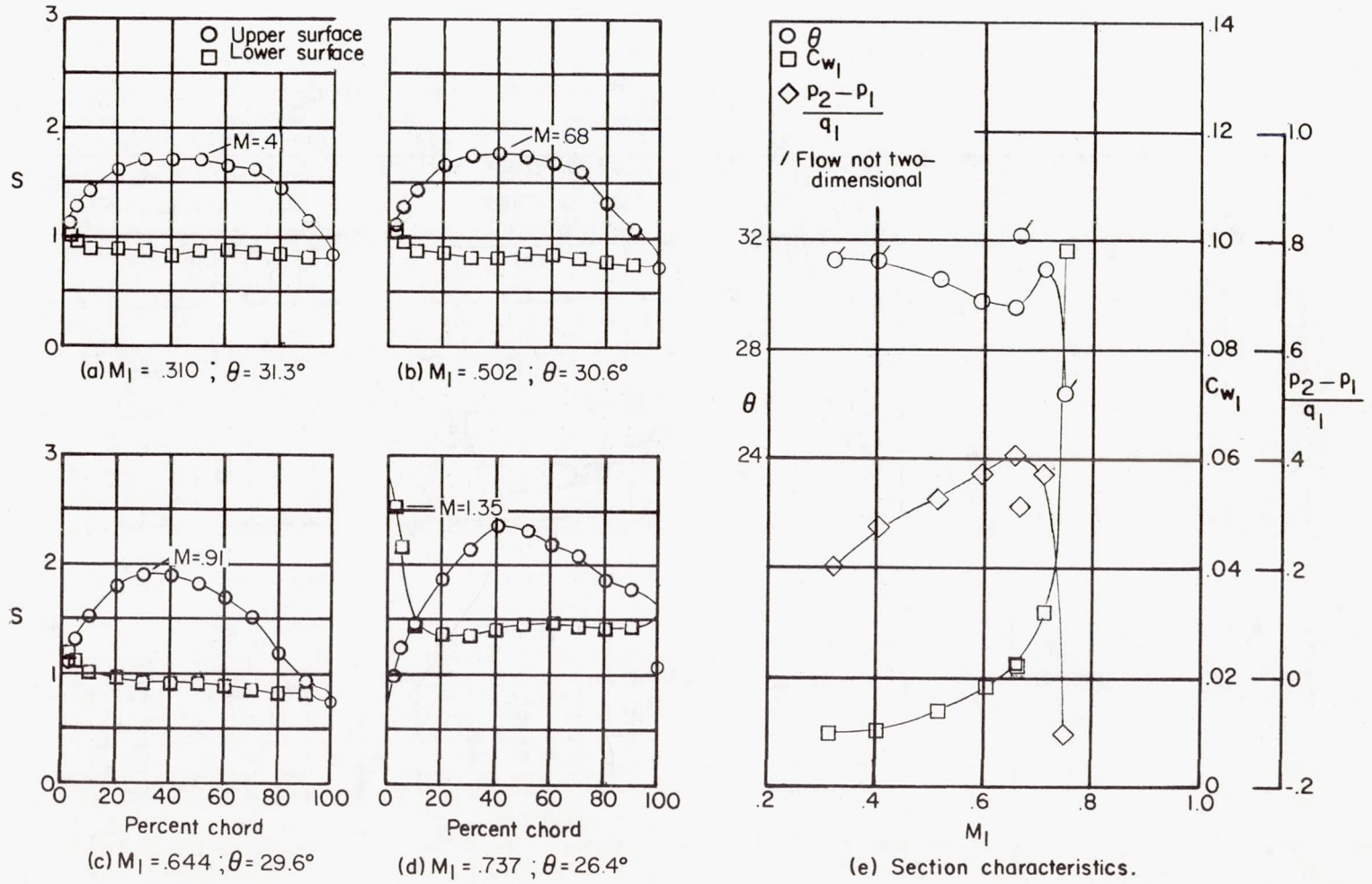


Figure 60.- Blade-surface pressure distributions and section characteristics for the cascade combination $\beta_1 = 35°$, $\sigma = 1.5$, $\alpha = 18.2°$, and circular-arc configuration I.

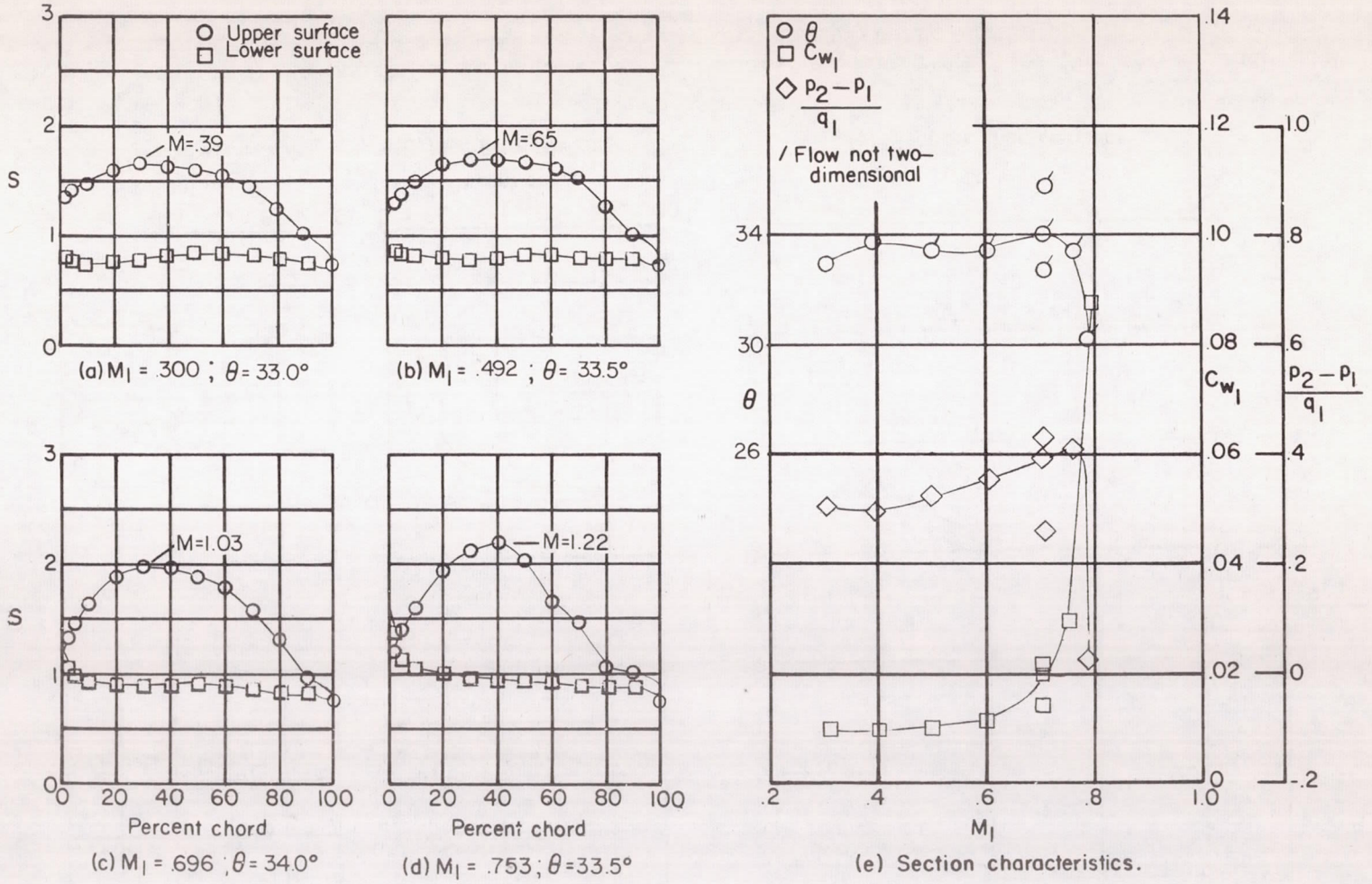


Figure 61.- Blade-surface pressure distributions and section characteristics for the cascade combination $\beta_1 = 35°$, $\sigma = 1.5$, $\alpha = 21.2°$, and circular-arc configuration I.

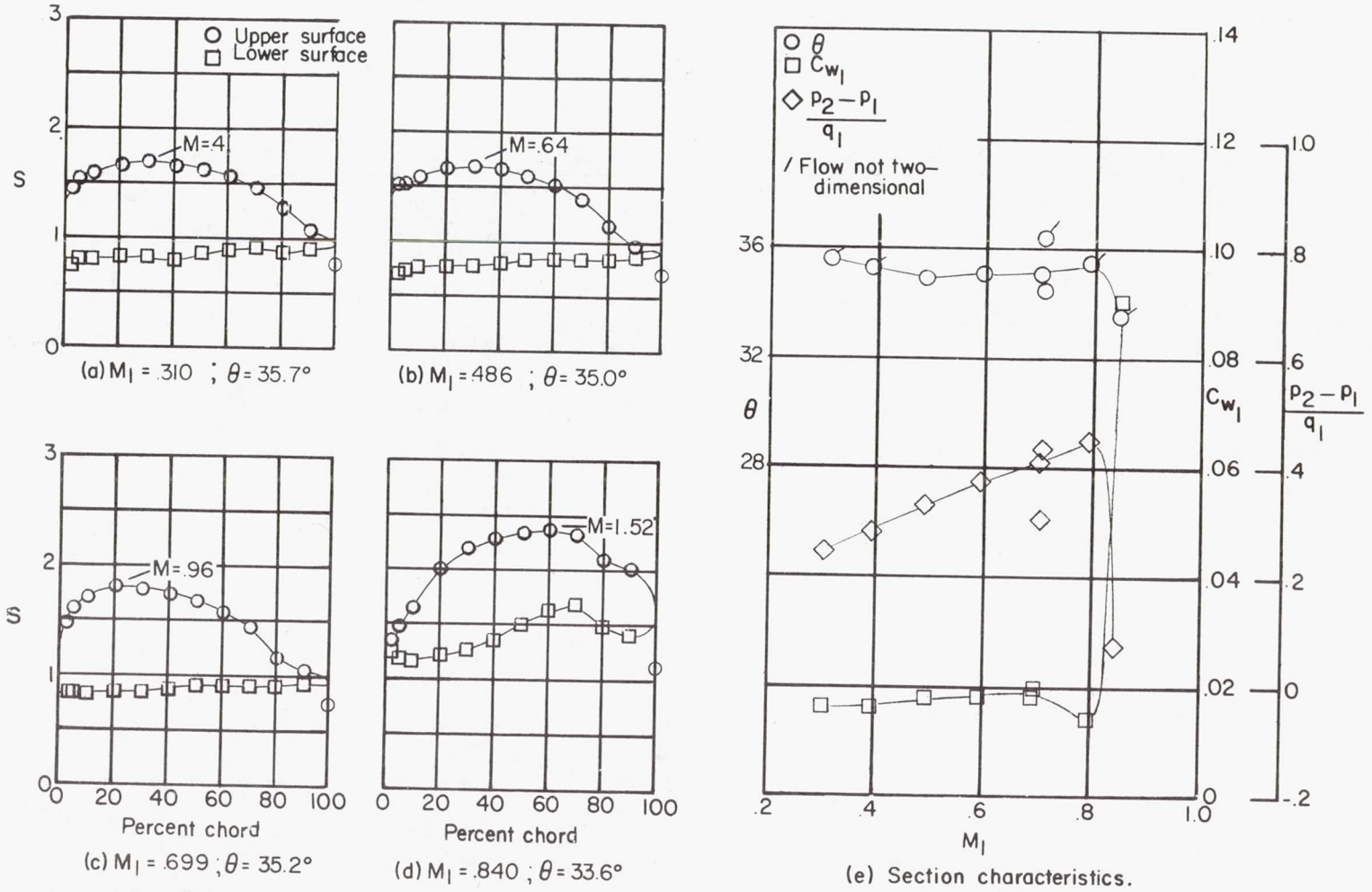


Figure 62.- Blade-surface pressure distributions and section characteristics for the cascade combination $\beta_1 = 35°$, $\sigma = 1.5$, $\alpha = 24.2°$, and circular-arc configuration I.

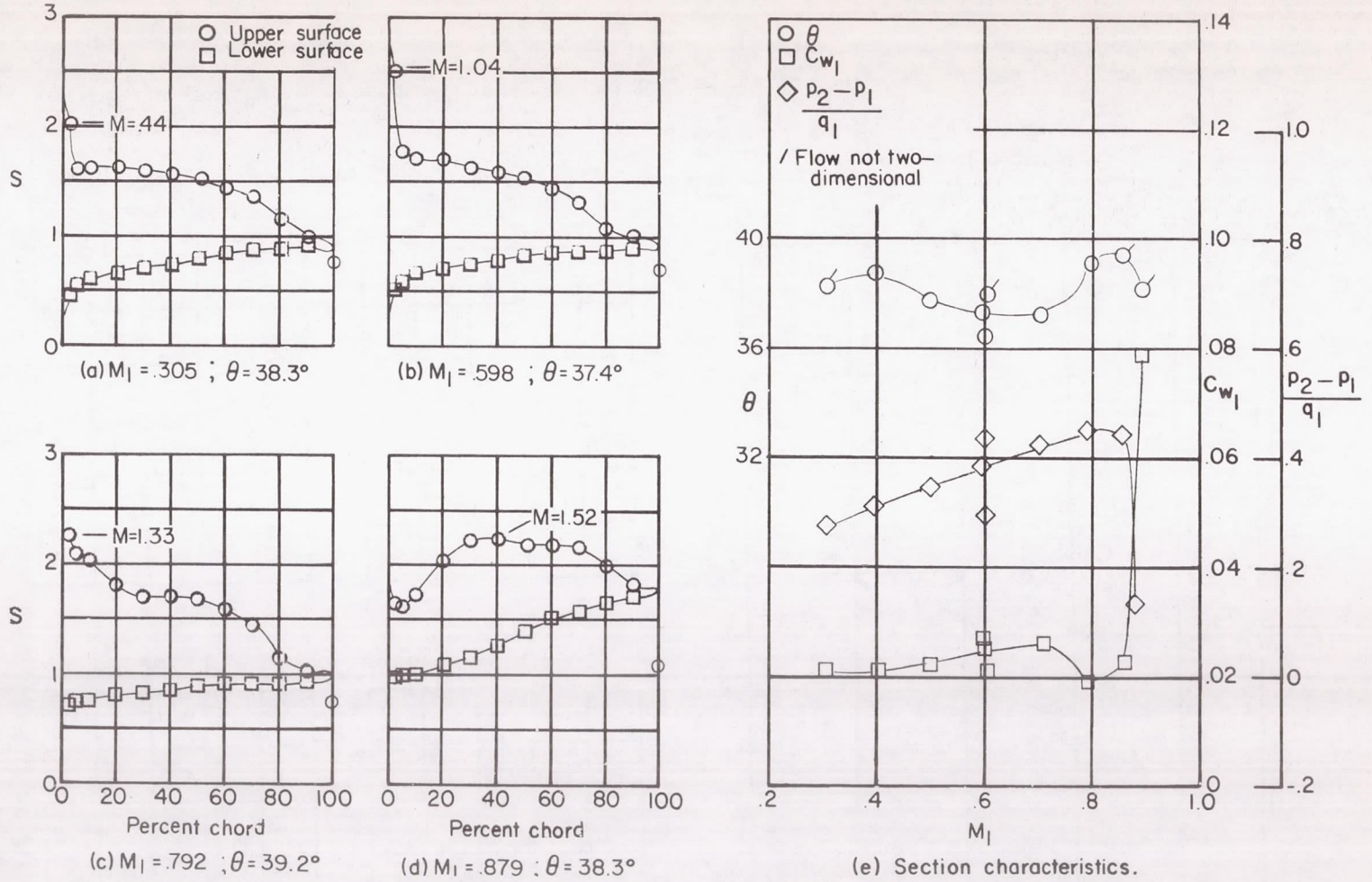


Figure 63.- Blade-surface pressure distributions and section characteristics for the cascade combination $\beta_1 = 35°$, $\sigma = 1.5$, $\alpha = 27.2°$, and circular-arc configuration I.

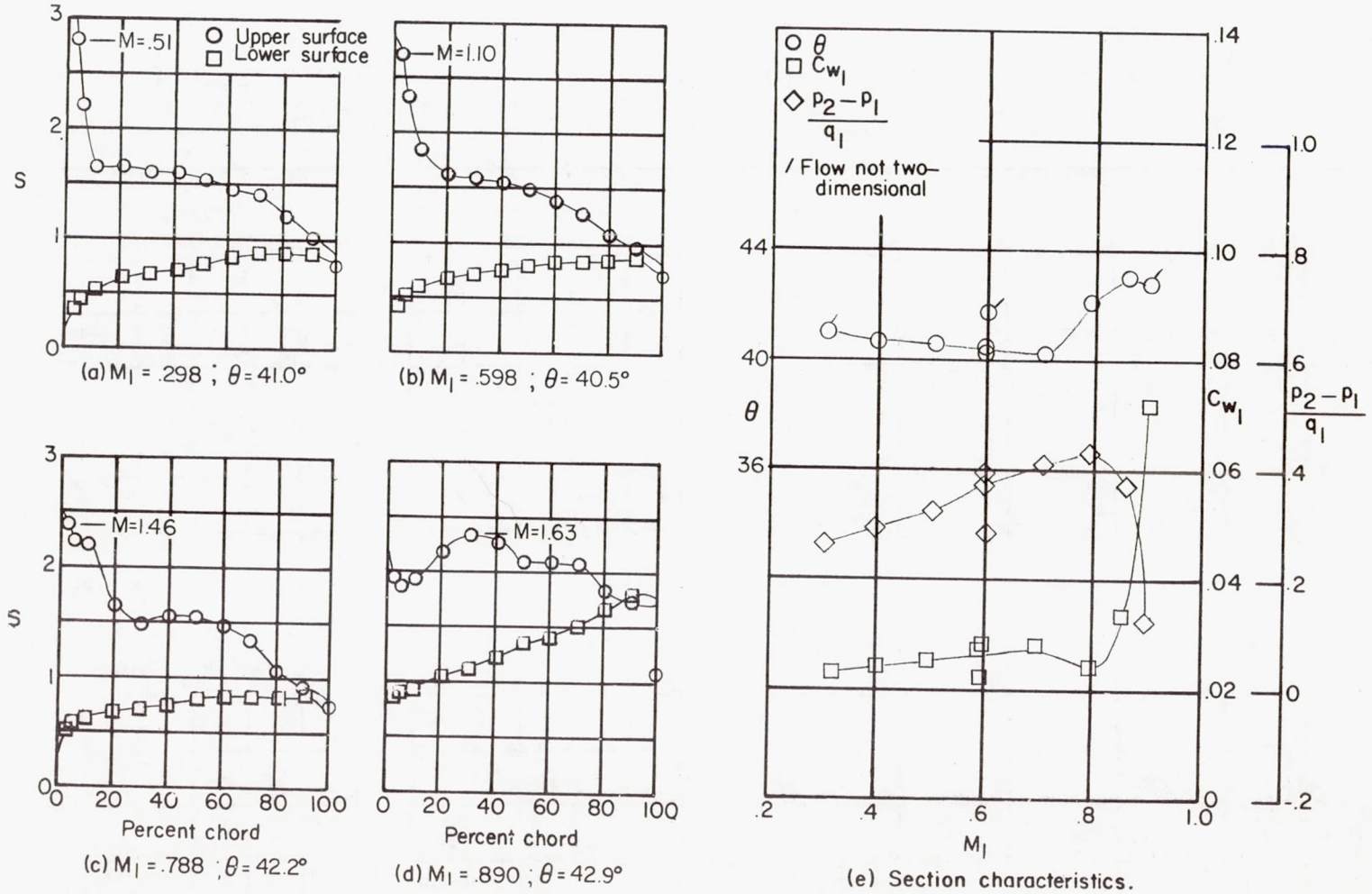


Figure 64.- Blade-surface pressure distributions and section characteristics for the cascade combination $\beta_1 = 35°$, $\sigma = 1.5$, $\alpha = 30.2°$, and circular-arc configuration I.

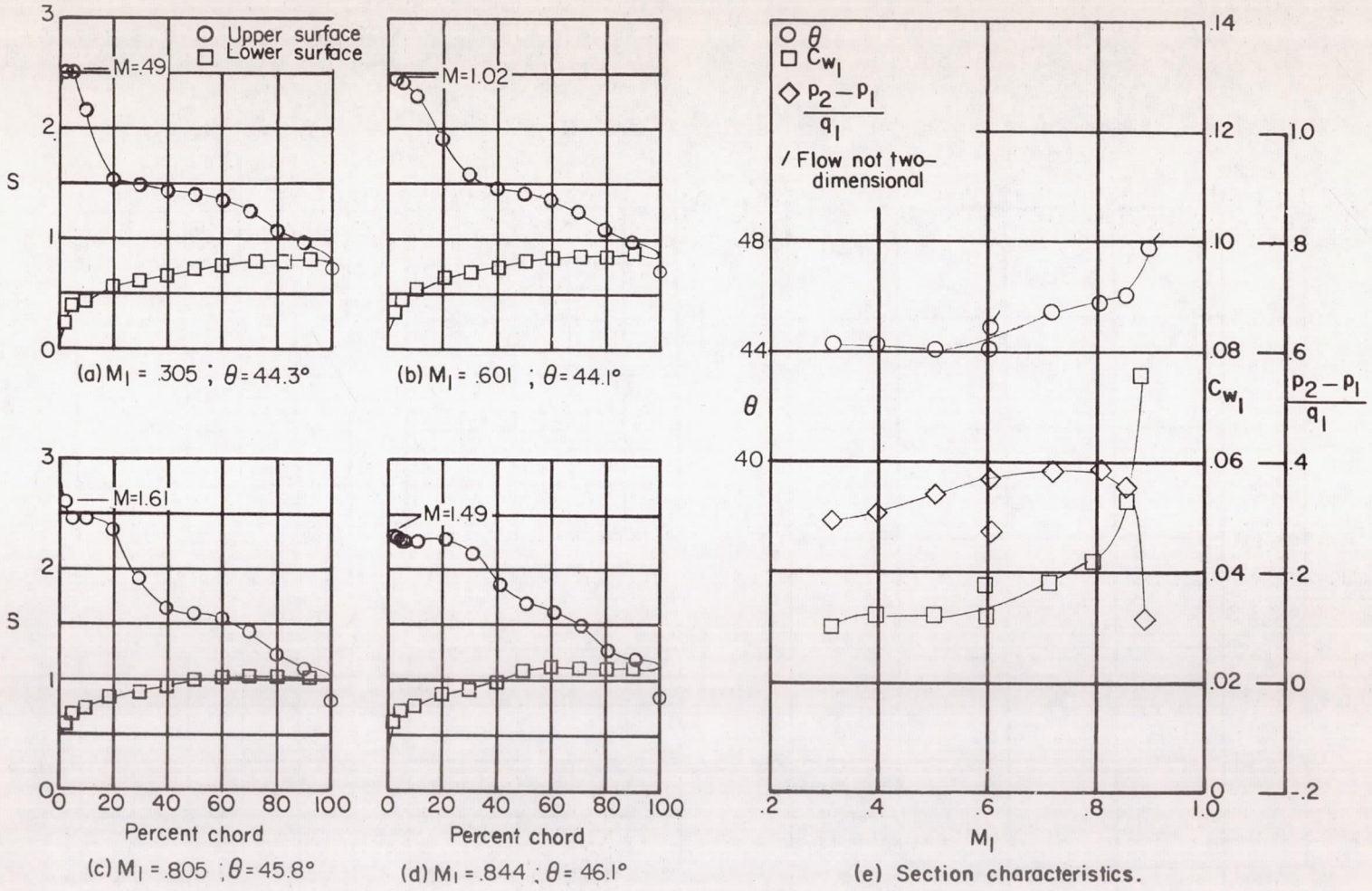


Figure 65.- Blade-surface pressure distributions and section characteristics for the cascade combination $\beta_1 = 35^\circ$, $\sigma = 1.5$, $\alpha = 33.2^\circ$, and circular-arc configuration I.

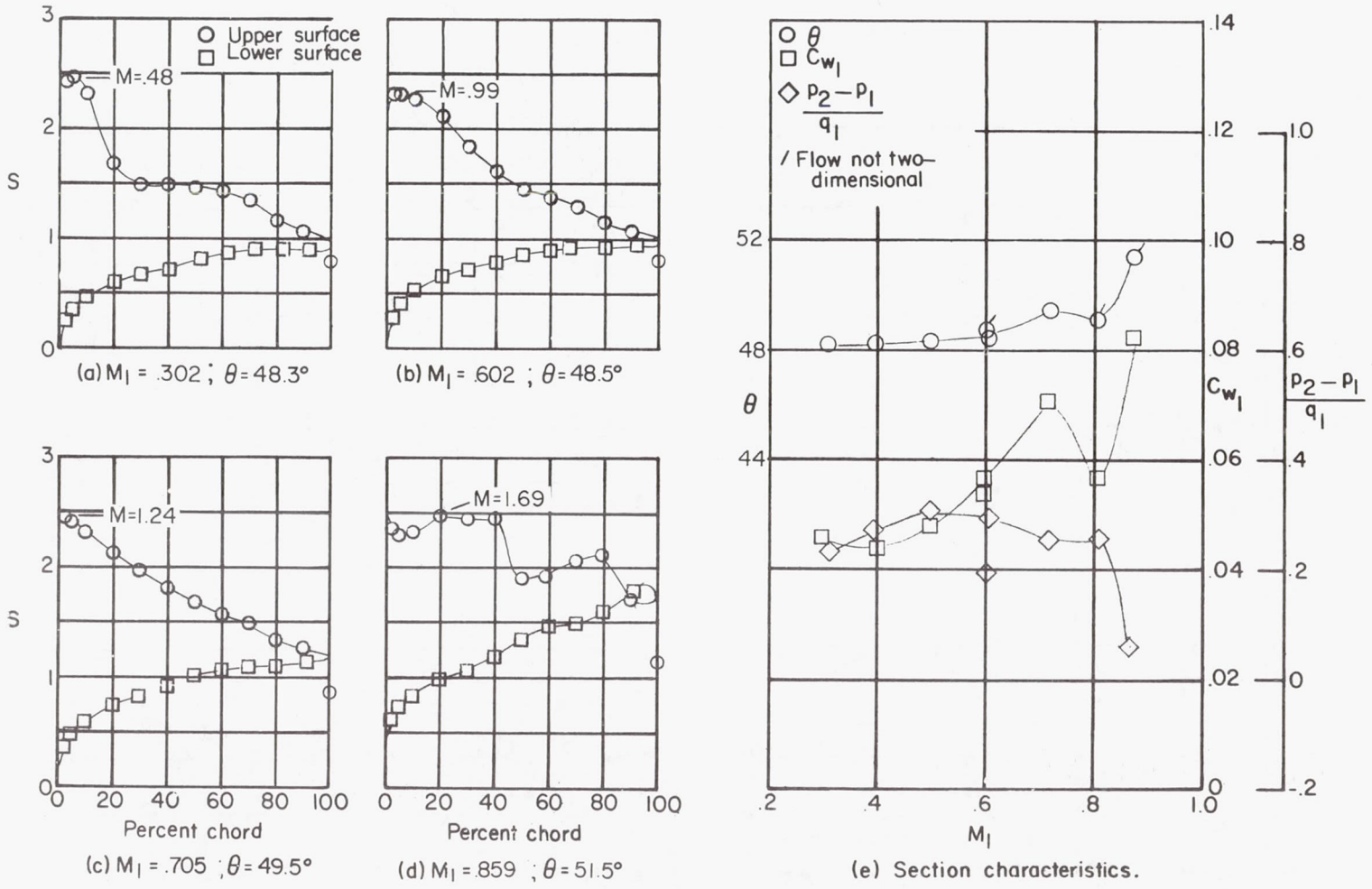


Figure 66.- Blade-surface pressure distributions and section characteristics for the cascade combination $\beta_1 = 35^\circ$, $\sigma = 1.5$, $\alpha = 36.2^\circ$, and circular-arc configuration I.

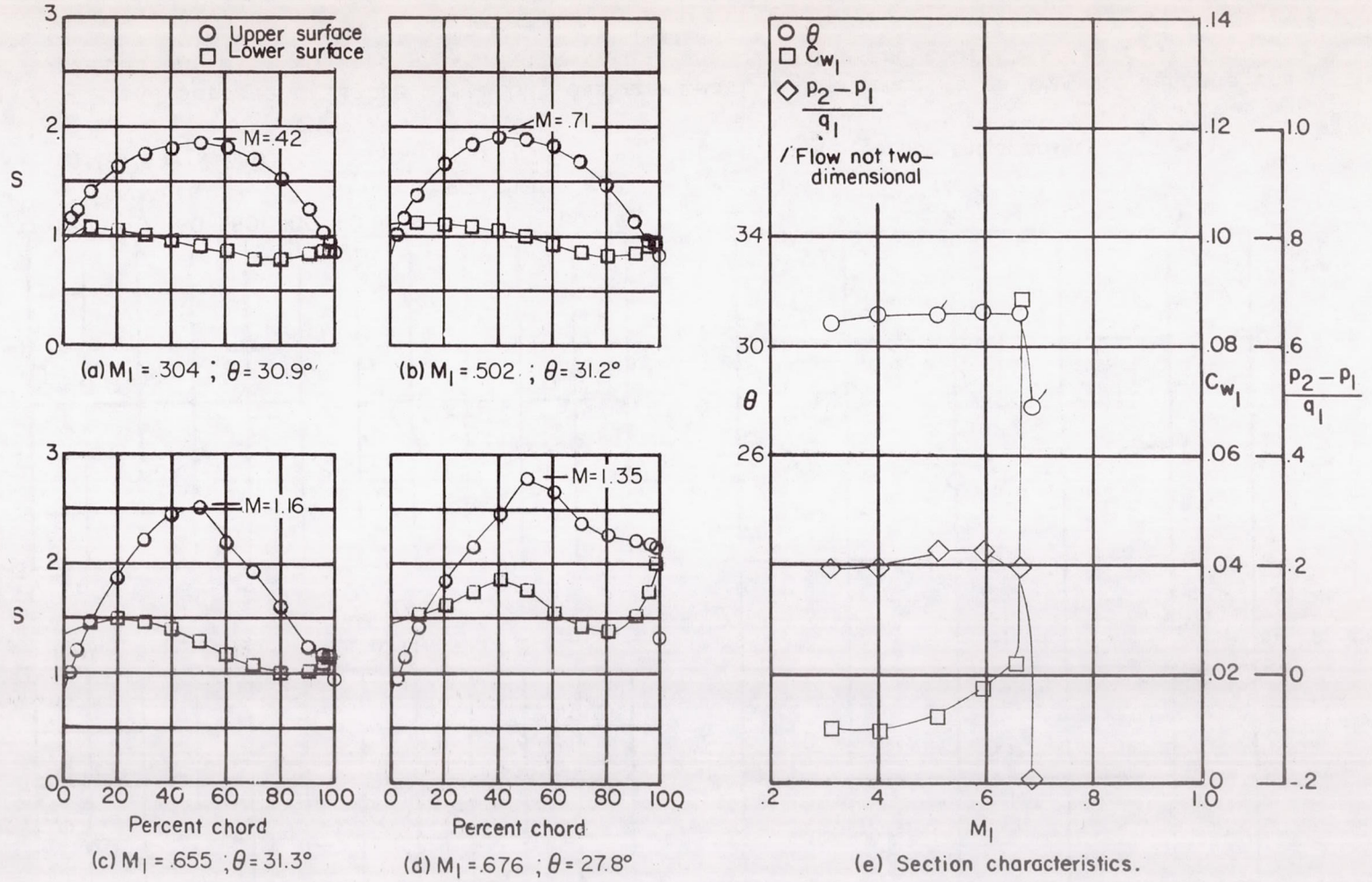


Figure 67.- Blade-surface pressure distributions and section characteristics for the cascade combination $\beta_1 = 25°$, $\sigma = 1.5$, $\alpha = 14.8°$, and circular-arc configuration II.

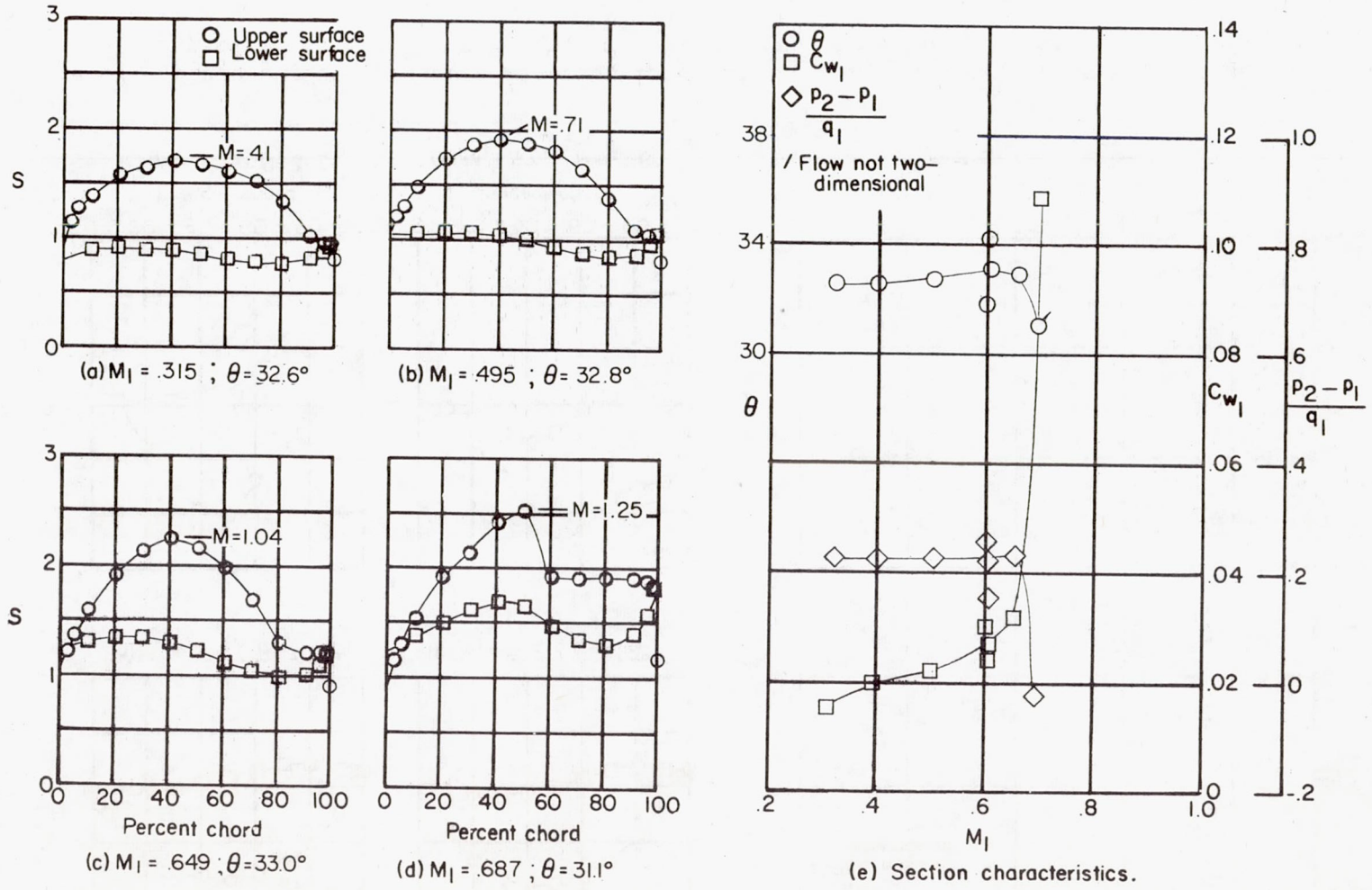


Figure 68.- Blade-surface pressure distributions and section characteristics for the cascade combination $\beta_1 = 25^\circ$, $\sigma = 1.5$, $\alpha = 17.8^\circ$, and circular-arc configuration II.

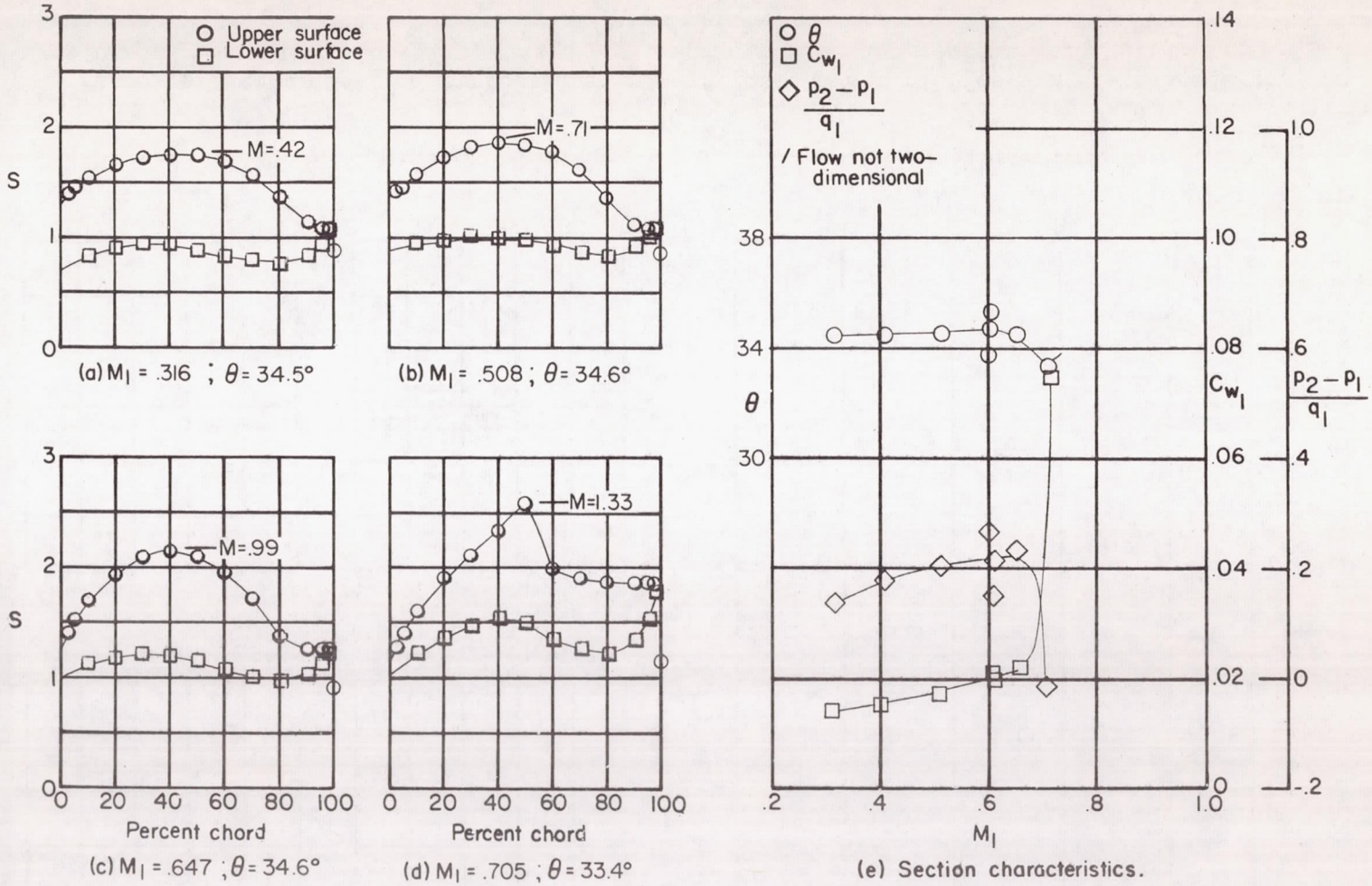


Figure 69.- Blade-surface pressure distributions and section characteristics for the cascade combination $\beta_1 = 25°$, $\sigma = 1.5$, $\alpha = 20.8°$, and circular-arc configuration II.

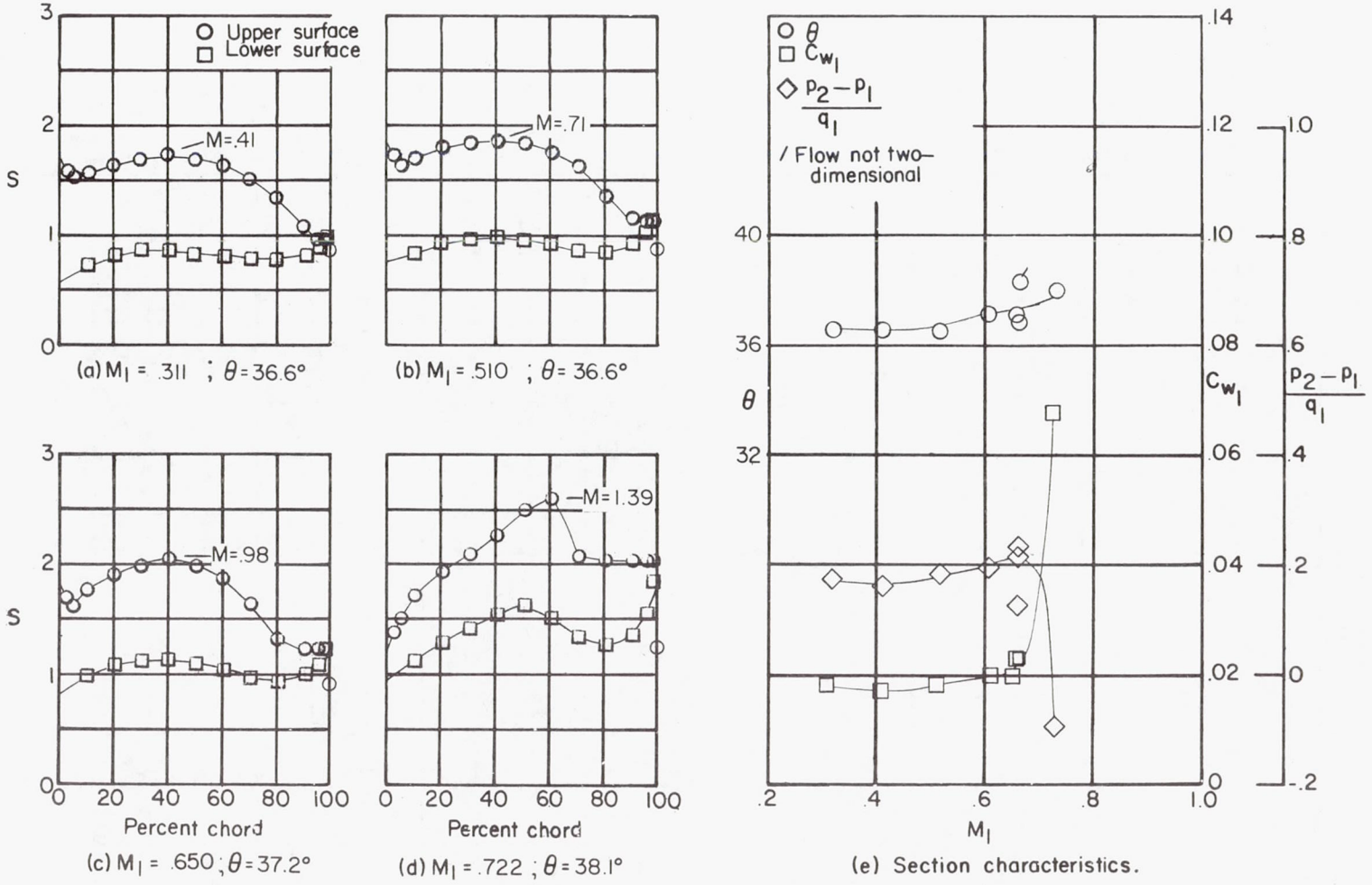


Figure 70.- Blade-surface pressure distributions and section characteristics for the cascade combination $\beta_1 = 25^\circ$, $\sigma = 1.5$, $\alpha = 23.8^\circ$, and circular-arc configuration II.

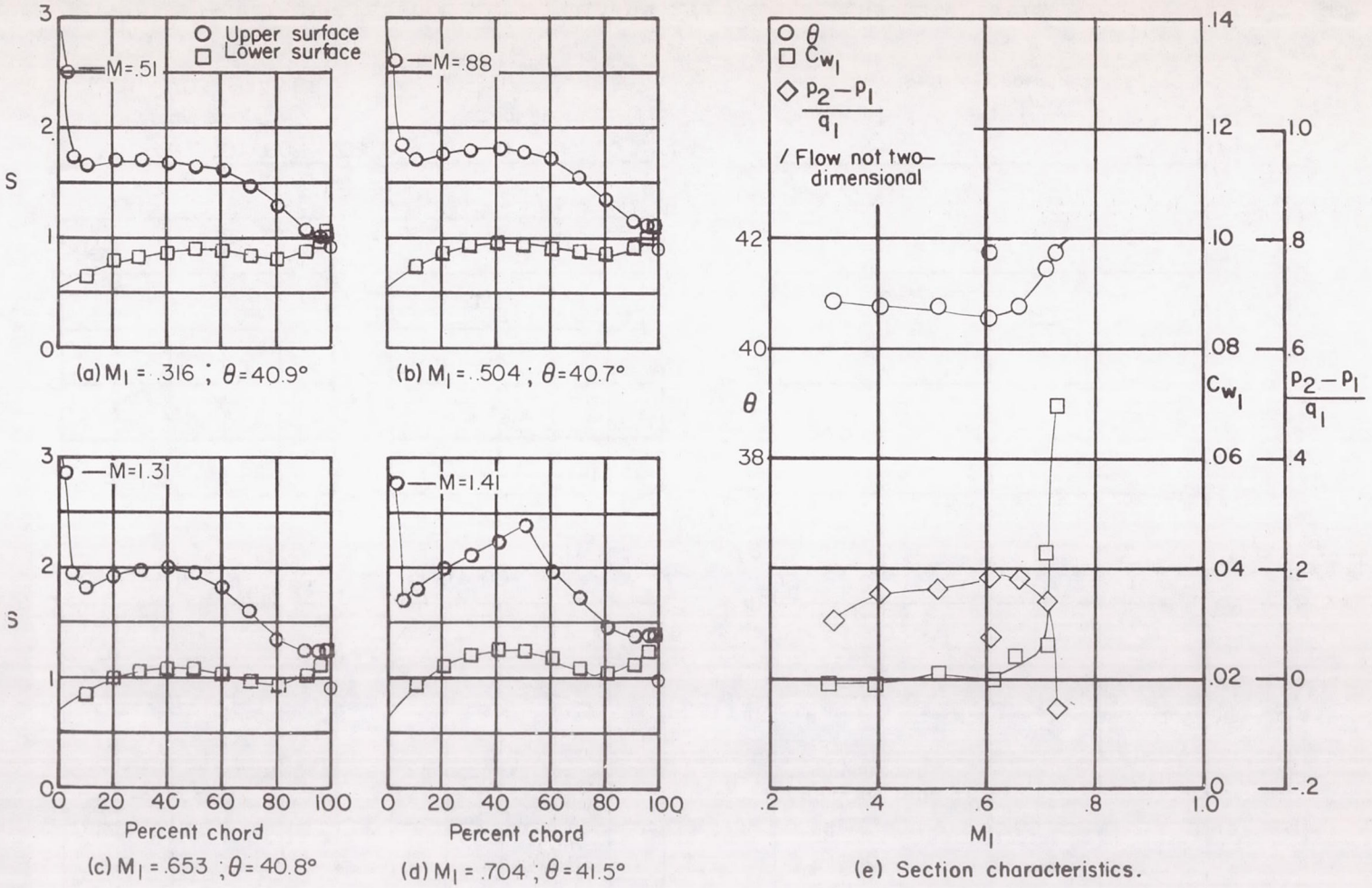


Figure 71.- Blade-surface pressure distributions and section characteristics for the cascade combination $\beta_1 = 25°$, $\sigma = 1.5$, $\alpha = 26.8°$, and circular-arc configuration II.

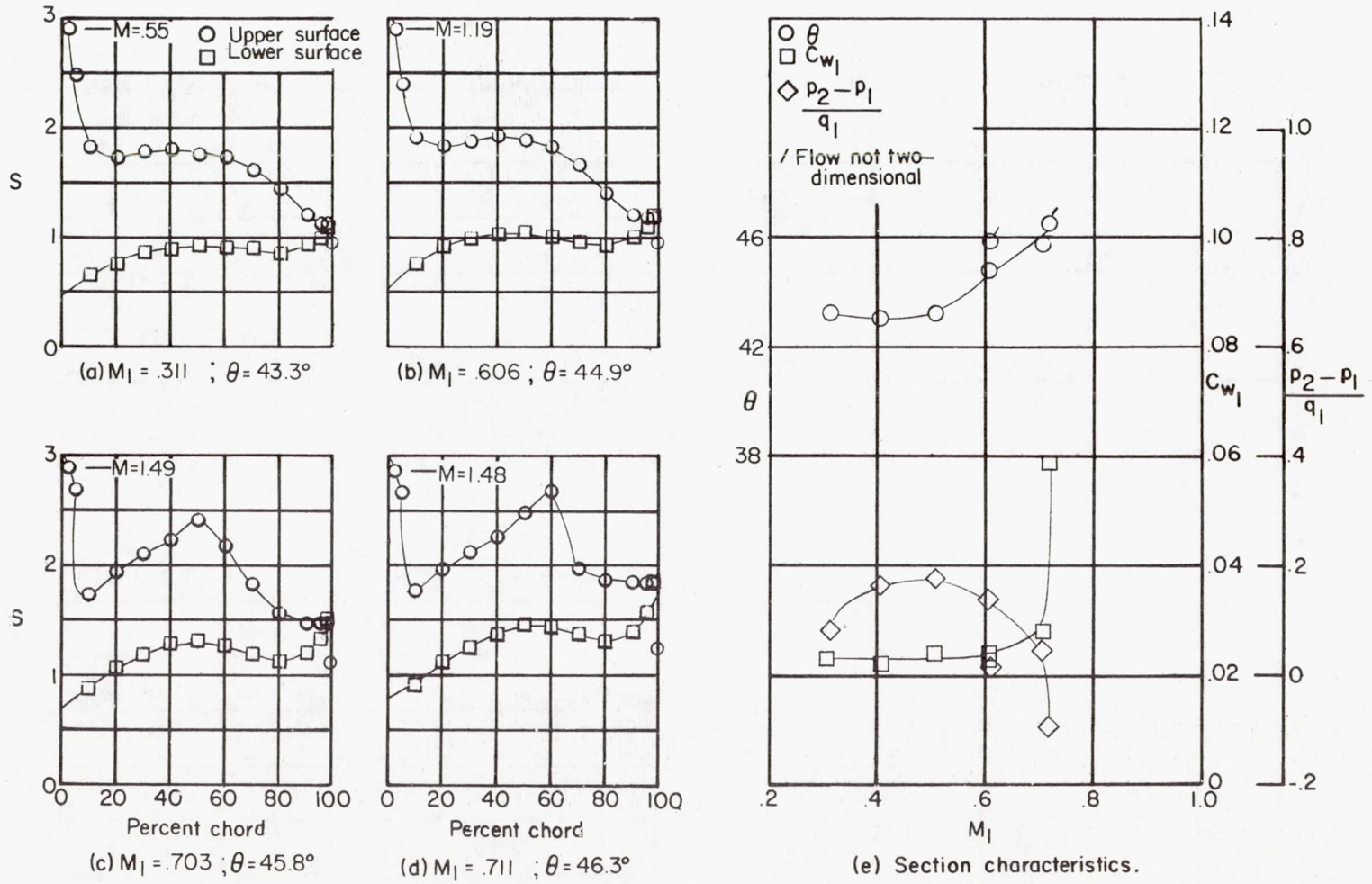


Figure 72.- Blade-surface pressure distributions and section characteristics for the cascade combination $\beta_1 = 25°$, $\sigma = 1.5$, $\alpha = 29.8°$, and circular-arc configuration II.

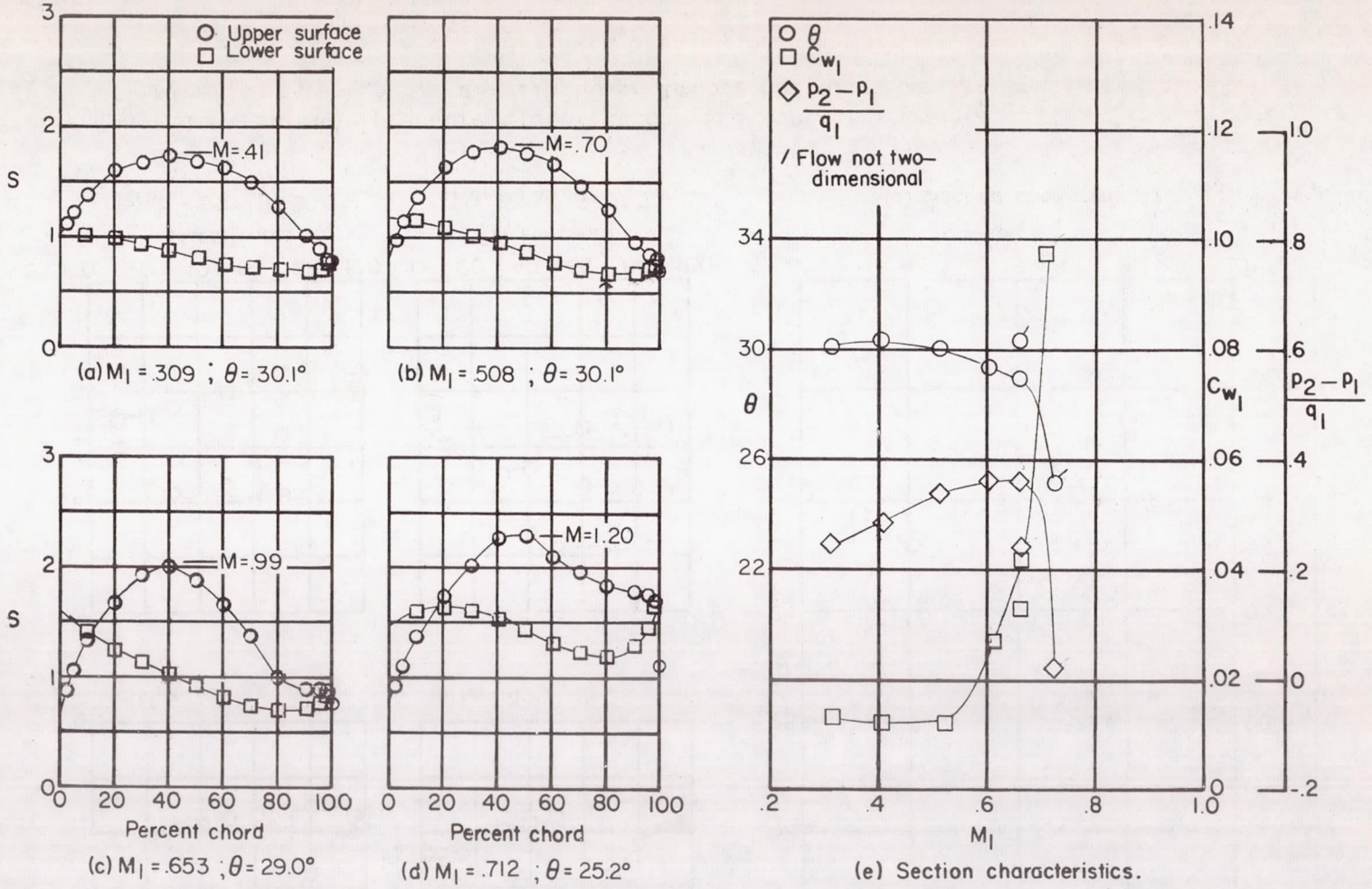


Figure 73.- Blade-surface pressure distributions and section characteristics for the cascade combination $\beta_1 = 35^\circ$, $\sigma = 1.5$, $\alpha = 15.8^\circ$, and circular-arc configuration II.

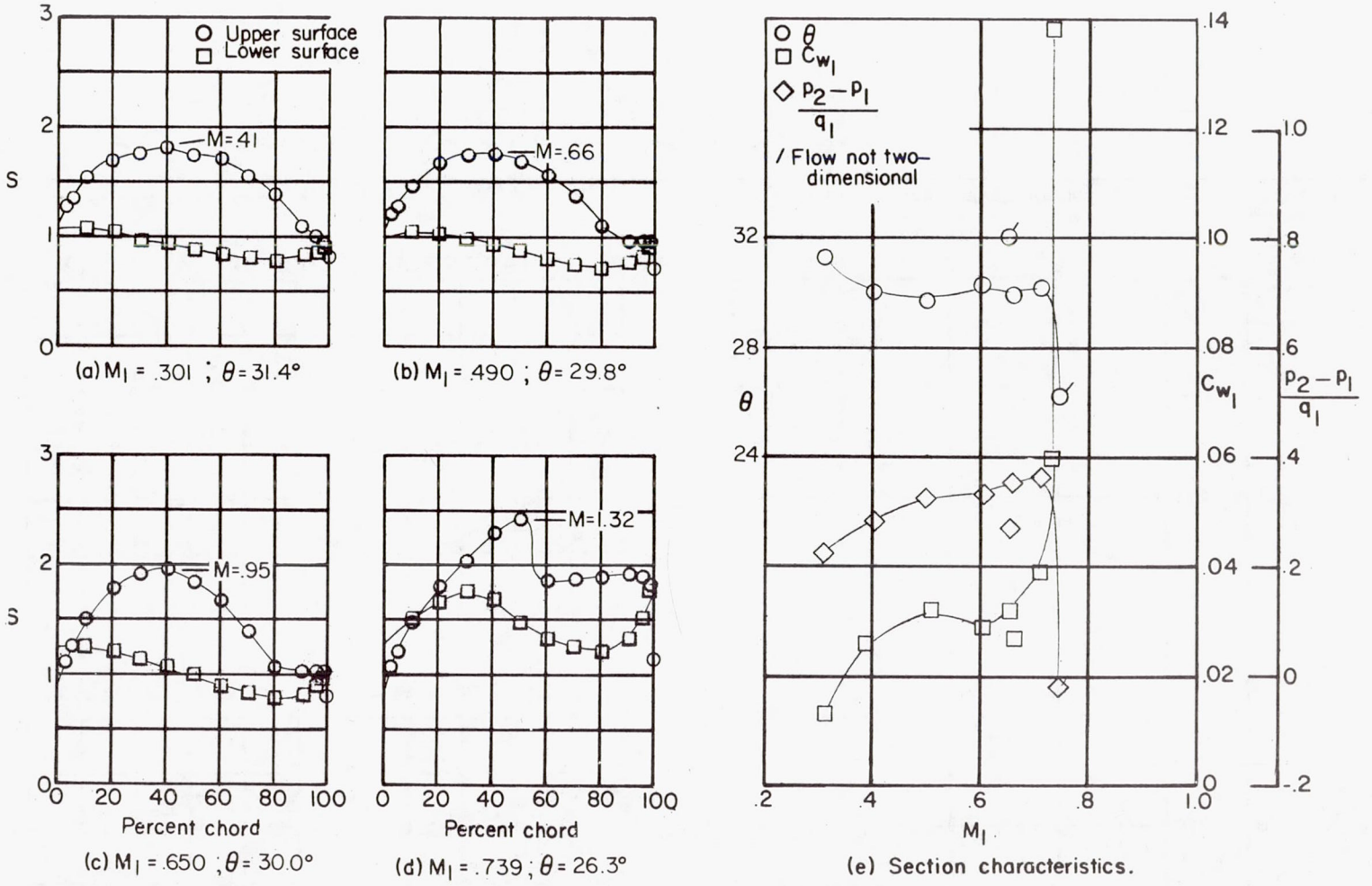


Figure 74.- Blade-surface pressure distributions and section characteristics for the cascade combination $\beta_1 = 35°$, $\sigma = 1.5$, $\alpha = 18.8°$, and circular-arc configuration II.

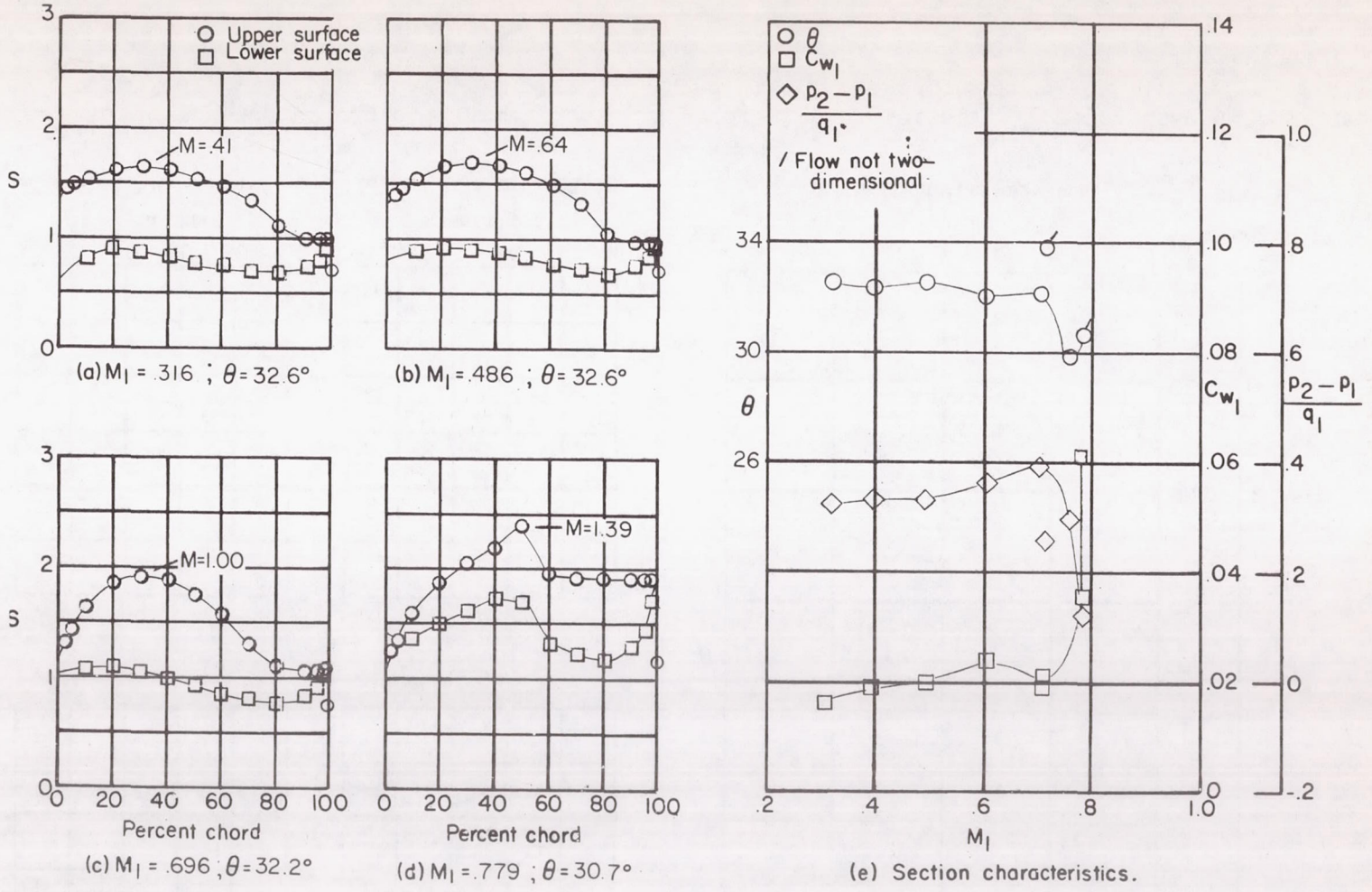


Figure 75.- Blade-surface pressure distributions and section characteristics for the cascade combination $\beta_1 = 35°$, $\sigma = 1.5$, $\alpha = 21.8°$, and circular-arc configuration II.

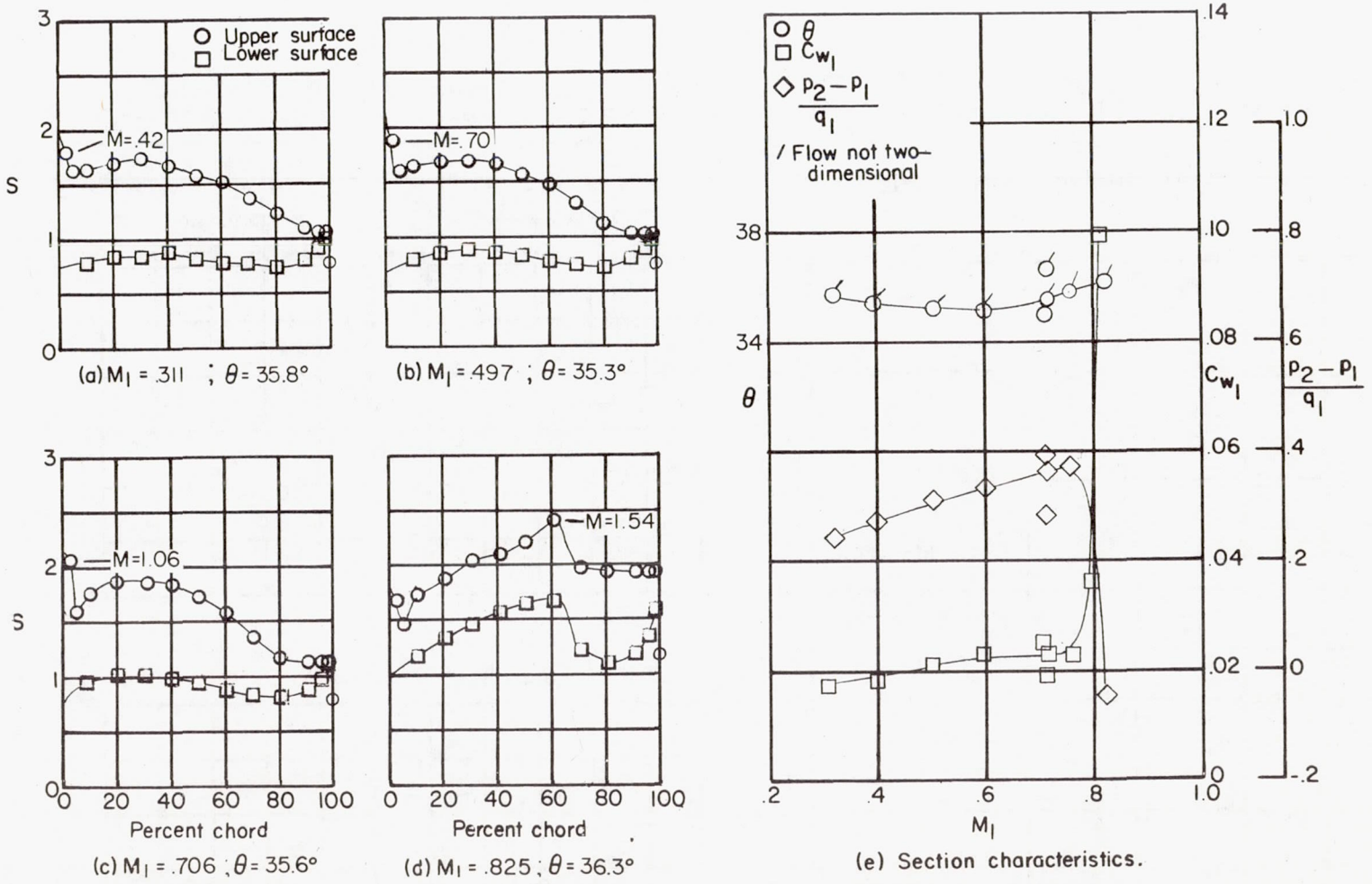


Figure 76.- Blade-surface pressure distributions and section characteristics for the cascade combination $\beta_1 = 35^\circ$, $\sigma = 1.5$, $\alpha = 24.8^\circ$, and circular-arc configuration II.

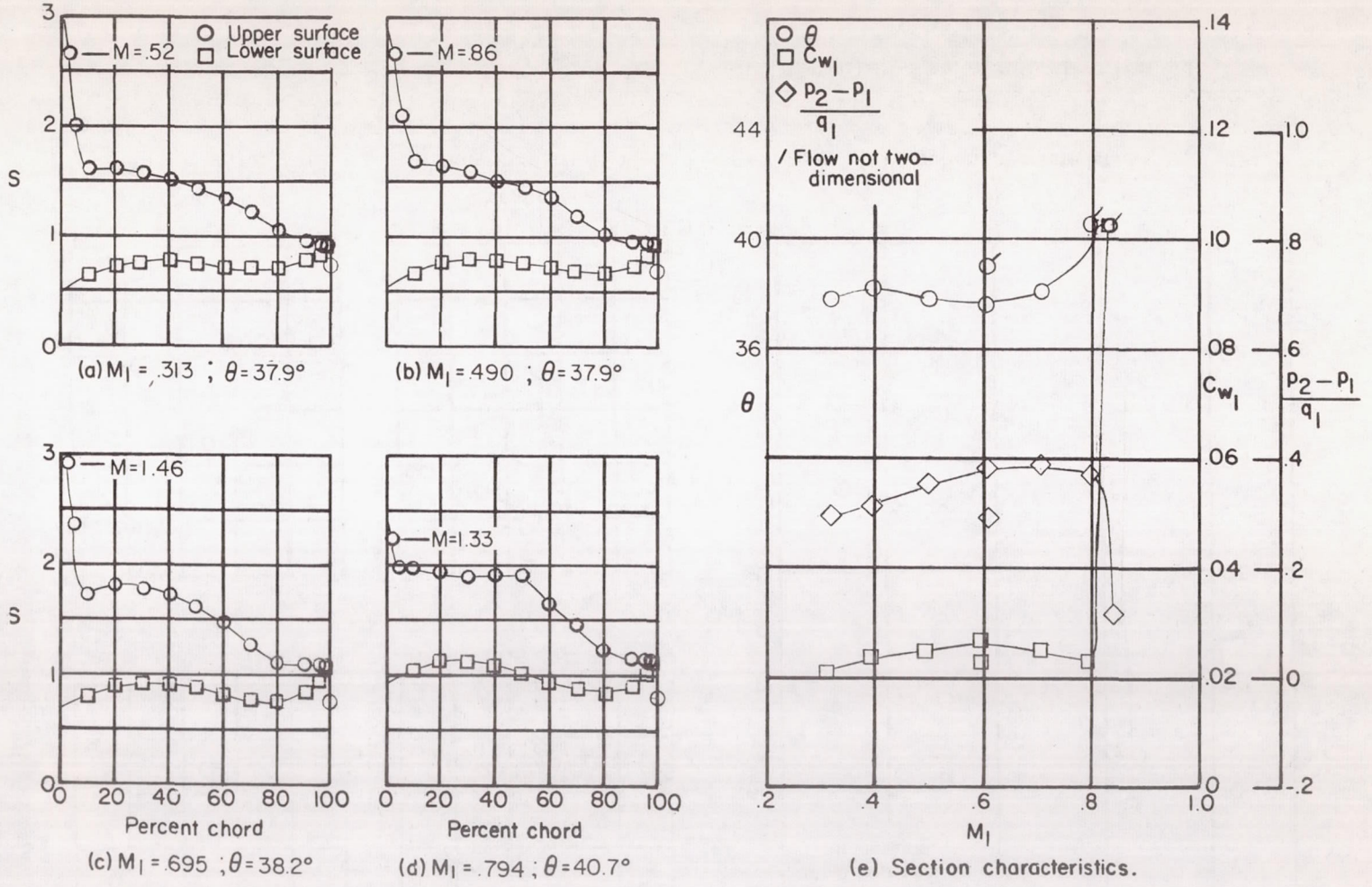


Figure 77.- Blade-surface pressure distributions and section characteristics for the cascade combination $\beta_1 = 35^\circ$, $\sigma = 1.5$, $\alpha = 27.8^\circ$, and circular-arc configuration II.

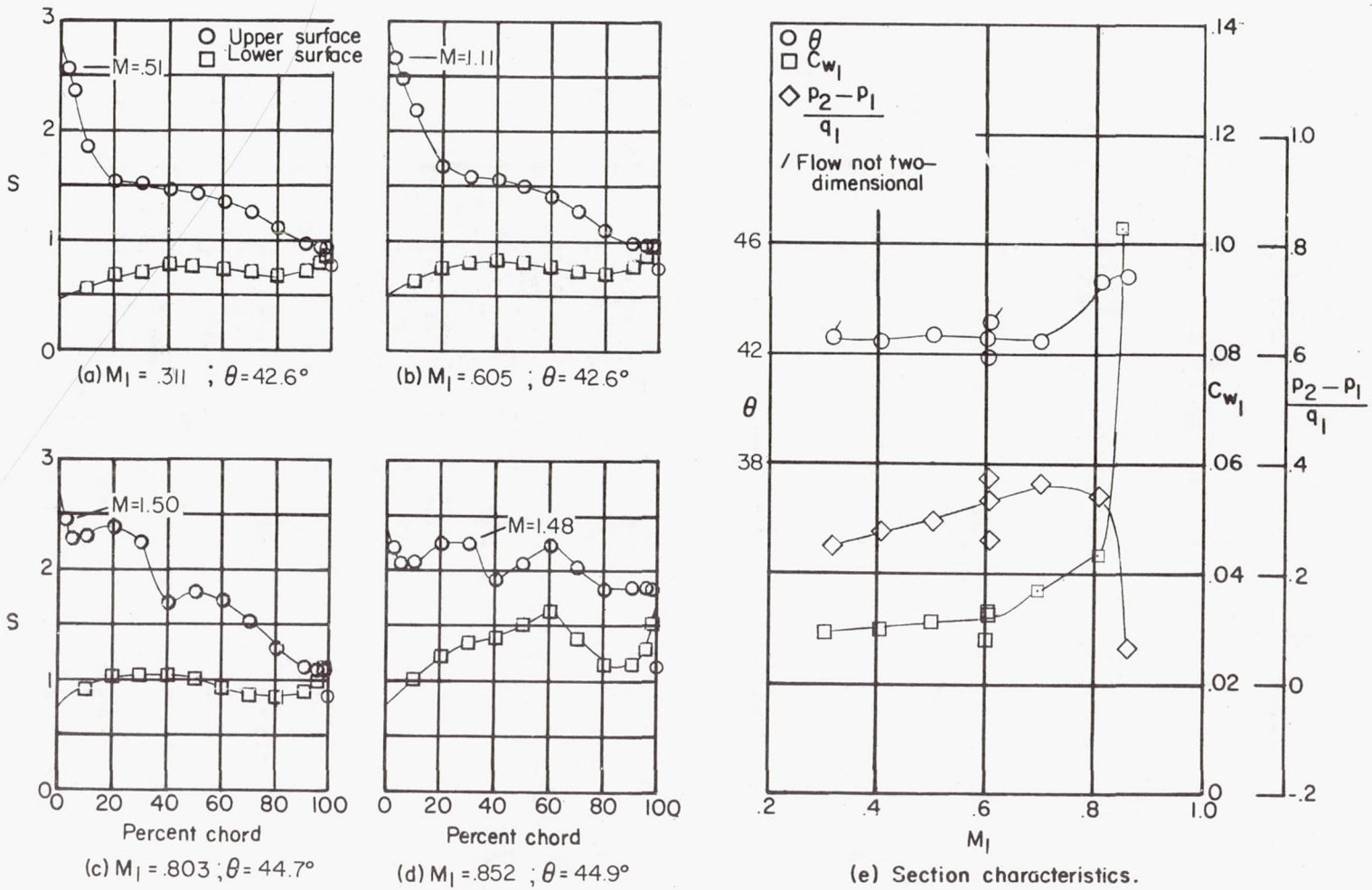


Figure 78.- Blade-surface pressure distributions and section characteristics for the cascade combination $\beta_1 = 35°$, $\sigma = 1.5$, $\alpha = 30.8°$, and circular-arc configuration II.

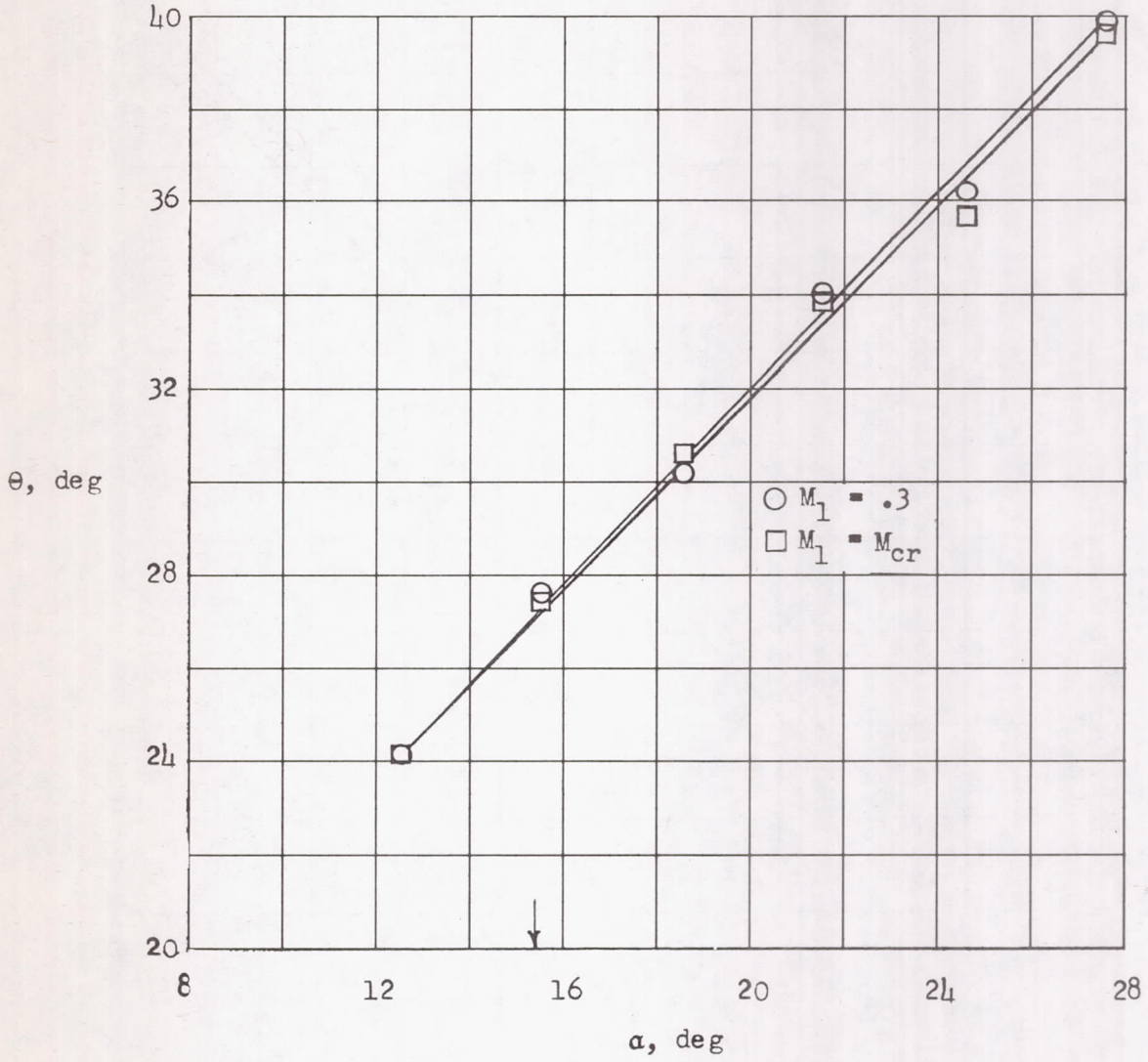


Figure 79.- Comparison of turning angles at high and low speeds for NACA 65-($12A_{10}$)10 blade section at $\beta_1 = 25^\circ$ and $\sigma = 1.5$. Arrow shows low-speed design angle of attack.

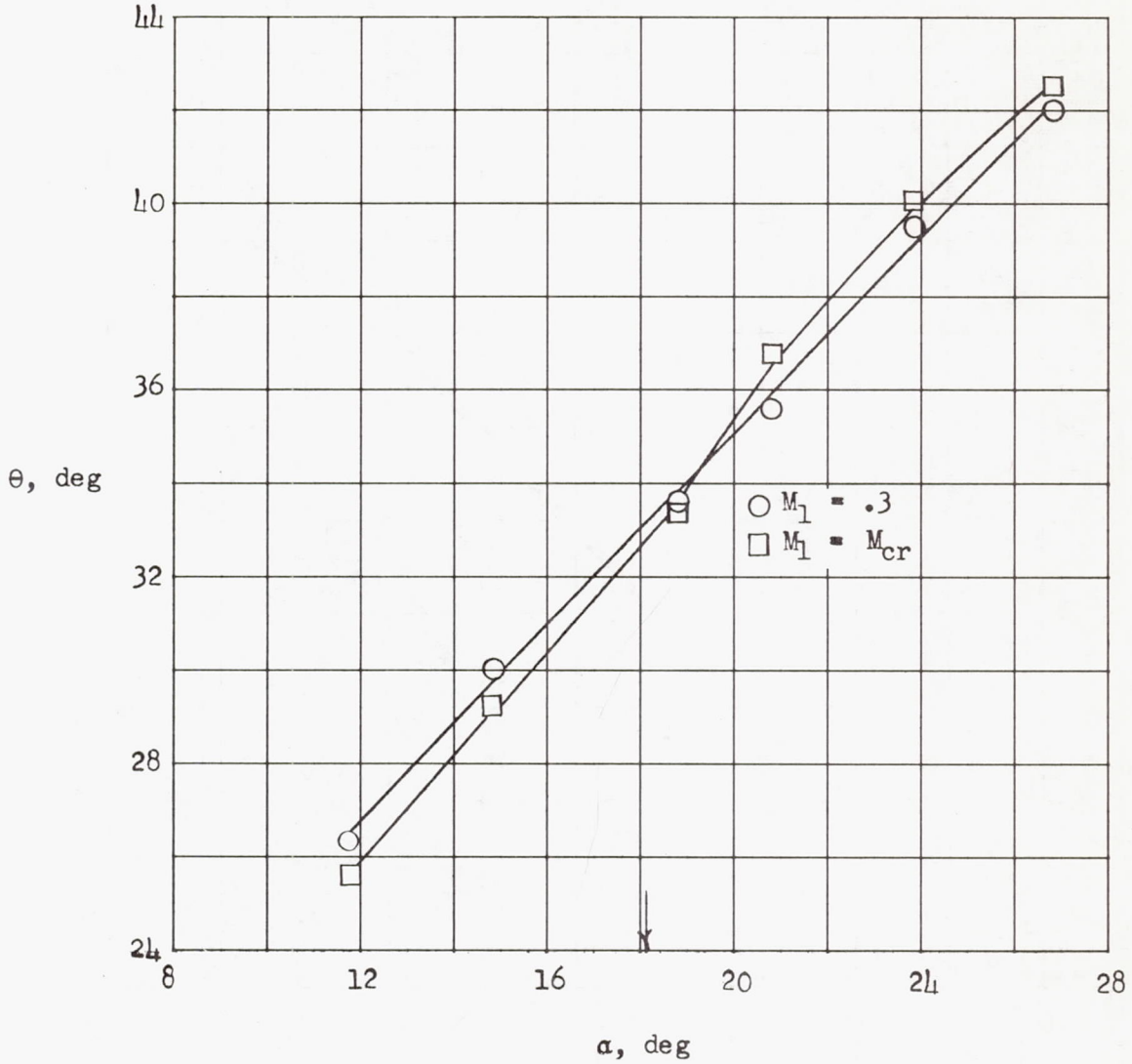


Figure 80.- Comparison of turning angles at high and low speeds for NACA 65-($15A_{10}$)10 blade section at $\beta_1 = 25^\circ$ and $\sigma = 1.5$. Arrow shows low-speed design angle of attack.

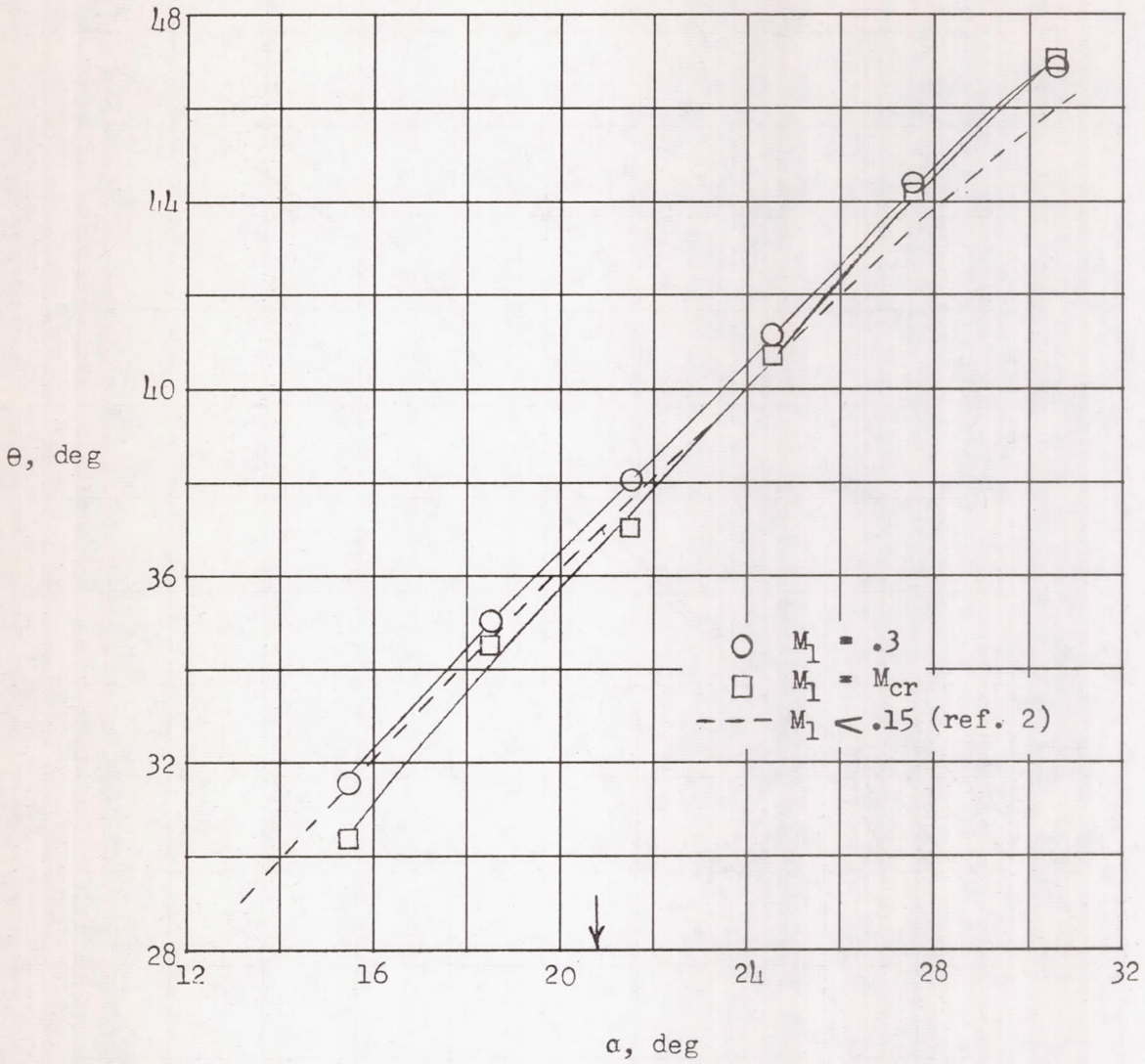


Figure 81.- Comparison of turning angles at high and low speeds for NACA 65-($18A_{10}$)10 blade section at $\beta_1 = 35^\circ$ and $\sigma = 1.5$. Arrow shows low-speed design angle of attack.

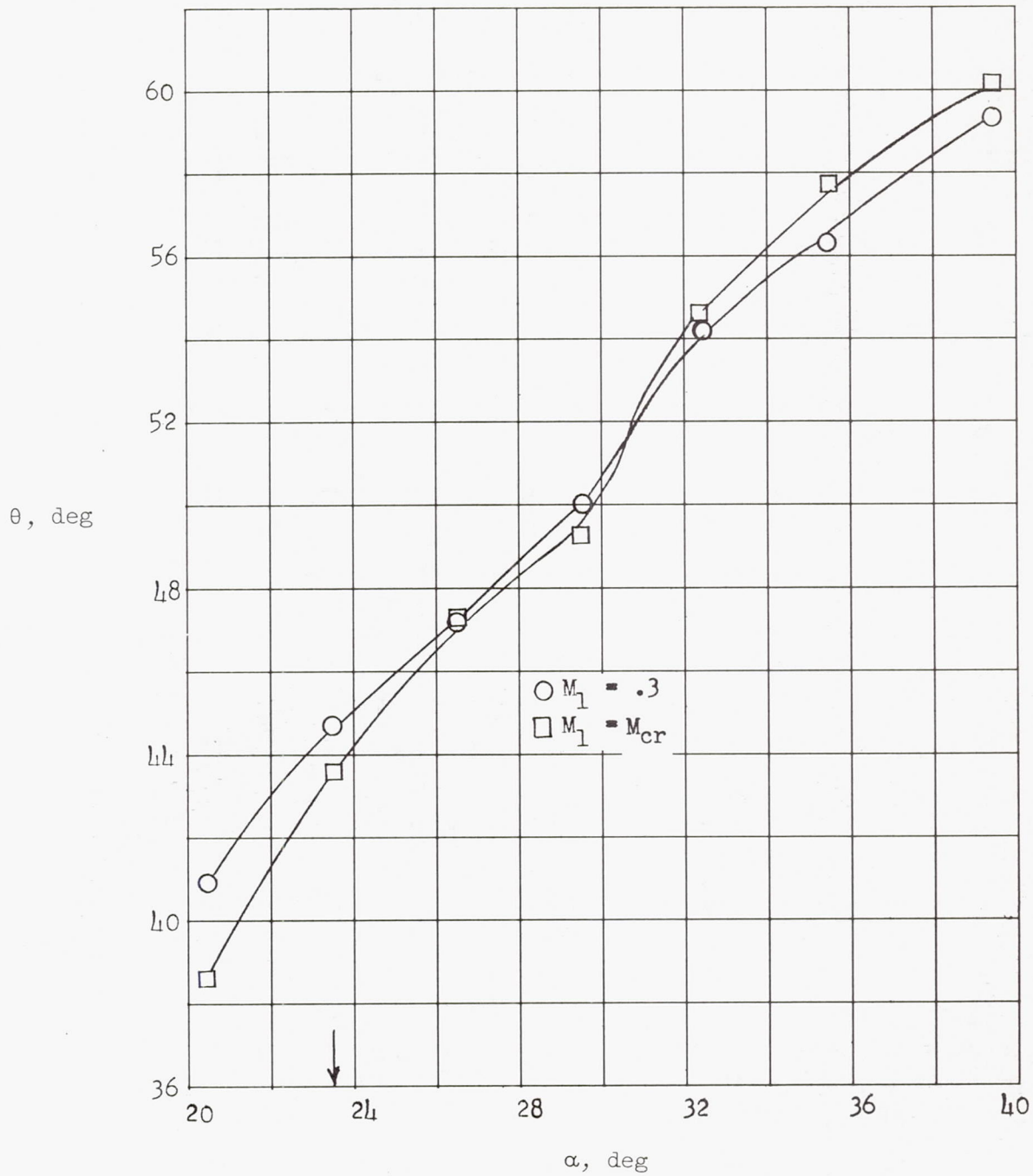


Figure 82.- Comparison of turning angles at high and low speeds for NACA 65-($21A_{10}$)10 blade section at $\beta_1 = 35^\circ$ and $\sigma = 1.5$. Arrow shows low-speed design angle of attack.

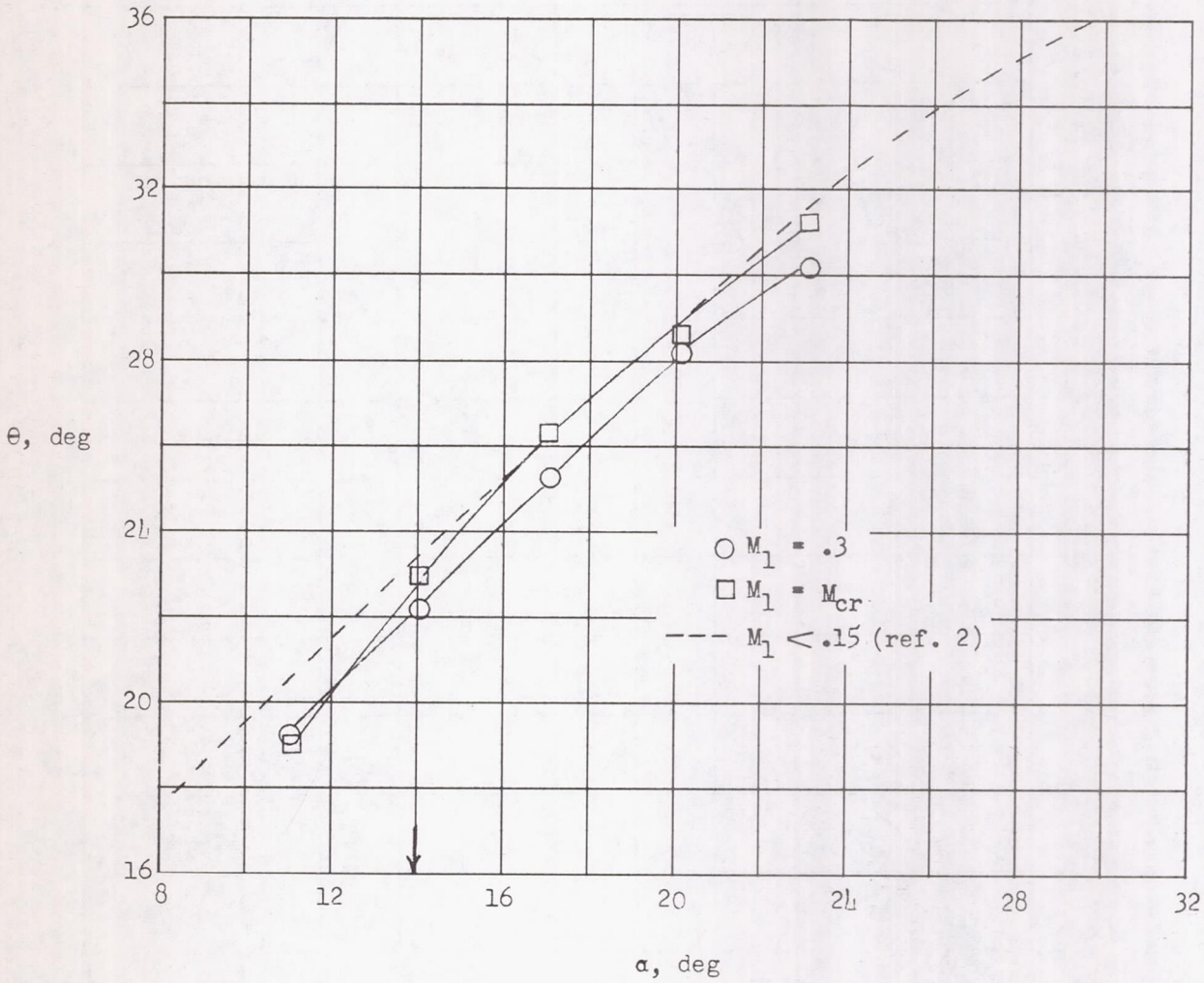


Figure 83.- Comparison of turning angles at high and low speeds for NACA 65-($12A_{10}$)10 blade section at $\beta_1 = 35^\circ$ and $\sigma = 1.25$. Arrow shows low-speed design angle of attack.

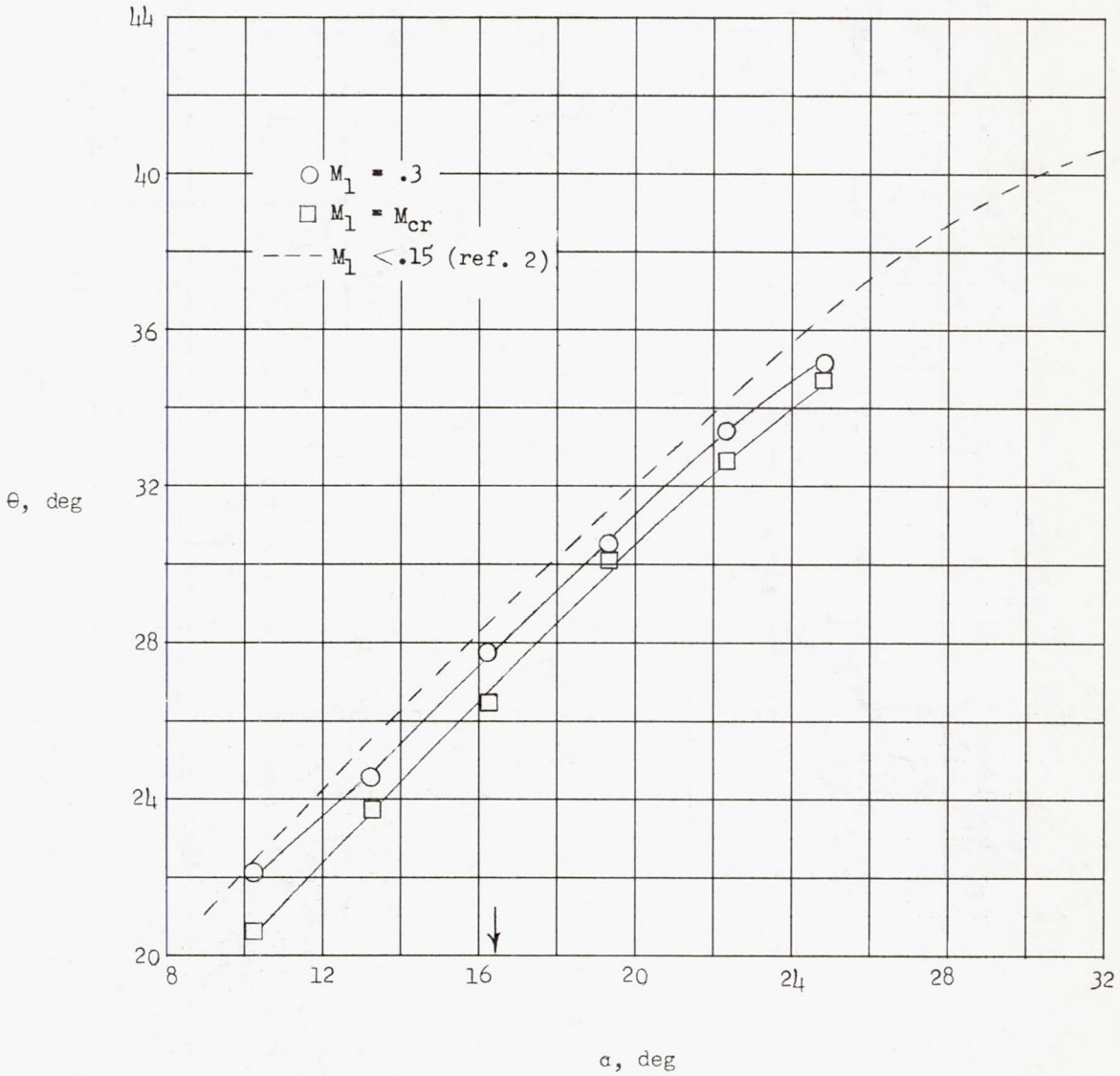


Figure 84.- Comparison of turning angles at high and low speeds for NACA 65-($15A_{10}$)10 blade section at $\beta_1 = 35^\circ$ and $\sigma = 1.25$. Arrow shows low-speed design angle of attack.

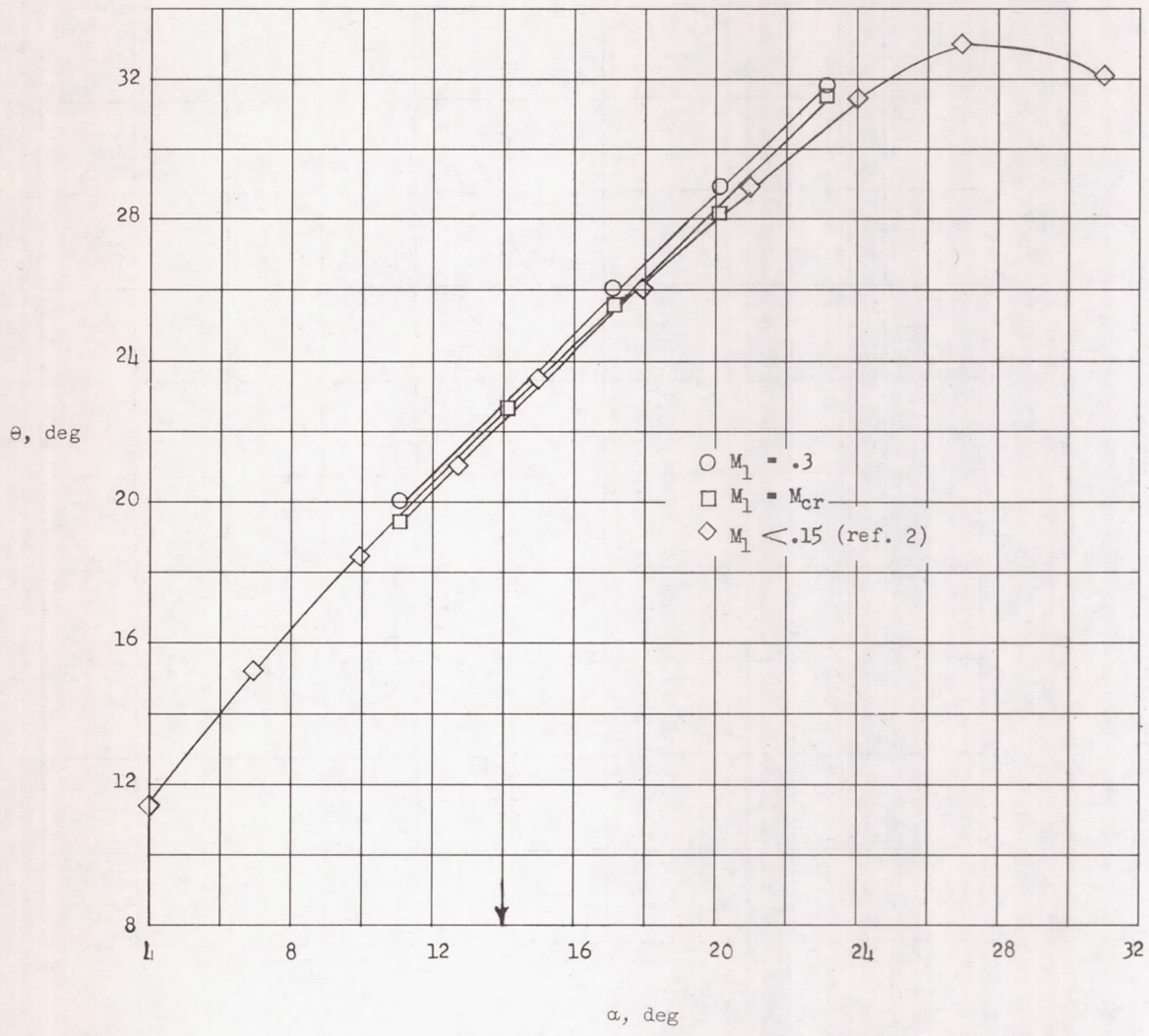


Figure 85.- Comparison of turning angles at high and low speeds for NACA 65-($12A_{10}$)10 blade section at $\beta_1 = 45^\circ$ and $\sigma = 1.25$. Arrow shows low-speed design angle of attack.

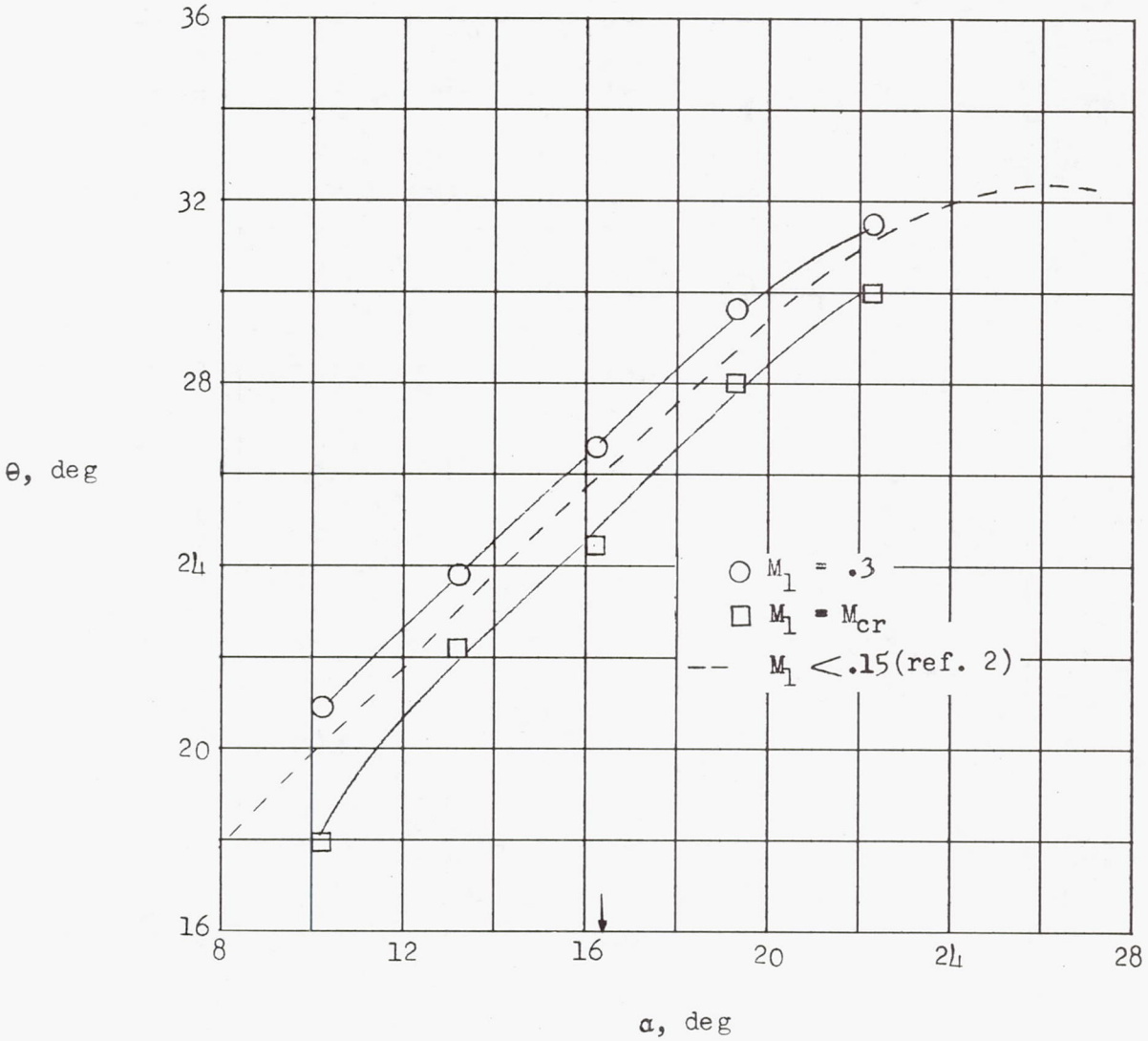


Figure 86.- Comparison of turning angles at high and low speeds for NACA 65-($15A_{10}$)10 blade section at $\beta_1 = 45^\circ$ and $\sigma = 1.25$. Arrow shows low-speed design angle of attack.

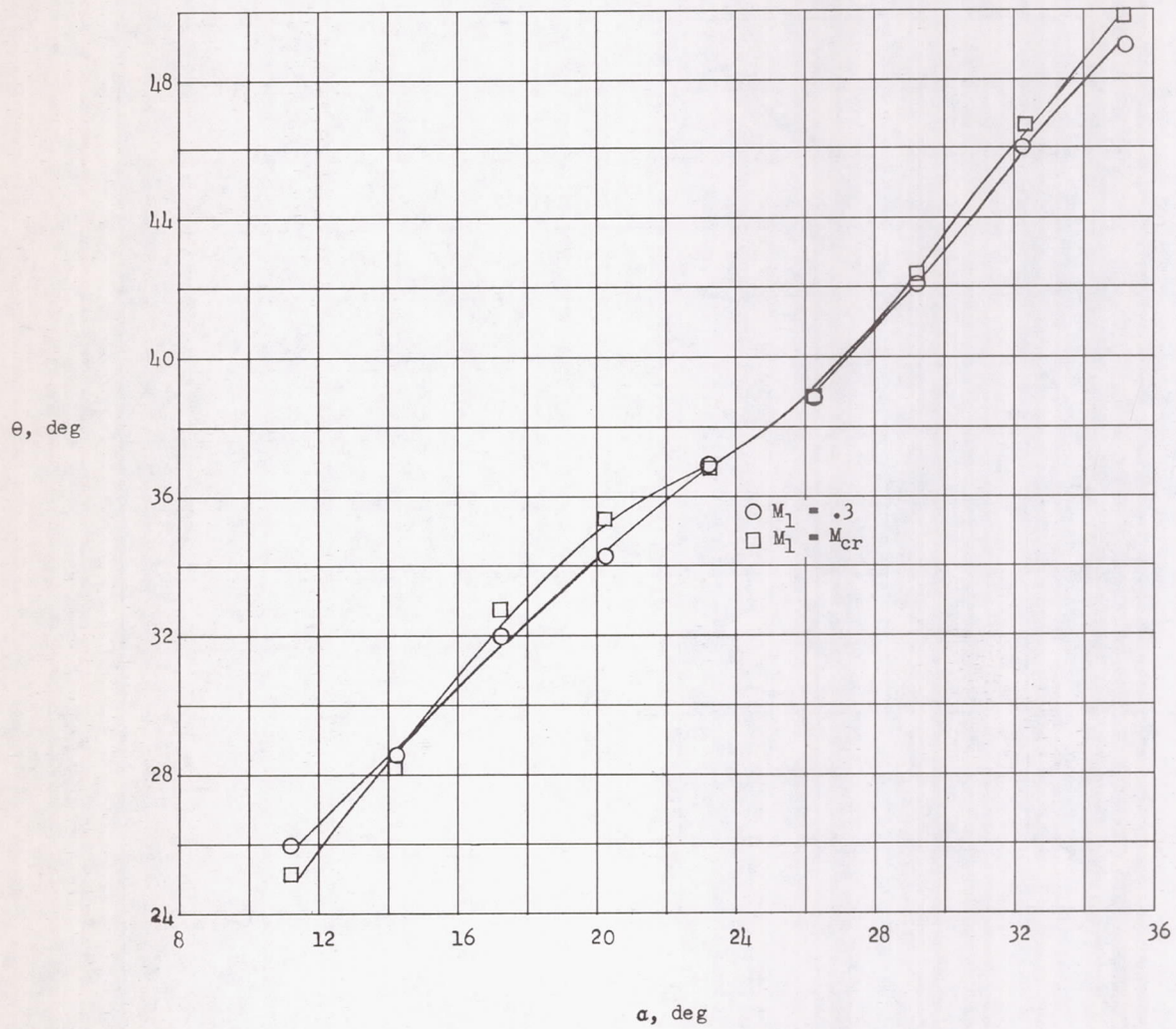


Figure 87.- Comparison of turning angles at high and low speeds for circular-arc configuration I at $\beta_1 = 25^\circ$ and $\sigma = 1.5$.

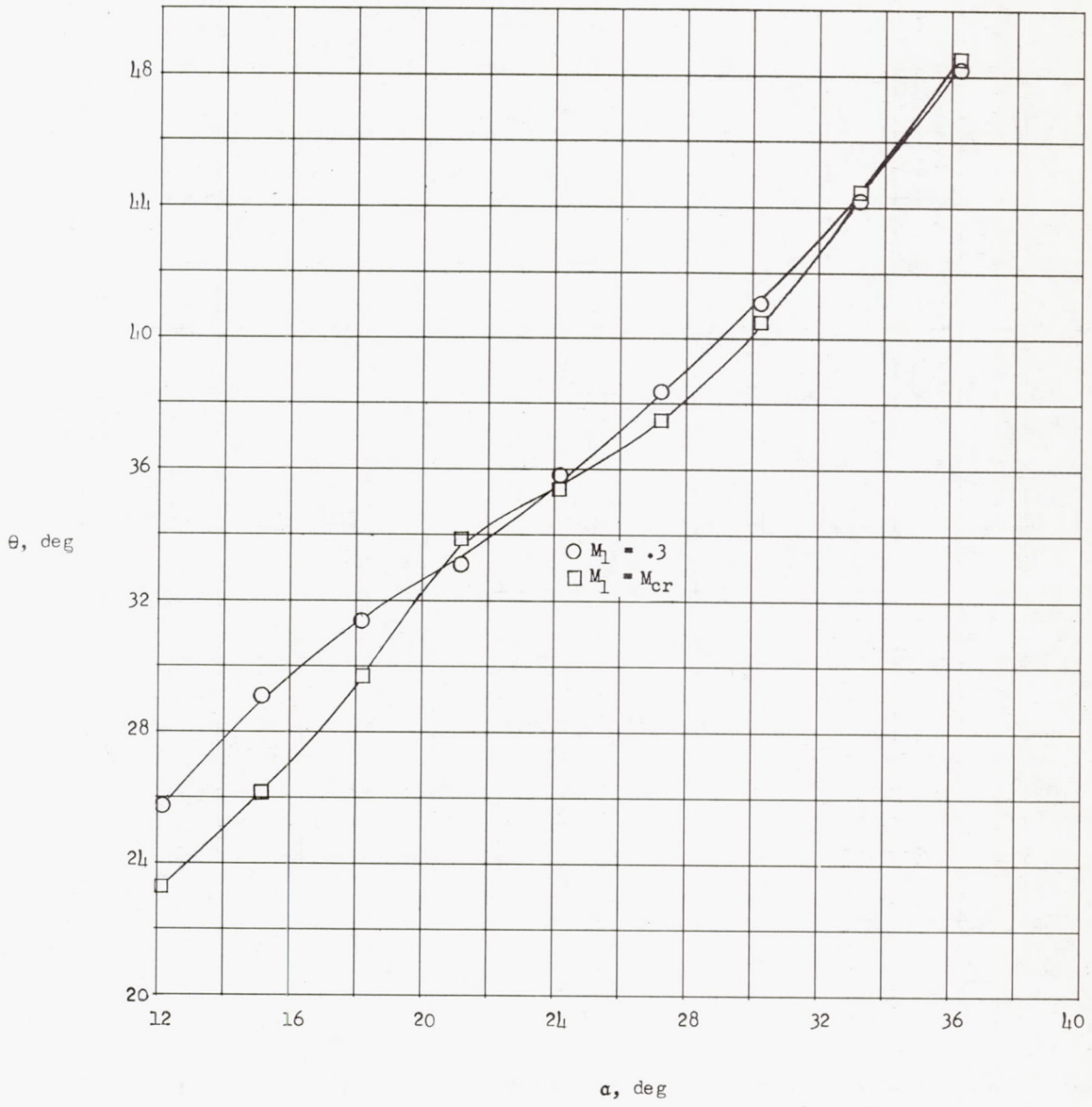


Figure 88.- Comparison of turning angles at high and low speeds for circular-arc configuration I at $\beta_1 = 35^\circ$ and $\sigma = 1.5$.

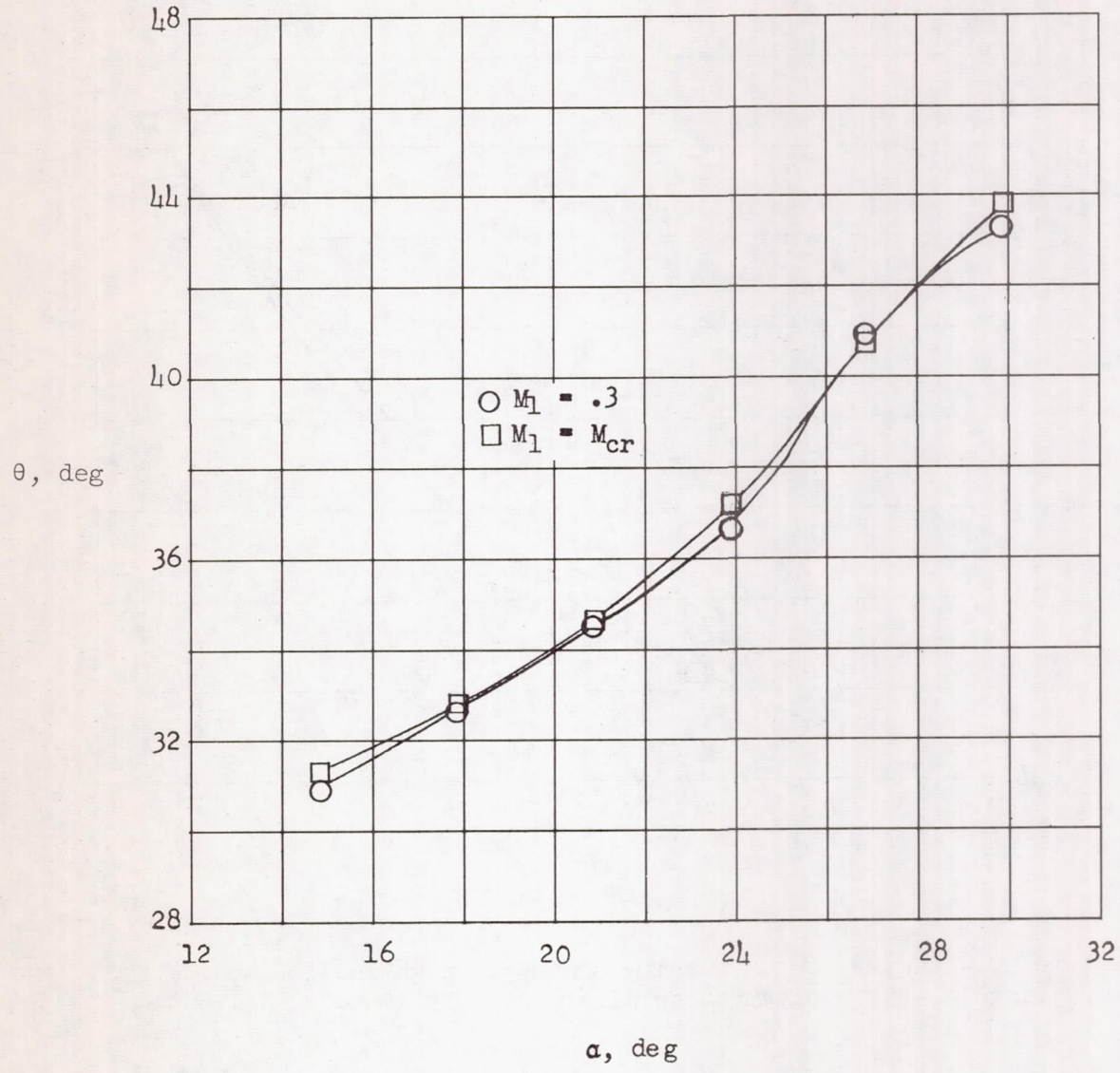


Figure 89.- Comparison of turning angles at high and low speeds for circular-arc configuration II at $\beta_1 = 25^\circ$ and $\sigma = 1.5$.

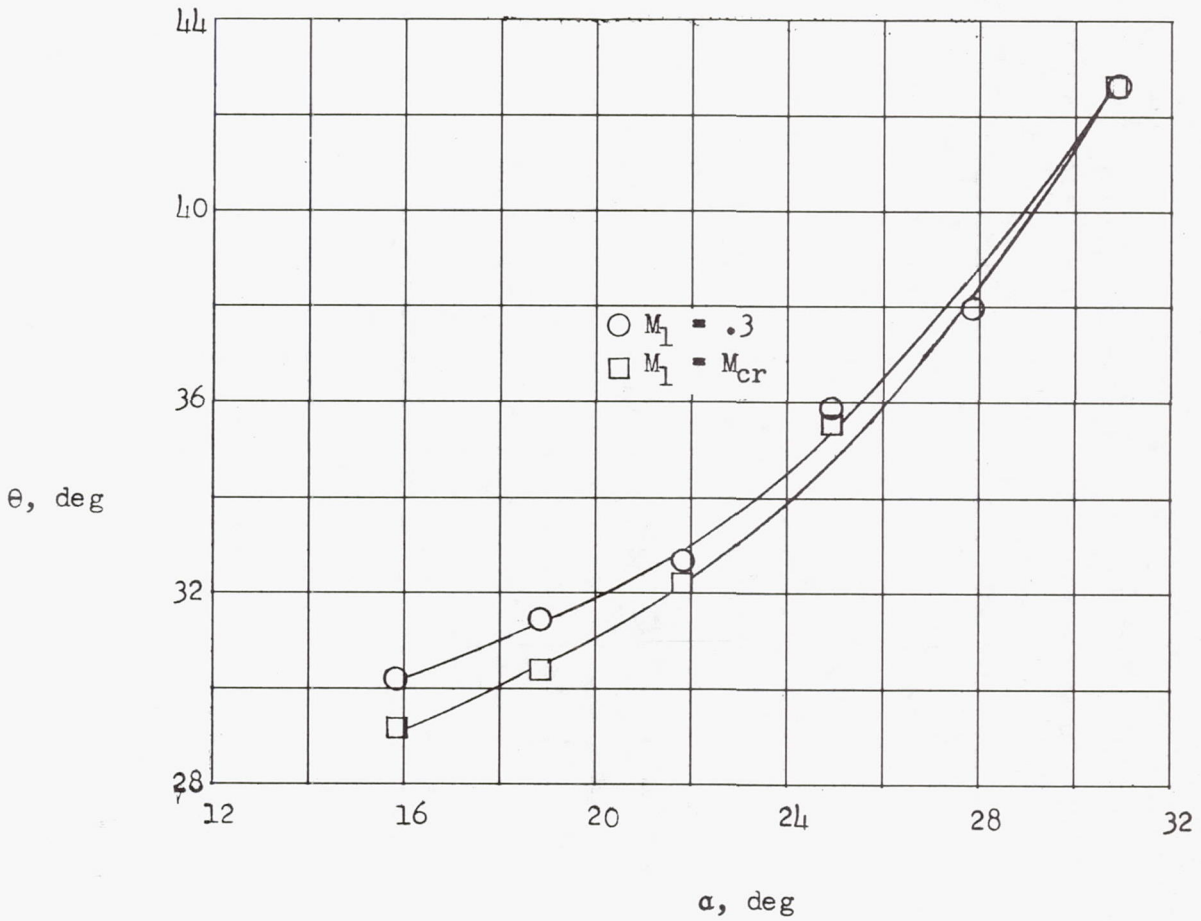


Figure 90.- Comparison of turning angles at high and low speeds for circular-arc configuration II at $\beta_1 = 35^\circ$ and $\sigma = 1.5$.

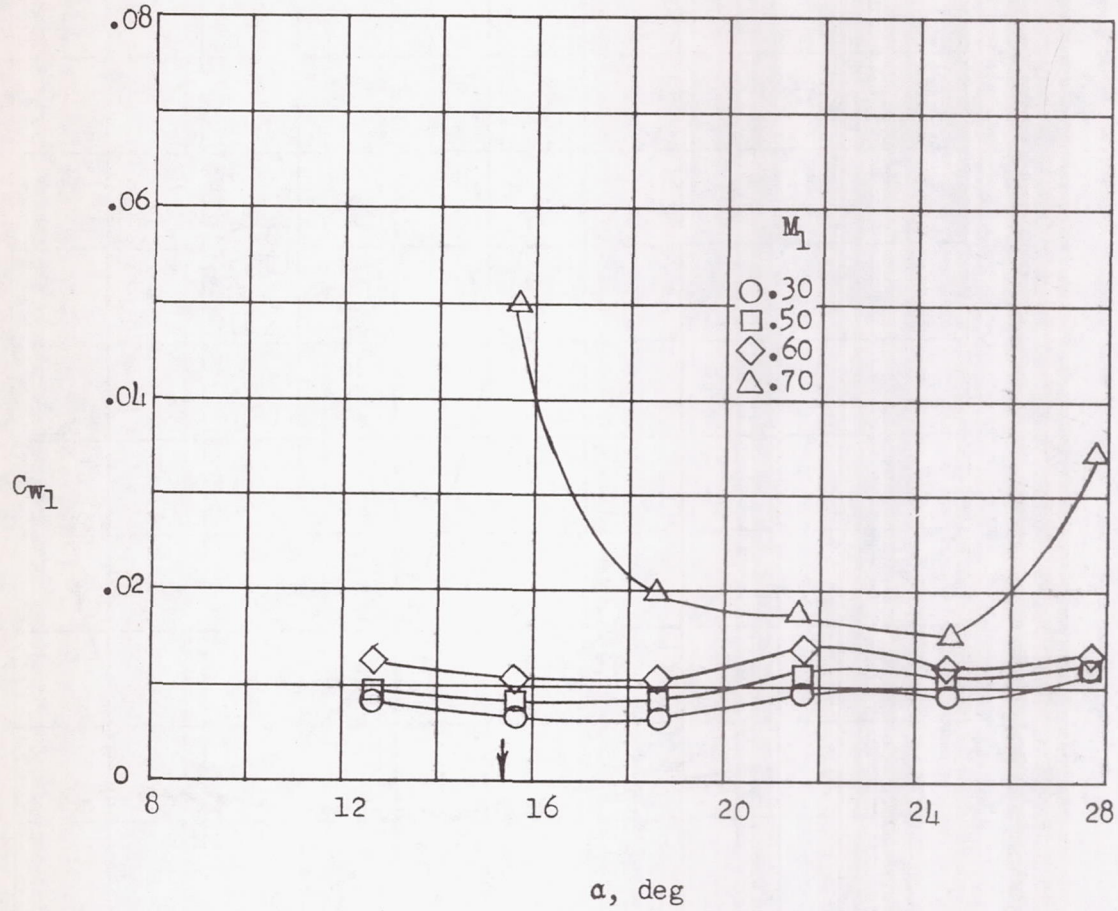


Figure 91.- Variation of momentum loss with angle of attack at constant Mach number for NACA 65-($12A_{10}$)10 blade section at $\beta_1 = 25^\circ$ and $\sigma = 1.5$. Arrow shows low-speed design angle of attack.

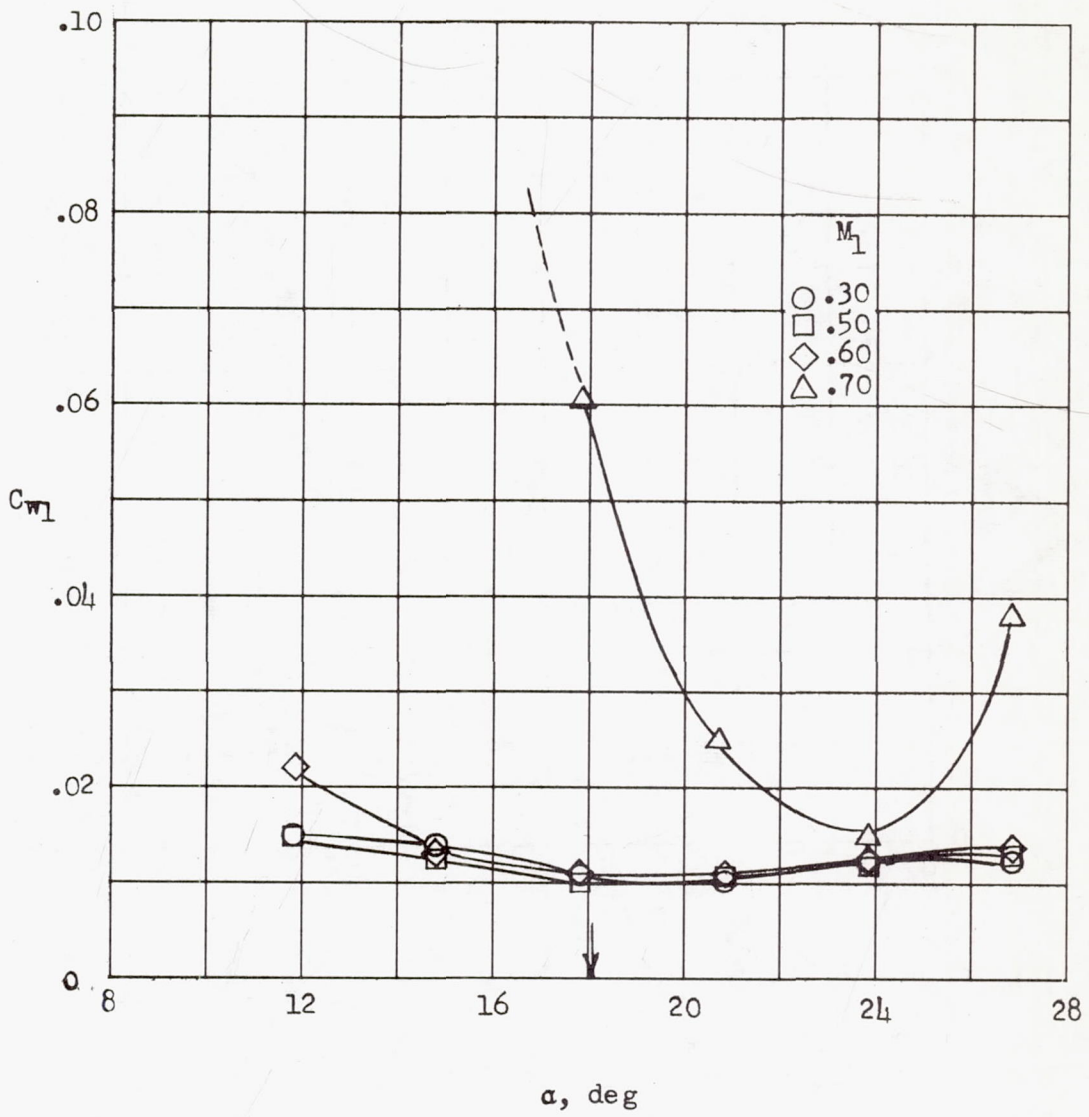


Figure 92.- Variation of momentum loss with angle of attack at constant Mach number for NACA 65-($15A_{10}$)10 blade section at $\beta_1 = 25^\circ$ and $\sigma = 1.5$. Arrow shows low-speed design angle of attack.

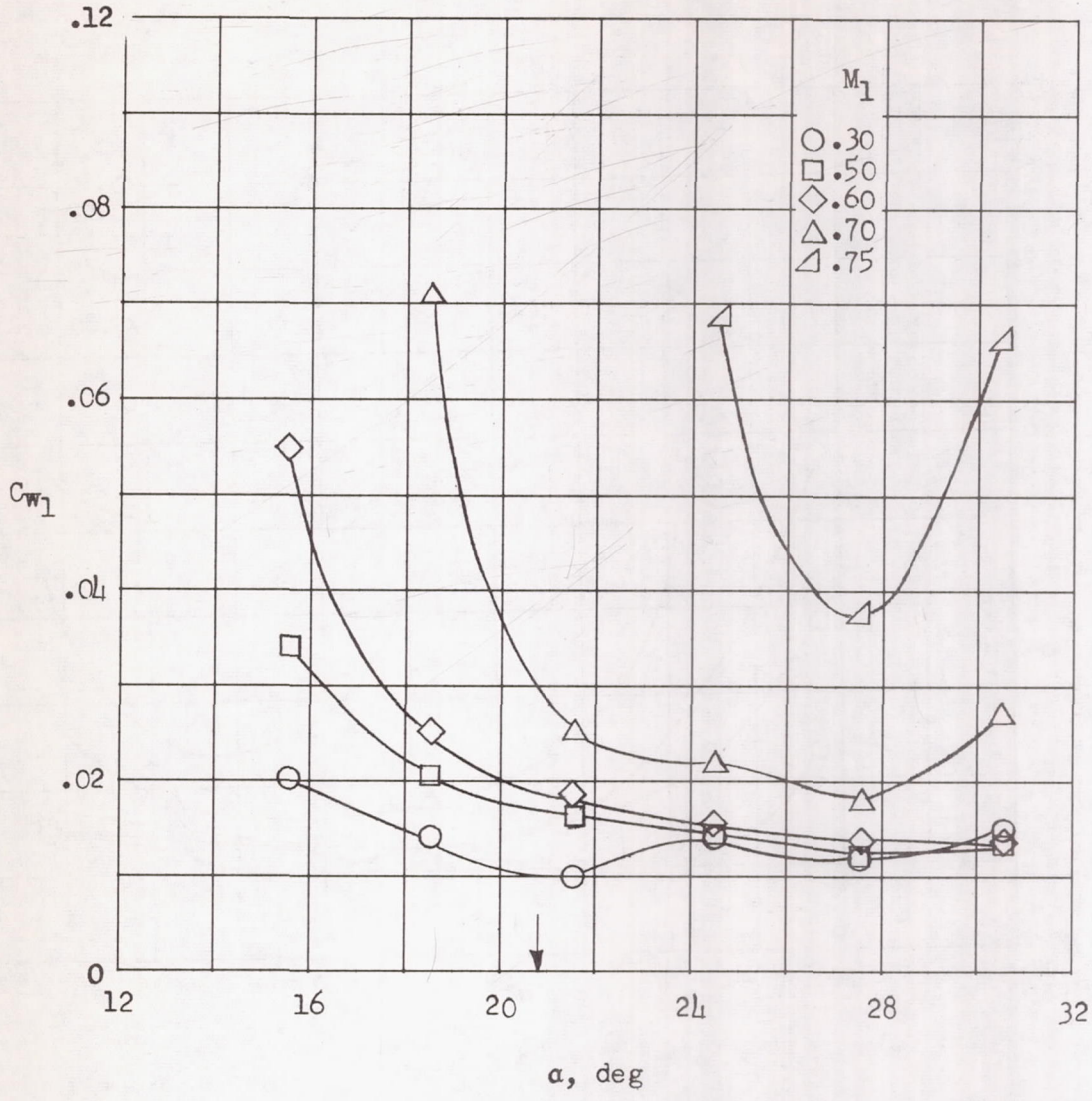


Figure 93.- Variation of momentum loss with angle of attack at constant Mach number for NACA 65-($18A_{10}$)10 blade section at $\beta_1 = 35^\circ$ and $\sigma = 1.5$. Arrow shows low-speed design angle of attack.

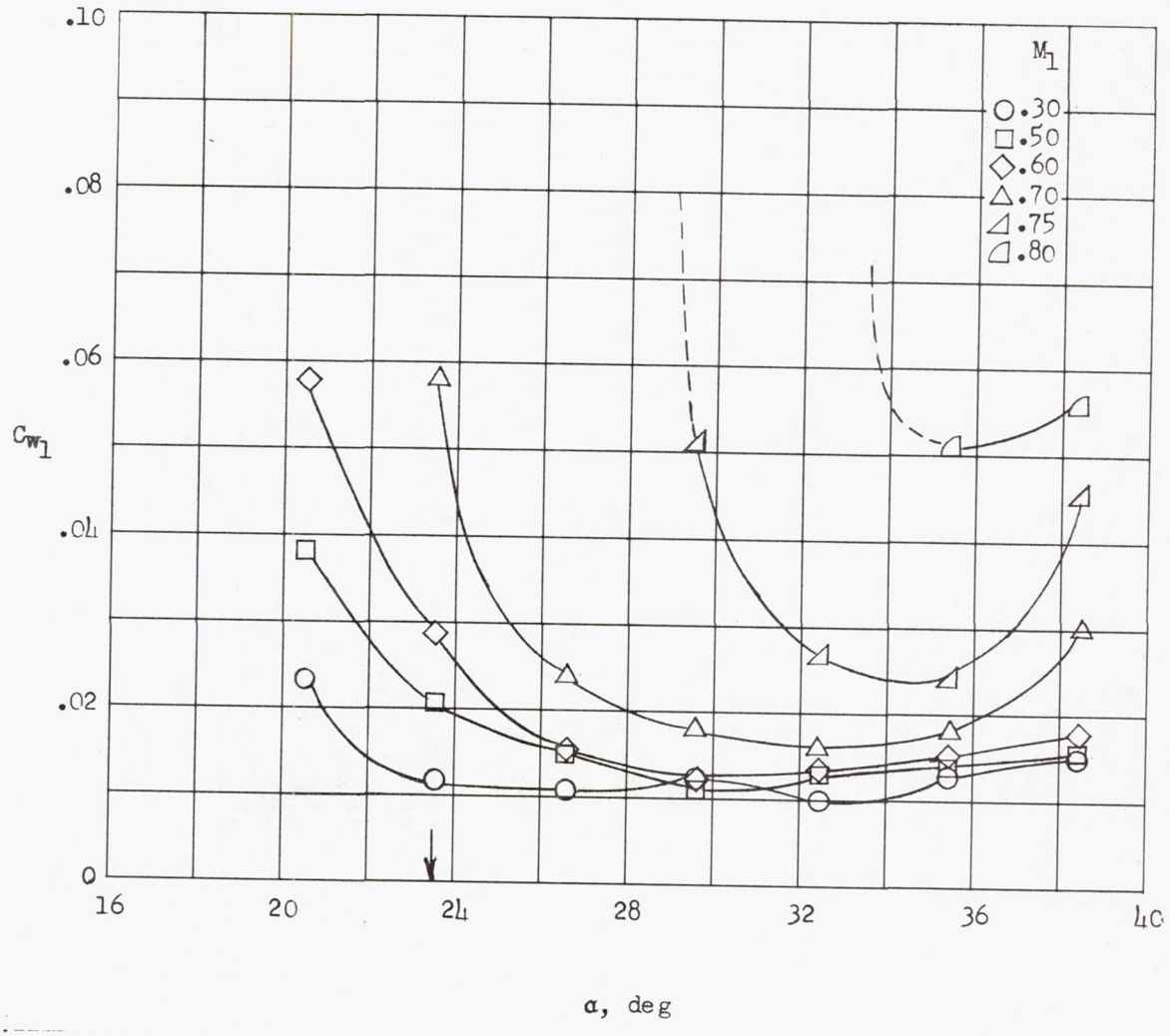


Figure 94.- Variation of momentum loss with angle of attack at constant Mach number for NACA 65-(21A10)10 blade section at $\beta_1 = 35^\circ$ and $\sigma = 1.5$.

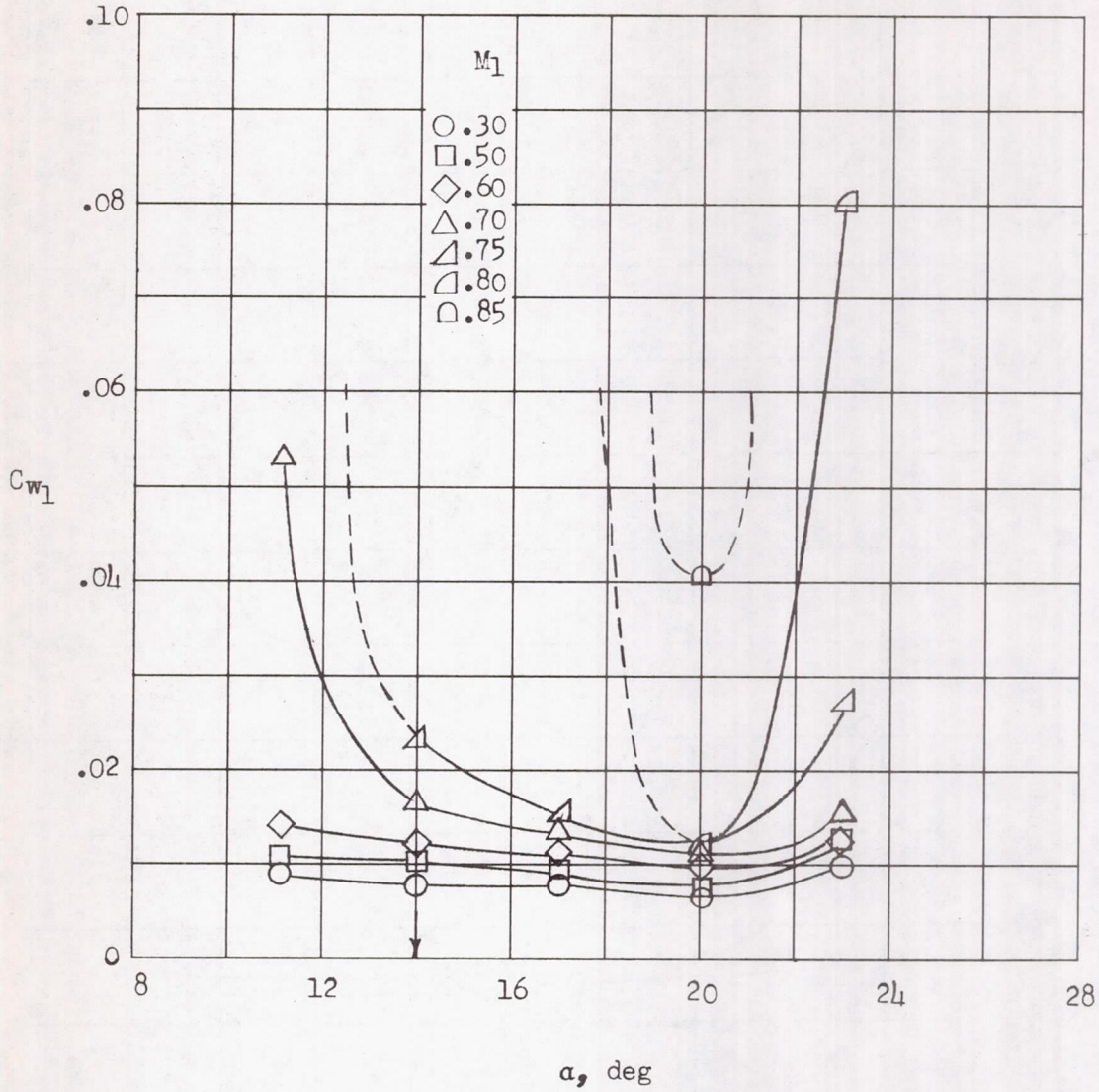


Figure 95.- Variation of momentum loss with angle of attack at constant Mach number for NACA 65-($12A_{10}$)10 blade section at $\beta_1 = 35^\circ$ and $\sigma = 1.25$. Arrow shows low-speed design angle of attack.

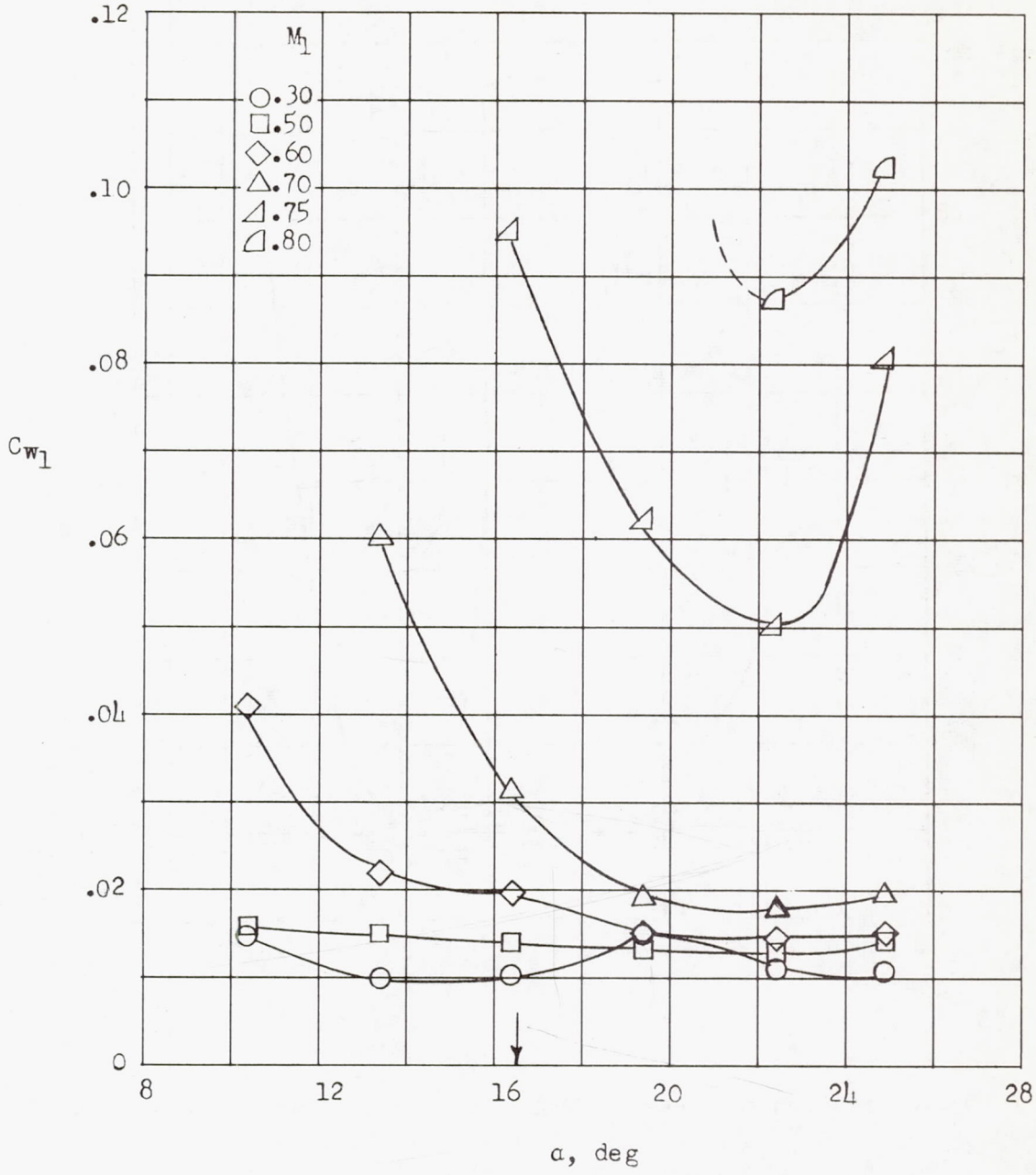


Figure 96.- Variation of momentum loss with angle of attack at constant Mach number for NACA 65-(15A10)10 blade section at $\beta_1 = 35^\circ$ and $\sigma = 1.25$. Arrow shows low-speed design angle of attack.

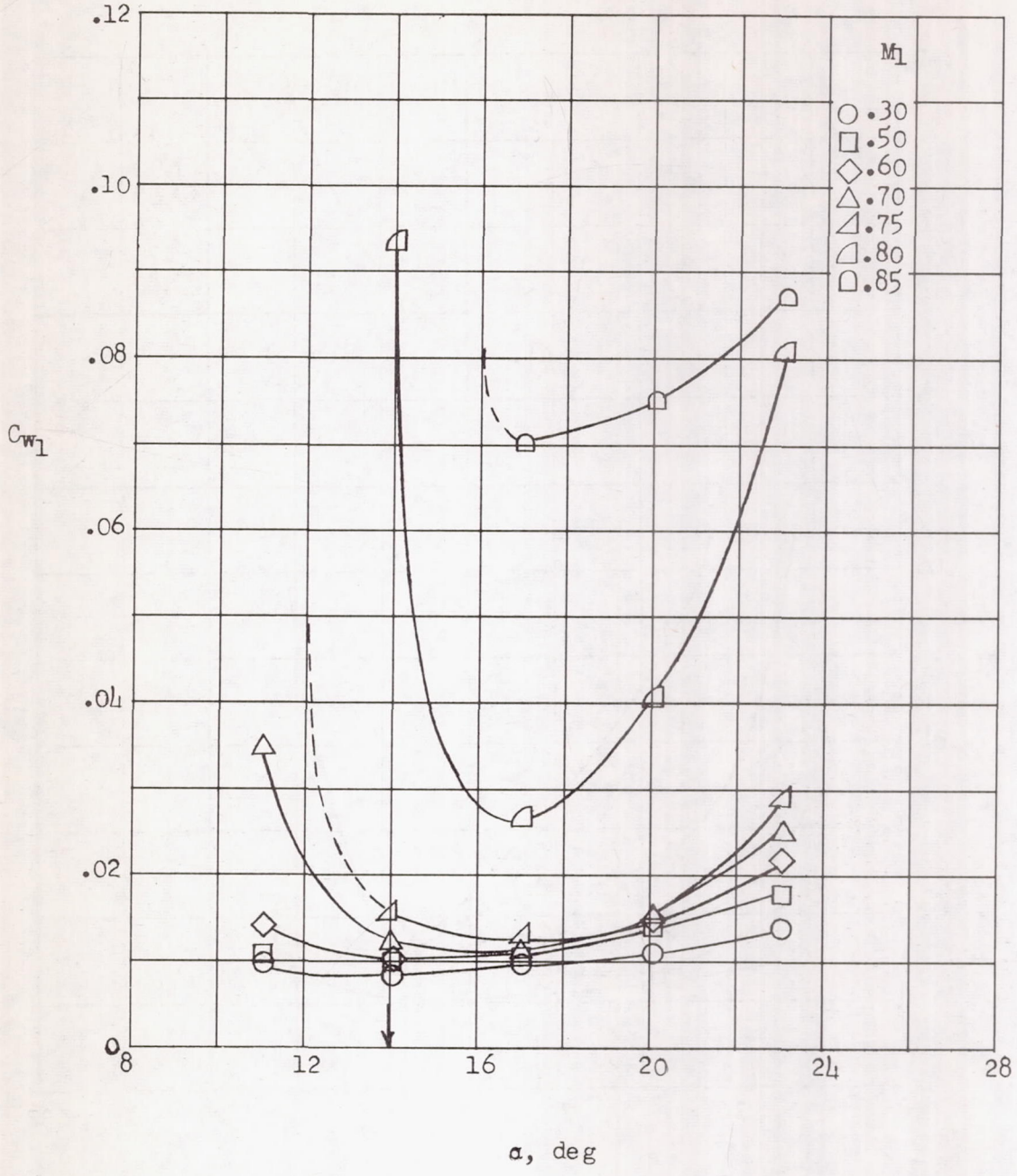


Figure 97.- Variation of momentum loss with angle of attack at constant Mach number for NACA 65-($12A_{10}$)10 blade section at $\beta_1 = 45^\circ$ and $\sigma = 1.25$. Arrow shows low-speed design angle of attack.

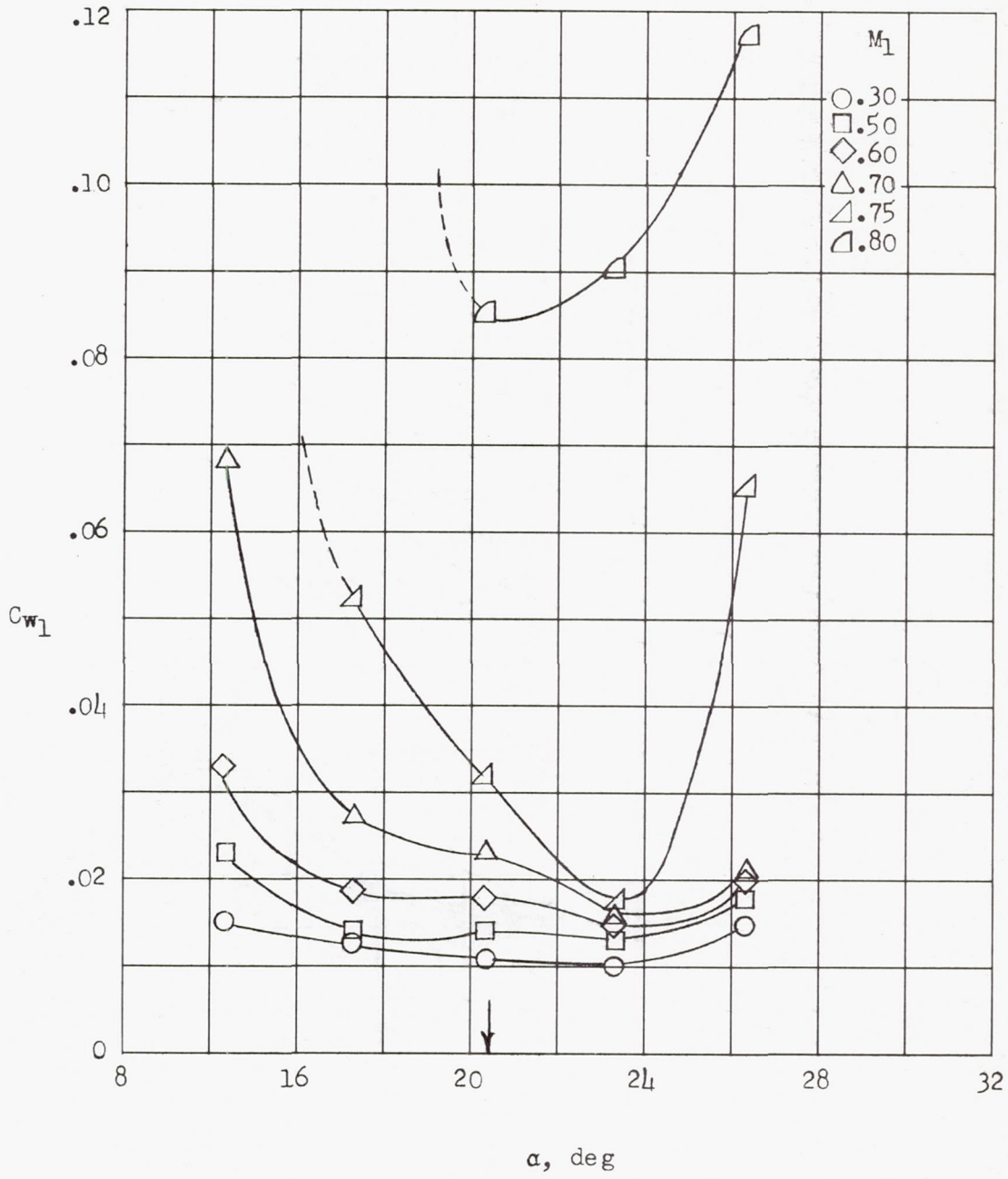


Figure 98.- Variation of momentum loss with angle of attack at constant Mach number for NACA 65-($15A_{10}$)10 blade section at $\beta_1 = 45^\circ$ and $\sigma = 1.25$. Arrow shows low-speed design angle of attack.

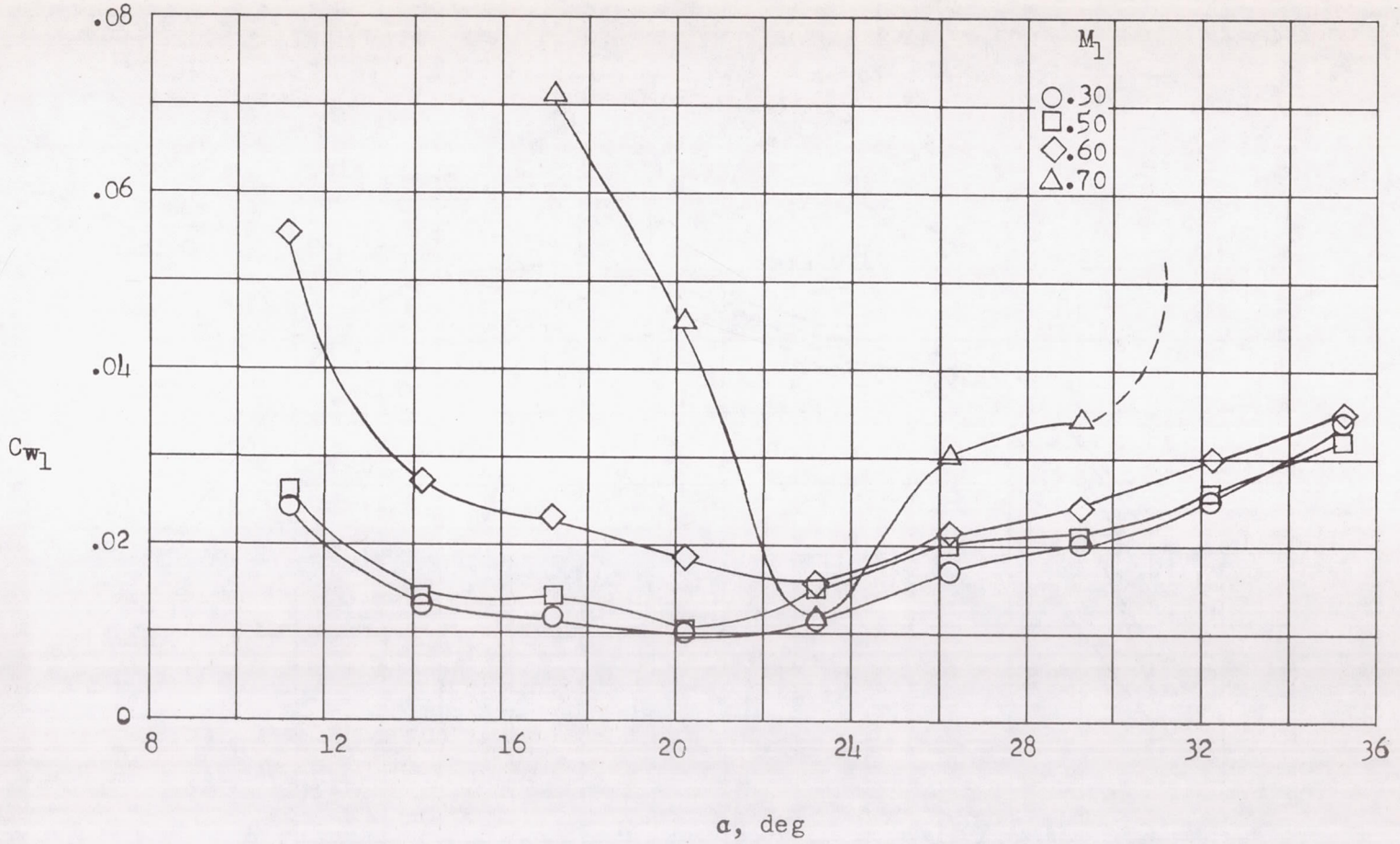


Figure 99.- Variation of momentum loss with angle of attack at constant Mach number for circular-arc configuration I at $\beta_1 = 25^\circ$ and $\sigma = 1.5$.

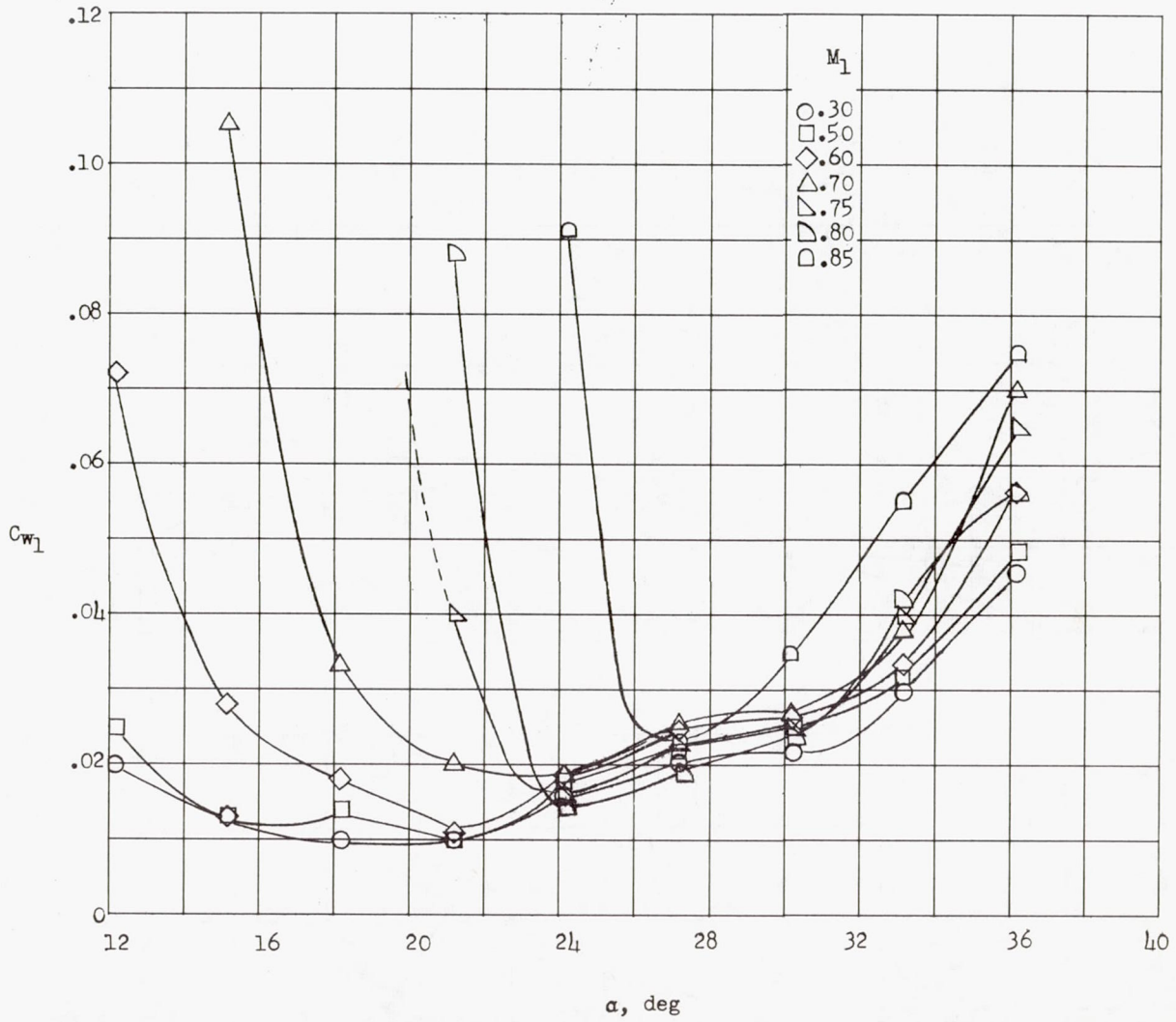


Figure 100.- Variation of momentum loss with angle of attack at constant Mach number for circular-arc configuration I at $\beta_1 = 35^\circ$ and $\sigma = 1.5$.

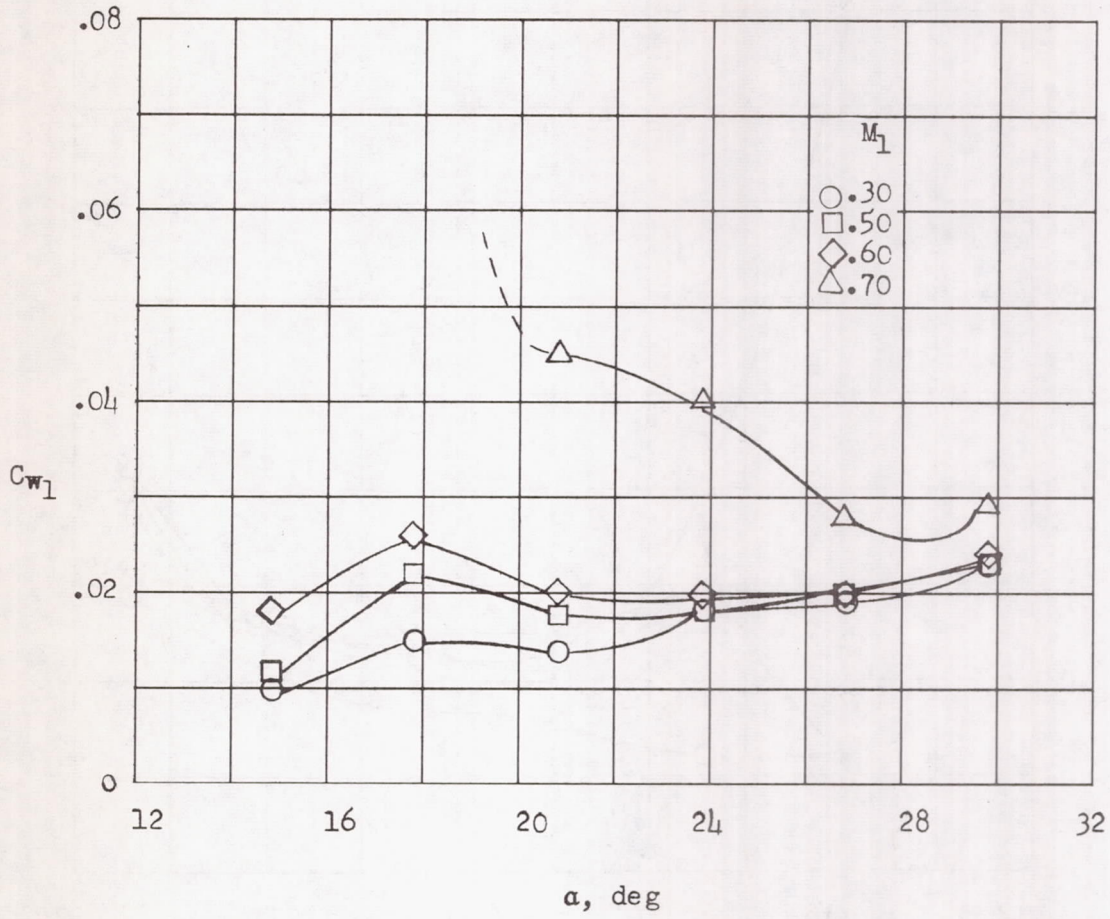


Figure 101.- Variation of momentum loss with angle of attack at constant Mach number for circular-arc configuration II at $\beta_1 = 25^\circ$ and $\sigma = 1.5$.

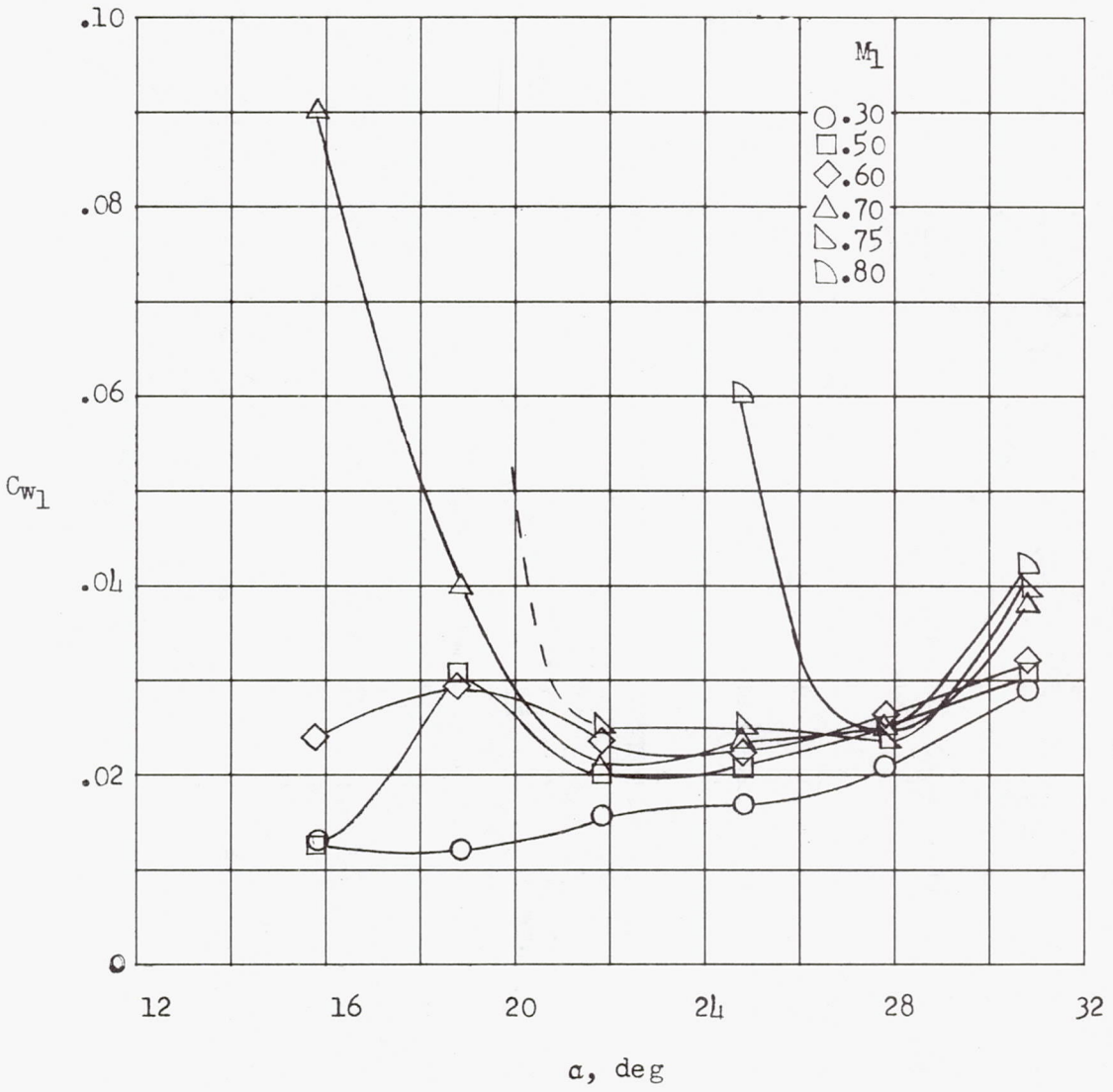


Figure 102.- Variation of momentum loss with angle of attack at constant Mach number for circular-arc configuration II at $\beta_1 = 35^\circ$ and $\sigma = 1.5$.

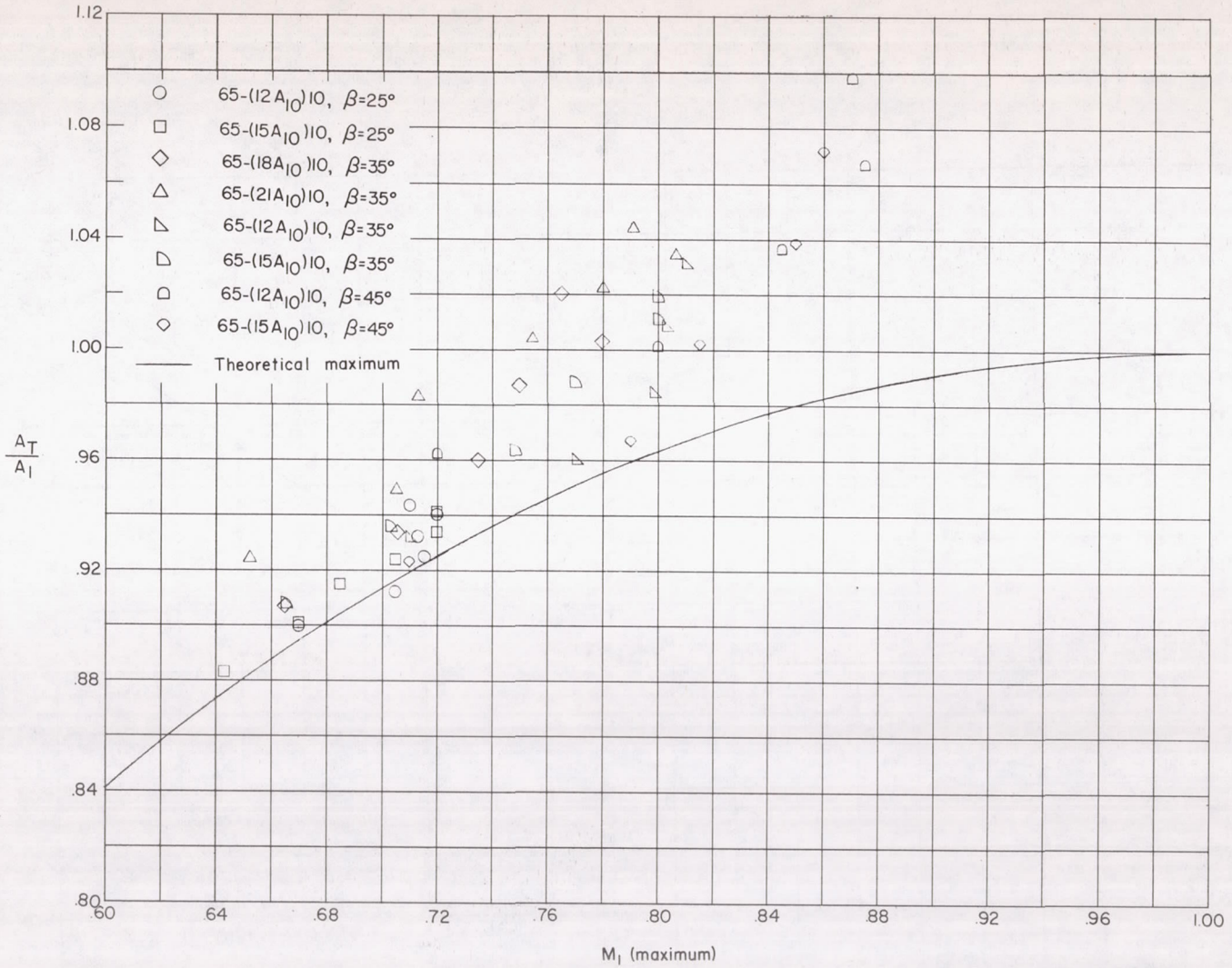


Figure 103.- Variation of throat area with maximum entering Mach number for 65-(C_{l_o}A10)10 blade-section tests.

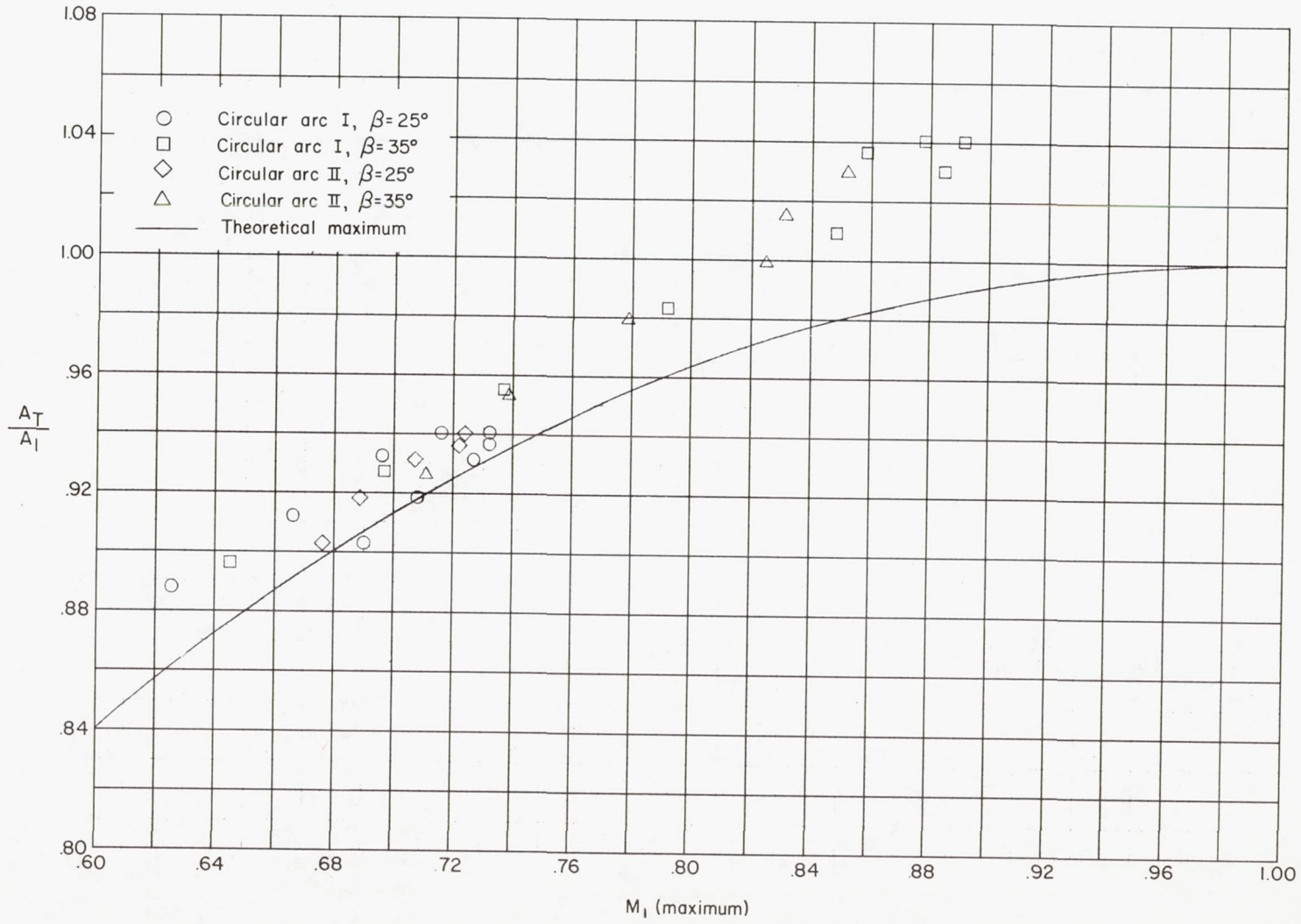


Figure 104.- Variation of throat area with maximum entering Mach number for circular-arc configurations I and II.

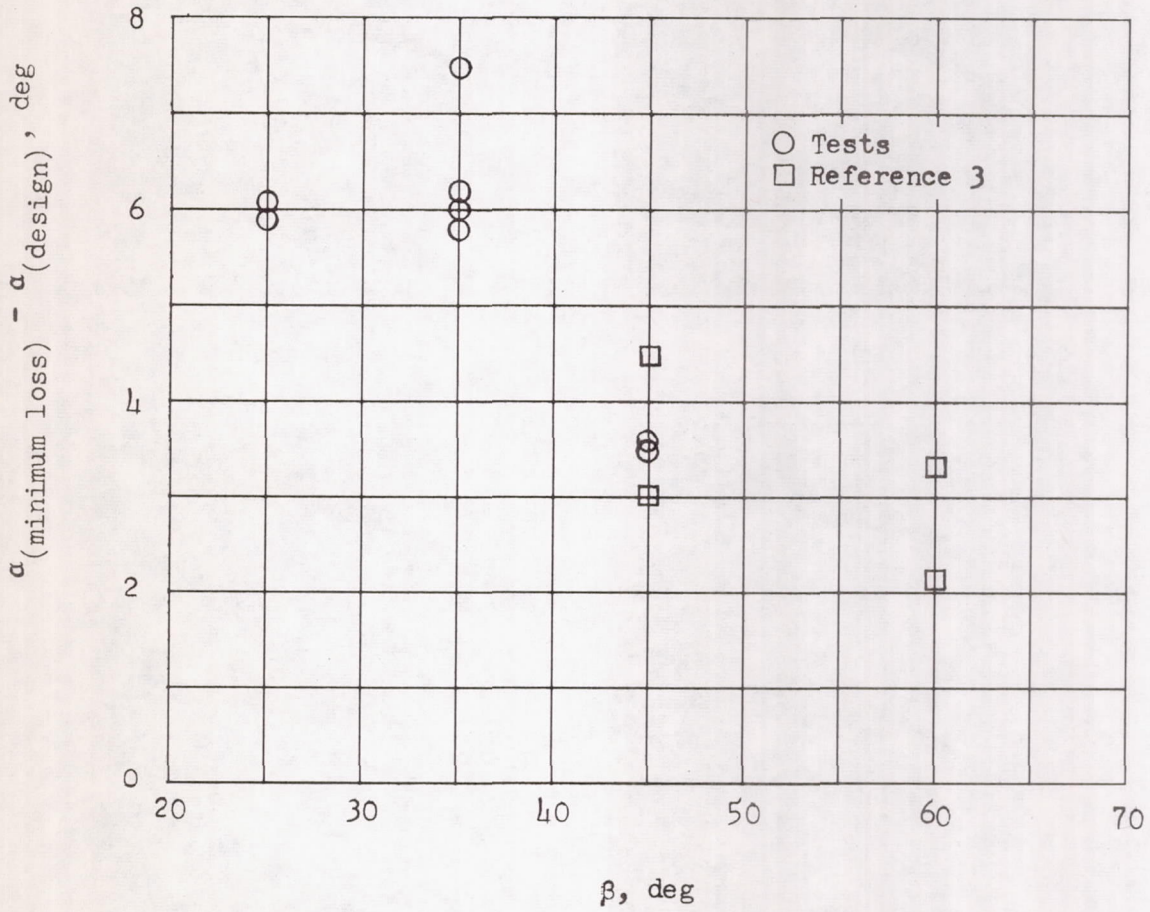
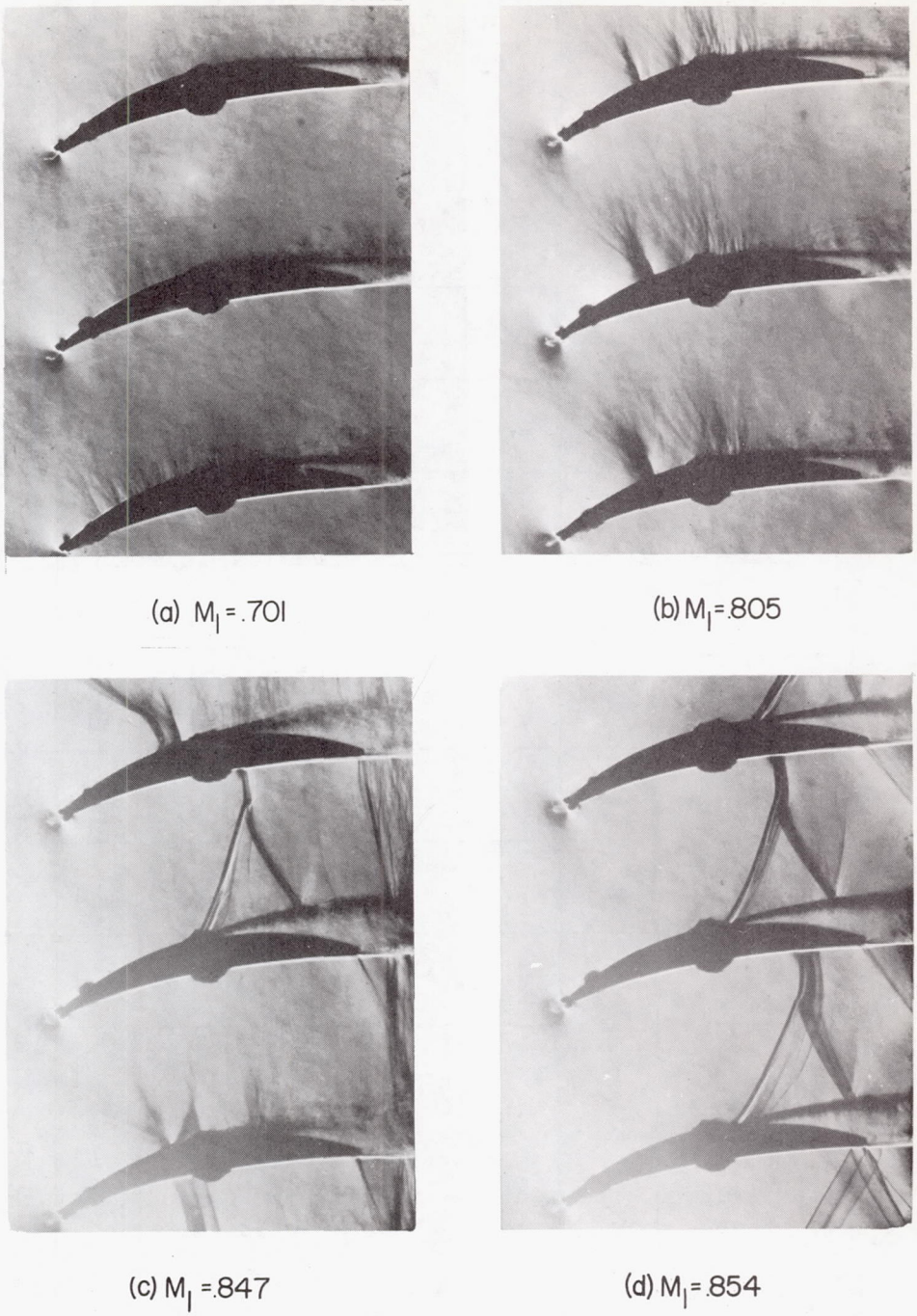


Figure 105.- Difference between low-speed design angle of attack and angle of attack for minimum losses at critical speed.



(a) $M_1 = .701$ (b) $M_1 = .805$

(c) $M_1 = .847$ (d) $M_1 = .854$

L-57-2734

Figure 106.- Schlieren photographs of the cascade combination $\beta_1 = 35^\circ$, $\sigma = 1.5$, $\alpha = 24.2^\circ$, and circular-arc configuration I.